

**Iron-doped Titanium Dioxide Nanomaterials:
Synthesis, Characterization and
Photodegradation Catalytic Behavior**

Mohammad Nazari

**A DISSERTATION SUBMITTED TO THE FACULTY OF GRADUATE
STUDIES IN PARTIAL FULFILMENT OF THE REQUIREMENTS FOR
THE DEGREE OF DOCTOR OF PHILOSOPHY**

GRADUATE PROGRAM IN CHEMISTRY

YORK UNIVERSITY

TORONTO, ONTARIO

January 2019

© Mohammad Nazari, 2019

Abstract

Titanium dioxide (TiO_2) is a very good material for various photocatalytic industrial applications because of its non-toxicity, high chemical stability, low cost and relatively good photoactivity. However, one of the most serious challenges to its applicability is its wide band gap and because of that TiO_2 absorbs mainly in the UV region of the solar spectrum, which corresponds to a small portion (<10%) of the sun's energy.

In this thesis, doping of TiO_2 is employed as a method to improve TiO_2 optical properties by decreasing the band gap and enabling the material to absorb a larger fraction of the visible spectrum. A series of iron-doped titanium dioxide nanoparticles containing various percentages of iron was prepared and their chemical, structural, optical and electrochemical properties were characterized. These results confirm that the proposed materials were successfully prepared and that they indeed have smaller band gaps.

Raman imaging was also employed to map the various phases present in our samples and to identify surface functionalities on the materials and their accessibility to binding especially with dyes, such as N3 and Z907 dye, for the first time. The results shows the coexistence of phases in TiO_2 as well as adsorption pattern of the dyes on the surface of the TiO_2 .

Finally, The photodegradation of methylene blue has been studied to quantify the photocatalytic activity of all prepared iron-doped TiO_2 and pure TiO_2 photocatalysts under simulated sunlight. The measurements are performed at two pH values and the different mechanism observed can be explained in terms of changes in the materials' potential of zero charge (PZC) and how surface charge affects the dye adsorption. Using the Langmuir-Hinshelwood model, rate constants (k_{obs}) decreasing with an increase in the molar percentage of iron in TiO_2 as well as a decrease in the materials' band gap. This trend is opposite to what was expected and it could be due to a significant increase in the charge recombination rate when the band gap is reduced, meaning that less charge is available to participate in the photodegradation process.

Dedications

-To my parents who raised me with their unconditional love, warmth, support, patience and kindness allowed me to focus on my life goals and reach my dreams.

-To my siblings for their love, support and kindness.

-To my role model, Dr. Mostafa Chamran, for his inspiration to survive even in the most sophisticated conditions.

Acknowledgement

First and foremost, I must express my gratitude to my supervisor, Professor Sylvie Morin, for all her incredible support through this project. You have shown me how to think in a critical way while having always the big picture of the project in my mind. I appreciate the freedom you provided for me to learn and find my way through out conducting this project. I warmly thank you for providing the opportunity to travel to Germany two times for my research and internship, although they were not mandatory parts of my PhD program.

I also thank Professor René Fournier for undertaking the membership of my supervisory committee. I applaud your positive attitude as well as your constructive support. I acknowledge Professor Jennifer Chen not only as a member of my supervisory committee, but also for assisting us to conduct part of my experiments in her research lab. Your great help and cooperation is well appreciated. I express my gratitude to Professor Jérôme Claverie and Professor Usman T. Khan for being my external and internal examiners, respectively. I appreciate your great feedback.

I am incredibly grateful to Professor Susan Andrews from Department of Civil Engineering at University of Toronto, for her great collaboration for running all photocatalytic tests. I will never forget your kindness, support and the positive environment you provided me to successfully finish the last part of my work. I would also like to thank her Master's student, Sarah Larlee, for training me all necessary aspect of the DWRG (Drinking Water Research Group) facilities. As one of the most inspiring scientists in my life, I would like to thank Dr. Melisa Hatat Fraile, postdoctoral fellow from the DWRG, for nourishing my mind with new ideas regarding my research. I would like to acknowledge all other members of the DWRG at University of Toronto for all your astonishing help, effort and welcoming attitude, especially Dr. Kerry Evans-Tokaryk and Jim Wang.

I express my thanks to Dr. Srebri Petrov and George Kretschmann, both from University of Toronto, for their great collaboration for performing XRD experiments. I also thank Ms. Karen Rethoret and Dr. Magdalena Jaklewicz from York University for assisting with the SEM experiments.

Definitely, one of my unforgettable memories of my academic life was my internship period during summer 2018 at BASF SE, the world's largest chemical company located in Ludwigshafen, Germany. I was fortunate to meet two of the greatest people I have worked with during all my career life, Dr. Masayuki Hirose and Dr. Daniel Wilms. I would like to express my deep gratitude to Dr. Hirose for his unbelievable mentorship, kindness and support. I also acknowledge Dr. Wilms for his welcoming attitude, organization and positive approach.

I express also my special gratitude to Dr. Klaus Weishaupt, the managing director of Witec GmbH for his great hospitality at Witec GmbH in Ulm, Germany to perform Raman imaging as well as sponsoring me to participate in a conference in Jena, Germany. I should admit that without the enormous help, coordination and supervision of Dr. Elena Bailo, it would have been impossible to run any experiments there. I would like to kindly thank other Witec GmbH staff for their support.

I should thank especially two of my former colleagues in our research group, Dr. Ali Sepehrifard and Dr. Maryam Hariri for all their support, guidance and cooperation. I will never forget all your endless effort to help me to adjust myself in a new country, city and university. I also thank my other current and former coworkers and officemates, Dr. Moriam Ore, Sreena Thekkoot, Dr. Sven Kochmann, Paola Guarracino, Dr. Victor Galievsky and Antoine Dumont, for all the wonderful time that we have spent together.

It is impossible to find yourself happy after moving to a new country without having wonderful friends that you can share both your happiness and hardships with them. I discover two of my best friends at York University, Dr. Amirsaman Sajad and Dr. Mahdi Daemi, after I encountered the biggest challenges of my whole life. You are both my friends for life. Thank you both for helping me when nobody pays any attention to me.

I express my gratitude to all former and current staff members of Department of Chemistry at York University, especially Mary Mamais, Magy Baket, Natasha May and Sindy Mahal for your constant help during my academic life at York University.

The last but not least, I would like to acknowledge all my family members. Although I have been living very far from you, you have been always in my heart. Without you, it was impossible to accomplish any kind of success I have reached so far in my life. I would like to thank the most

important person in my life, my mother. I know I am not able to thank you as you deserve it. Your unconditional love and understanding means the world to me. You are always my role model in terms of patience, kindness and humanity. I am very blessed to have you in life.

Table of Contents

Abstract.....	ii
Dedications.....	iii
Acknowledgement.....	iv
Table of Contents.....	vii
List of Tables.....	xiii
List of Figures.....	xiv
List of Abbreviations.....	xxii
Chapter 1: Introduction.....	1
1-1-Outline of the thesis.....	1
1-2-Introduction.....	2
1-3-Chemical structure of titanium dioxide.....	3
1-4-Doping.....	5
1-5-Sol-gel method for production of TiO ₂ materials.....	6
1-6-Iron as a dopant for titanium dioxide.....	7
1-7-Photochemical activity of titanium dioxide.....	8
1-8-Principles of semiconductor-based photocatalysis.....	8
1-8-1-Mechanism of photocatalyzed dye degradation.....	10
1-9-Effect of pH on the photocatalytic reactions.....	14
1-10-Kinetics of photocatalytic reactions.....	15

1-11-Reported iron-doped titanium dioxides as photodegradation catalysts.....	16
1-11-1-Iron-doped titanium dioxide materials used as photodegradation catalysts with focus on synthetic methods.....	17
1-11-2-Iron-doped titanium dioxide thin films used as photodegradation catalysts.....	18
1-11-3-Organic molecules applied as model pollutant in photodegradation studies with iron-doped titanium dioxide materials.....	19
1-11-4-Mechanism of the photodecomposition reaction promoted by iron-doped TiO ₂ materials.....	21
1-12-Raman spectroscopy.....	24
1-13-Application of Raman mapping for titanium dioxide characterization.....	26
1-14-Raman imaging of dye-adsorbed TiO ₂ films.....	32
1-15-Thesis objectives.....	33
1-16-References.....	35

Chapter 2: Synthesis and Characterization of Iron-doped Titanium Dioxide Nanomaterials.....42

2-1-Introduction.....	42
2-2-Synthesis.....	42
2-2-1-Synthesis of pure and iron-doped titanium dioxide nanomaterials.....	42
2-2-1-1-Background.....	42
2-2-1-2-Experimental.....	42
2-2-2-Synthesis of iron (III) oxide.....	43
2-2-2-1-Background.....	43

2-2-2-2-Experimental.....	43
2-3-Characterization of the synthesized nanomaterials.....	44
2-3-1-Methodology.....	44
2-3-1-1-Powder XRD diffraction.....	44
2-3-1-1-1-Background.....	44
2-3-1-1-2-Experimental.....	45
2-3-1-2-Diffusive Reflectance UV-Vis spectroscopy (UV-Vis DRS).....	45
2-3-1-2-1-Background.....	45
2-3-1-2-2-Experimental.....	45
2-3-1-3-Scanning electron microscopy (SEM).....	45
2-3-1-3-1-Background.....	45
2-3-1-3-2-Experimental.....	46
2-3-1-4-Energy Dispersive X-ray (EDX) analysis.....	46
2-3-1-4-1-Background.....	46
2-3-1-4-2-Experimental.....	46
2-3-1-5-Differential Scanning Calorimetry (DSC).....	46
2-3-1-5-1-Background.....	46
2-3-1-5-2-Experimental.....	47
2-3-1-6-Cyclic Voltammetry (CV).....	47
2-3-1-6-1-Background.....	47
2-3-1-6-2-Experimental.....	47

2-3-2-Results and Discussion.....	48
2-3-2-1-Powder XRD diffraction.....	48
2-3-2-1-1-Powder XRD diffractions of pure and iron-doped titanium dioxide nanomaterials.....	48
2-3-2-1-2-Powder XRD diffraction of iron (III) oxide.....	51
2-3-2-2-Diffusive Reflectance UV-Vis spectroscopy (UV-Vis DRS).....	52
2-3-2-3-Scanning electron microscopy (SEM).....	60
2-3-2-3-1-Scanning electron microscopy (SEM) of pure and iron-doped titanium dioxides.....	60
2-3-2-3-2-Scanning electron microscopy (SEM) of iron (III) oxide.....	62
2-3-2-4-Energy Dispersive X-ray (EDX) analysis.....	62
2-3-2-4-1-Energy Dispersive X-ray (EDX) analysis of pure and iron-doped titanium dioxide nanomaterials.....	62
2-3-2-4-2-Energy Dispersive X-ray (EDX) analysis of iron (III) oxide.....	64
2-3-2-5-Differential Scanning Calorimetry (DSC).....	65
2-3-2-6-Cyclic Voltammetry (CV).....	66
2-4-Conclusion.....	70
2-5-References.....	72
2-6-Appendix 1: XRD-pattern of pure anatase, pure brookite and pure rutile.....	76
2-7-Appendix 2: EDX experiment for all iron-doped TiO ₂ nanomaterials.....	77
2-8-Appendix 3: Cyclic voltammetry experiment for iron-doped TiO ₂ (5 mol% Fe). Each experiment contains three consecutive cycles.....	80

Chapter 3: Confocal Raman Mapping.....	82
3-1-Introduction.....	82
3-2-Raman imaging of pure and iron-doped titanium dioxide nanomaterials.....	84
3-2-1-Experimental.....	84
3-2-2-Results and discussion.....	85
3-2-2-1-Raman imaging of synthesized pure and iron-doped titanium dioxides.....	85
3-2-2-2-Raman imaging of commercial Aeroxide P25.....	91
3-3-Raman imaging of dye-adsorbed TiO ₂ films.....	95
3-3-1-Experimental.....	96
3-3-2-Results and discussion.....	97
3-3-2-1-N3 dye adsorbed on synthesized pure and iron-doped titanium dioxide.....	97
3-3-2-2-Z907 dye adsorbed on synthesized pure and iron-doped titanium dioxide.....	101
3-4-Conculsion.....	104
3-5-References.....	106
Chapter 4: Photodegradation Properties of Iron-doped Titanium Dioxide Nanomaterials.....	108
4-1-Introduction.....	108
4-2-Experimental.....	108
4-2-1-Materials.....	108
4-2-2-Instrumentation.....	108
4-2-3-Photodegradation experimental setup.....	109

4-3-Results and Discussion.....	109
4-3-1-Kinetic studies on photodegradation reaction of methylene blue.....	122
4-4-Conclusion.....	128
4-5-References.....	130
Chapter 5: Conclusions and Future Outlook.....	132
5-1-Coclusions.....	132
5-2-Future outlook.....	134
5-3-References.....	136

List of Tables

Table (1-1). Comparison between different Fe-doped TiO ₂ used for photodegradation of methylene blue.....	21
Table (2-1). The amount of Fe(NO ₃) ₃ .9H ₂ O used to prepare iron-doped TiO ₂ samples.....	43
Table (2-2). XRD results for all samples.....	51
Table (2-3). The calculated band gaps of the prepared samples.....	59
Table (2-4). The theoretical and real amount of iron as a dopant, based on the EXD results.....	63
Table (4-1). Intermediate compounds formed during photodegradation of methylene blue and their maximum absorption intensity wavelength.....	116
Table (4-2). The calculated k _{obs} values according to theoretical and empirical amount of iron in titanium dioxide for methylene blue photodegradation at pH=4.5.....	124
Table (4-3). The calculated k _{obs} values according to theoretical and empirical amount of iron in titanium dioxide for methylene blue photodegradation at pH=2.4.....	127

List of Figures

- Figure (1-1). Solar spectrum at sea level with the sun at its zenith. Reprinted with permission from reference [11], Copyright © 1995, American Chemical Society.....3
- Figure (1-2). Crystal structure of anatase and rutile. Reprinted with permission from reference [11], Copyright © 1995, American Chemical Society.....4
- Figure (1-3). crystal structure of anatase, rutile and brookite. Reprinted with permission from reference [20], Copyright © 2010, American Chemical Society.....5
- Figure (1-4). Photoexcitation process in (a) V-doped TiO₂ (b) Fe-doped TiO₂ (c) Cr-doped TiO₂. Reprinted from reference [22], Copyright © 2002, With permission from Elsevier.....6
- Figure (1-5). Schematic photoexcitation and deexcitation events in a semiconductor. Reprinted with permission from reference [47], Copyright © 1995, American Chemical Society.....9
- Figure (1-6). Time scales for photoinduced reactions in titanium dioxide. Reprinted with permission from reference [48a], Copyright © 2014, American Chemical Society.....10
- Figure (1-7). Schematic representation of indirect photocatalytic dye degradation. Republished with permission from reference [55], Copyright © 2014, RSC Publishing.....13
- Figure (1-8). Schematic representation of direct photocatalytic dye degradation. Republished with permission from reference [55], Copyright © 2014, RSC Publishing.....14
- Figure (1-9). Schematic diagram of energy states in Raman spectroscopy. Republished from open-access reference [106], © 2015, Lupoi J. S.; Gjersing E.; Davis M. F.; *Front. Bioeng. Biotechnol.*, 2015, 3, 1., <https://www.frontiersin.org/articles/10.3389/fbioe.2015.00050/full>.....25
- Figure (1-10). Black-and-white Raman images recorded from anodically grown TiO₂ film representing two different polymorphs of TiO₂. Reprinted from reference [114], Copyright © 1995, With permission from Elsevier.....28
- Figure (1-11). Confocal Raman mapping of anatase/rutile distribution on P25 film fired at 450 °C. Anatase and rutile are color-coded with black and red, respectively. In image (C) the same

color code are applied to exert anatase-rich and rutile-rich spectra. Raman scattering intensity at 398 and 448 cm^{-1} bands across the cross section lines in (A) and (B) are depicted in (D). Reprinted with permission from reference [115], Copyright © 2009, American Chemical Society.....28

Figure (1-12). Confocal Raman mapping of anatase/brookite distribution on the prepared film: (a) Optical microscope image of the mapped area (b) Raman image of anatase taken at 143 cm^{-1} (b) Raman image of brookite taken at 247 cm^{-1} (c) Raman image of brookite taken at 152 cm^{-1} [117]. Reprinted by permission from Springer Nature: reference [117], Copyright © 2012.....29

Figure (1-13). Raman images of TiO_2 nanofibers (left side) and carbon nanotubes (right side). Republished from open access reference [120], © 2017 The Authors. Published by WILEY-VCH Verlag GmbH & Co. KGaA, Weinheim, <https://onlinelibrary.wiley.com/doi/10.1002/advs.201600504>.....30

Figure (1-14). The Raman images for (a) anatase (b) rutile (c) amorphous carbon (The brighter color in each image means higher content of that phase). (d) and (e) are Raman spectra taken from different tagged points on the sample. Reprinted from reference [121], Copyright © 2008, With permission from Elsevier.....31

Figure (1-15). Raman images of (a) BJ cells (b) TiO_2 nanoparticles (c) distribution of TiO_2 nanoparticles in BJ cells. Republished from open access reference [125], Harvanová M.; Mašek V.; Jírová D.; Kolářová H.; *Lékař a technika*, 2016, 46(1), 25, <https://ojs.cvut.cz/ojs/index.php/CTJ/article/view/4204/4058>.....32

Figure (1-16). Confocal Raman imaging of N719 dye adsorbed on the commercial TiO_2 surface. Reprinted with permission from reference [128], Copyright © 2010, American Chemical Society.....33

Figure (2-1). The powder XRD spectra of iron doped titanium dioxides according to the theoretical iron percentage as dopant.....48

Figure (2-2). Rietveld fitting utilized for XRD pattern analysis of iron-doped TiO_2 (0.5 mol% iron).....50

Figure (2-3). The powder XRD pattern of iron (III) oxide nanoparticles.....	52
Figure (2-4). The powder XRD pattern of α -phase iron (III) oxide. Reprinted from reference [23] , Copyright © 2016, With permission from Elsevier.....	52
Figure (2-5). The DRS UV-Vis spectra of P25 (commercial TiO ₂), pure synthesized TiO ₂ and iron doped titanium dioxides.....	53
Figure (2-6). The DRS UV-Vis spectra of solid mixtures composed of synthesized iron (III) oxide and synthesized pure titanium dioxide with molar ratios similar to doped samples with 0.7, 1.7 and 5 mol% iron.....	55
Figure (2-7). Comparison between the spectra of the iron-doped TiO ₂ and its corresponding mixture of iron (III) oxide and titanium dioxide.....	56
Figure (2-8). The linear relationship between iron (III) peak (at 480 nm) in DRS UV-Vis spectra of iron-doped samples and experimental molar percentage of iron (obtained from EDX data).....	57
Figure (2-9). Extrapolation of the linear portion of the Kubelka-Munk diagram to the x axis (energy/eV) in order to find the band gap for one of the iron-doped TiO ₂ samples.....	58
Figure (2-10). The band gap change by increasing the iron content in titanium dioxide in our study as well as some other publications.....	60
Figure (2-11). SEM images of the synthesized samples according to theoretical molar percentage of doped iron.....	61
Figure (2-12). SEM image of iron (III) oxide nanoparticles.....	62
Figure (2-13). EDX spectrum of the typical iron-doped TiO ₂	63
Figure (2-14). The relationship between the theoretical and the real amount of iron as a dopant, based on the EXD results.....	64
Figure (2-15). EDX analysis of α -Fe ₂ O ₃	64

Figure (2-16). Differential scanning calorimetry (DSC) of three selected iron-doped titanium dioxides.....	65
Figure (2-17). Cyclic voltammetry experiment for iron-doped TiO ₂ (5 mol% Fe). CV is repeated for three cycles.....	66
Figure (2-18). Cyclic voltammetry experiment for iron-doped TiO ₂ (5 mol% Fe).....	68
Figure (2-19). Cyclic voltammetry experiment for iron-doped TiO ₂ (5 mol% Fe) in water (0.1 M potassium perchlorate) and also in acetonitrile and DMF (0.1 M potassium perchlorate).....	69
Figure (2-20). Cyclic voltammetry experiment for iron-doped TiO ₂ (5 mol% and 4 mol% Fe) and pure TiO ₂ in acetonitrile-DMF (0.1 M potassium perchlorate).....	70
Figure (2-21). XRD-pattern of pure anatase, pure brookite and pure rutile. Republished from open-access reference [56] © 2017 by the authors. Licensee MDPI, Basel, Switzerland, https://www.mdpi.com/2073-4344/7/10/304	76
Figure (2-22). EDX experiment for all iron-doped TiO ₂ nanomaterials.....	79
Figure (2-23). Cyclic voltammetry experiment for iron-doped TiO ₂ (5 mol% Fe). Each experiment contains three consecutive cycles.....	81
Figure (3-1). Schematic diagram of a typical confocal microscope. Reprinted by permission from Springer Nature: reference [1]. Copyright © 2010.....	83
Figure (3-2). Schematic diagram of WITec confocal Raman microscope (alpha 300 R+): (01) Excitation laser (02) Optical fiber (03) Objectives (04) Scan table and/or stepper motor (05) Filter set (06) Optical fiber (07) CCD detector (08) White-light illumination [2].....	83
Figure (3-3). Raman spectra of (a) brookite TiO ₂ (b) anatase TiO ₂ . Republished from open access reference [3].© 2017, Monai M.; Montini T.; Fornasiero P.; <i>Catalysts</i> , 2017, 7, 304, https://www.mdpi.com/2073-4344/7/10/304	86
Figure (3-4). The peaks assigned for anatase and brookite in Raman spectrum of iron-doped titanium dioxide (0.7 mol.% Fe) containing 11.75% brookite phase in order to perform Raman imaging.....	86

Figure (3-5). (a) Raman mapping of iron-doped titanium dioxide (0.7 mol.% Fe). The darker areas are richer in anatase and lighter areas are richer in brookite (b) The expanded Raman spectra of point A, point B and total average spectrum of the whole mapped area at ca. 515 cm⁻¹ representing anatase phase (c) The expanded Raman spectra of of point A, point B and total average spectrum of the whole mapped area at ca. 244 cm⁻¹ representing anatase phase.....88

Figure (3-6). The expanded Raman spectra of multiple points in the Raman image from Figure (3-5a) and total average spectrum of the whole mapped area at ca. 244 cm⁻¹ representing anatase phase. The numbers used to label each points are the x and y position of each used pixel from the image.....89

Figure (3-7). Raman mapping of iron-doped titanium dioxide (0.9 mol.% Fe). The lighter areas are richer in anatase and the darker areas are richer in brookite.....90

Figure (3-8). Average Raman spectra of the imaged area for (a) iron-doped TiO₂ (0.7% mol% iron) containing 11.75% brookite phase based on the XRD results (b) iron-doped TiO₂ (0.9 mol% iron) containing no brookite based on the XRD results.....90

Figure (3-9). Raman spectra of pure anatase TiO₂ and pure rutile TiO₂. Reprinted from reference [10] , Copyright © 2000, With permission from Elsevier.....91

Figure (3-10). The peaks attributed to anatase and rutile in average Raman spectrum of the whole mapped Aeroxide P25 for performing Raman imaging.....93

Figure (3-11). (a) Raman image of Aeroxide P25 (c) The expanded Raman spectra taken from point A and point B plus total average spectrum of the whole imaged area.....94

Figure (3-12). The structure of N3 dye. Reprinted by permission from Springer Nature: reference [24]. Copyright © 2013.....95

Figure (3-13). The chemical structure of Z907 dye. Republished with permission of ROYAL SOCIETY OF CHEMISTRY from reference [25], Copyright © 2013. Permission conveyed through Copyright Clearance Center, Inc.....96

Figure (3-14). Raman spectra of pure titanium dioxide (anatase), pure N3 dye in solid state and N3 dye adsorbed on titanium dioxide. Reprinted with permission from reference [26], Copyright © 2011, American Chemical Society.....	97
Figure (3-15). The peaks assigned for titanium dioxide and N3 dye in average Raman spectrum of N3 dye adsorbed on titanium dioxide taken from the whole mapped area.....	98
Figure (3-16). Raman image of N3 adsorbed on TiO ₂ (2) (pure titanium dioxide).....	99
Figure (3-17). Raman image of another area of N3 adsorbed on TiO ₂ (2) (pure titanium dioxide).....	99
Figure (3-18). Raman image of N3 adsorbed on TiO ₂ (1) (pure titanium dioxide).....	100
Figure (3-19). Raman image of N3 adsorbed on iron-doped titanium dioxide with 0.9 mole% Fe.....	101
Figure (3-20). The Raman spectra of Z907 powder (top) and Z907 adsorbed on titanium dioxide. Reprinted with permission from reference [32] , Copyright © 2009, American Chemical Society.....	102
Figure (3-21). The peaks assigned for titanium dioxide and Z907 dye in average Raman spectrum of Z907 dye adsorbed on titanium dioxide taken from the whole mapped area.....	102
Figure (3-22). Raman image of Z907 adsorbed on TiO ₂ (1) (pure titanium dioxide).....	103
Figure (3-23). Raman images for (a) another spot for Z907 adsorbed on TiO ₂ (1) (pure titanium dioxide) (b) Z907 adsorbed on TiO ₂ (2) (pure titanium dioxide) (c) another spot for Z907 adsorbed on TiO ₂ (2) (pure titanium dioxide).....	103
Figure (3-24). Raman images of (a) Z907 adsorbed on iron-doped titanium dioxide with 0.7 mole% Fe (c) another spot for Z907 adsorbed on it.....	104
Figure (4-1). The standard calibration curve of methylene blue concentration and UV-Vis absorption.....	110

Figure (4-2). Photodecomposition efficiency of pure and iron-doped titanium dioxides for removal of methylene blue dye in water at pH 4.5.....	110
Figure (4-3). Photodecomposition efficiency of pure and iron-doped titanium dioxides for removal of methylene blue dye in water at pH 2.4.....	112
Figure (4-4). UV-Vis spectra of methylene blue used in photodegradation reaction at pH 2.4 with (a) pure titanium dioxide (b) Fe-doped titanium dioxide (0.5 mol% Fe).....	114
Figure (4-5). UV-Vis spectra of methylene blue used in photodegradation reaction at pH 4.5 with Fe-doped titanium dioxide (0.5 mol% Fe).....	117
Figure (4-6). UV-Vis spectra of methylene blue used in photodegradation reaction at pH 2.4 with Fe-doped titanium dioxide (0.5 mol% Fe) after 3 times dilution.....	117
Figure (4-7). The linear relationship between PZC and empirical iron percentage in titanium dioxide samples.....	119
Figure (4-8). One of the proposed mechanisms for the photocatalytic degradation of methylene blue. Reprinted from reference [7], , Copyright © 2001, With permission from Elsevier.....	120
Figure (4-9). Tracing of pH during the course of the reaction for methylene blue solution alone at pH 2.4 and methylene blue solution used in photodegradation reaction at pH 2.4 with pure titanium dioxide and iron-doped titanium dioxide (0.5 mol% Fe).....	121
Figure (4-10). UV-Vis spectra of methylene blue used in photodegradation reaction at pH 2.4 with Fe-doped titanium dioxide (4 mol% Fe).....	122
Figure (4-11). Langmuir-Hinshelwood linear transform model for photodegradation reaction of methylene blue at pH=4.5.....	123
Figure (4-12). Relationship between empirical amount of iron as dopant in TiO ₂ and calculated k _{obs} values for photodegradation reaction of methylene blue at pH=4.5.....	124
Figure (4-13). Relationship between the band gap values and calculated k _{obs} values for photodegradation reaction of methylene blue at pH=4.5.....	125

Figure (4-14). Langmuir-Hinshelwood linear transform model for photodegradation reaction of methylene blue at pH=2.4.....126

Figure (4-15). Relationship between empirical amount of iron as dopant in TiO₂ and calculated k_{obs} values for photodegradation reaction of methylene blue at pH=2.4.....127

Figure (4-16). Relationship between the band gap values and calculated k_{obs} values for photodegradation reaction of methylene blue at pH=2.4.....128

List of abbreviations

1. **at.:** Atomic
2. **CB:** Conduction band
3. **CV:** Cyclic Voltammetry
4. **DMF:** Dimethylformamide
5. **DRS:** Diffusive Reflectance Spectroscopy
6. **DSC:** Differential Scanning Calorimetry
7. **DSSC:** dye-sensitized solar cell
8. **EDX:** Energy Dispersive X-ray
9. **E_g:** Band gap energy
10. **FTO:** Fluorine doped tin oxide
11. **HER:** Hydrogen evolution reaction
12. **HOMO:** Highest occupied molecular orbital
13. **IR:** Infrared spectroscopy
14. **IUPAC:** International Union of Pure and Applied Chemistry
15. **LUMO:** Lowest unoccupied molecular orbital
16. **PZC:** point of zero charge
17. **OER:** Oxygen evolution reaction
18. **SCE:** Standard calomel electrode
19. **SEM:** Scanning Electron Microscope
20. **USP:** United States Pharmacopeia

- 21. **UV:** Ultraviolet
- 22. **UV-Vis:** Ultraviolet Visible
- 23. **VB:** Valence band
- 24. **wt.:** Weight
- 25. **XRD:** X-Ray Diffraction

Chapter 1: Introduction

1-1-Outline of the thesis:

This thesis is presented in five Chapters. In Chapter 1, the properties and applications of titanium dioxide are presented followed by a review of what is known about its doping, sol-gel synthesis, important literature related to the application of iron-doped TiO₂ as a photocatalyst, Raman spectroscopy, application of Raman mapping for titanium dioxide characterization as well as the theory regarding Raman imaging of dye-absorbed titanium dioxide. The final section of this Chapter will cover the thesis objectives.

Chapter 2 presents first the details of the synthesis method used for the preparation of pure and iron-doped nanomaterials and synthesis of iron (III) oxide. Then, it discusses the various characterization methods used in this work, such as powder X-ray diffraction (XRD), diffusive reflectance UV-Vis spectroscopy (DRS UV-Vis), scanning electron microscope (SEM), Energy-dispersive X-ray (EDX), Cyclic voltammetry (CV) and differential scanning calorimetry (DSC).

Chapter 3 gives information about the details of the sample preparation and instrumentation employed for Raman imaging, Raman imaging of synthesized pure and iron-doped titanium dioxides, Raman imaging of commercial Aeroxide P25 and Raman imaging of dye-adsorbed TiO₂ films.

Chapter 4 presents the employed experimental details and instrumentation for photodegradation of methylene blue as a model reaction for the study of pure and iron-doped titanium dioxide samples' properties as photocatalysts following by a presentation of the results and discussion.

Chapter 5 concludes the thesis with a presentation of the main achievements of the research presented therein as well as the novelty of the research results and conclusions.

1-2-Introduction

Titanium dioxide (TiO_2) materials have a wide variety of uses in our everyday life, such as pigments [1], in sunscreens [2-3], paints [4], ointments and toothpastes [5]. In sunscreens [2-3], titanium dioxide acts also as UV light absorbent. It is also used not only as a pigment but also helps prevent photodegradation of polymers in plastics when exposed to sunlight. After Fujishima and Honda discovered the water photocatalytic splitting on a TiO_2 electrode under ultraviolet (UV) light in 1972 [6-8], a huge number of studies have been implemented on the photocatalytic and photoelectrochemical applications of TiO_2 materials [9-12]. TiO_2 has a tremendous potential as a photocatalyst in helping to overcome very vital environmental pollution issues [7,11,12-13]. Moreover, due to gigantic energy demand in recent years, applications of TiO_2 materials in solar cells and water-splitting devices for hydrogen production could have an outstanding role in the energy market of the future [9,14-15].

Among all different types of semiconductors that could be potentially used as photocatalyst, titanium dioxide is the only proper candidate for industrial application because of its non-toxicity, high chemical stability, low cost and relatively good photoactivity [16]. However, one of the most serious challenges in application of TiO_2 in photocatalytic, photochemical and photoelectrochemical systems is its insufficient optical properties, especially its wide band gap. The band gap of TiO_2 lies in the UV region (3.2 eV for the anatase phase and 3.0 eV for the rutile phase), which covers only a small portion of the sun's energy (<10%), as depicted in Figure (1-1) [11].

Thus, in term of the performance improvement of TiO_2 , the optical activity should be shifted from UV to visible region. Several methods are employed to achieve this goal. Sensitization of TiO_2 with various organic and inorganic dyes is one of the common ways to enhance its optical activity in the visible region, which is widely applied in dye-sensitized solar cells (DSSCs) [10]. Doping of titanium dioxide with other elements is also another widespread method that leads to a narrow band gap and subsequent enhancement in its optical properties [17].

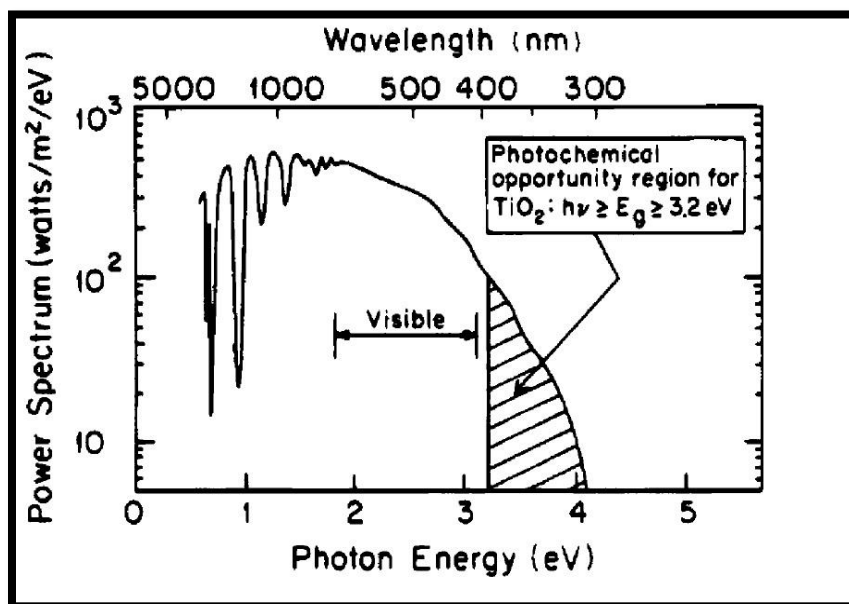


Figure (1-1). Solar spectrum at sea level with the sun at its zenith. Reprinted with permission from reference [11], Copyright © 1995, American Chemical Society.

1-3-Chemical structure of titanium dioxide

Titanium dioxide can be found in three common crystal phases: anatase, brookite and rutile. Rutile is recognized as the most stable form of TiO_2 , whereas brookite and anatase are metastable, which means they can be converted to the rutile structure upon heating.

The anatase and rutile unit cell structures are demonstrated in Figure (1-2). In both crystal structures, Ti^{4+} ion has a coordination number of 6, which means each titanium cation is surrounded by 6 oxygen anions in an octahedral structure. The difference between two structures are the distortion of each octahedron arising from the assembly pattern of octahedral chains. In the rutile structure, the octahedron exerts a slight orthorhombic distortion, while the octahedron in anatase is remarkably distorted resulting in a symmetry lower than orthorhombic. The distance between two adjacent titanium atoms in the rutile phase is shorter than the one is the anatase phase, while Ti-O distance is longer in the rutile phase. Moreover, each octahedron is in direct contact with 10 other neighbor octahedrons, but this number in anatase is only 8. Such structural

differences affect the density and band gap energy of the anatase and rutile phases [17]. The density of anatase and rutile is 3.895 and 4.248 g/cm³, respectively [18]. There is still a debate about the effect of structural differences on the electronic and photocatalytic properties of each TiO₂ polymorphs. Based on a theoretical study, it is claimed that anatase is an indirect band gap semiconductor, while rutile and brookite are direct band gap semiconductor. Thus, the lifetime of photo-generated electrons and holes is higher in the anatase phase leading to a better photochemical activity. Moreover, the anatase phase possesses the lowest average effective mass leading to the fastest migration of electrons and holes from the bulk to the surface of titanium dioxide [19].

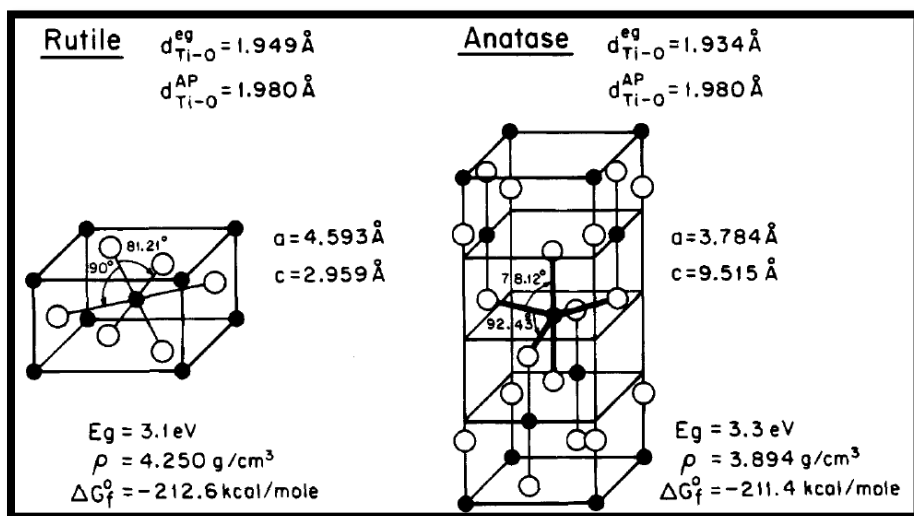


Figure (1-2). Crystal structure of anatase and rutile. Reprinted with permission from reference [11], Copyright © 1995, American Chemical Society.

The brookite phase possesses an orthorhombic crystal structure unlike the anatase and rutile ones but with a tetragonal crystal system. In contrast to anatase, where only the edges of each octahedron is shared with other octahedra, in both the brookite and rutile phases, the octahedra are connected to each other both through their corners and edges (Figure (1-3)) [20].

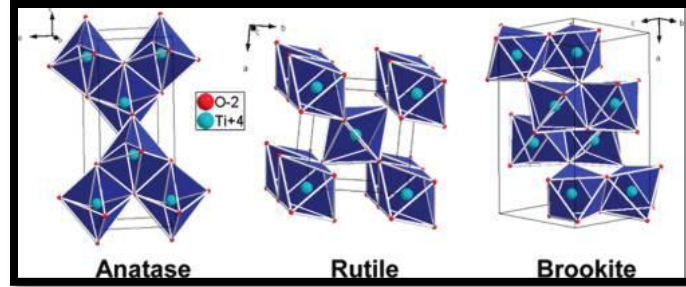


Figure (1-3). crystal structure of anatase, rutile and brookite. Reprinted with permission from reference [20], Copyright © 2010, American Chemical Society.

1-4-Doping

As discussed, doping is one of the major routes to improve the properties of TiO_2 . The main objective of doping is introducing intra-band gap states leading to more absorption of visible light. This new intermediate energy level can act both as electron acceptor and electron donor, which ultimately allow titanium dioxide to absorb visible light [21]. In addition, doping can change the electronic structure of semiconductors by introducing defects and oxygen vacancies in the crystal lattice, which could form a forbidden band. With transition metals as dopant, the t_{2g} energy level is a fundamental factor to determine the final band structure of doped titanium dioxide. By increasing the atomic number of the dopant, the localized energy level shifts to lower energy. This arises from the alteration of t_{2g} energy level of transition metals across a period in the periodic table. For example, the energy band resulting from doping with chromium lies almost in the middle of the band gap. But, this band lies closer to the valence band with iron and it lies closer to the conduction band with vanadium (Figure (1-4)) [22].

Much work has been reported on the doping of titanium dioxide with different elements including metals and nonmetals with wide variety of preparation methods. These methods can be categorized into three main paths: wet chemistry, high temperature treatment, and ion implantation on TiO_2 . The wet chemistry method includes hydrolysis of a precursor mostly titanium alkoxide in the presence of the other reagents followed by heating to obtain crystalline powder. Sol-gel process is the best-known method beyond wet chemistry methods. High temperature treatment and ion implantation on TiO_2 are also two other methods that can be

employed for doping. High temperature treatment is normally used for doping nonmetals into TiO₂ lattice. Heating titanium carbide [23] or annealing TiO₂ under CO gas flow at high temperature [24] generate carbon doped TiO₂ and are examples of high temperature treatment method. The ion implantation is quite expensive and it requires highly crystalline TiO₂.

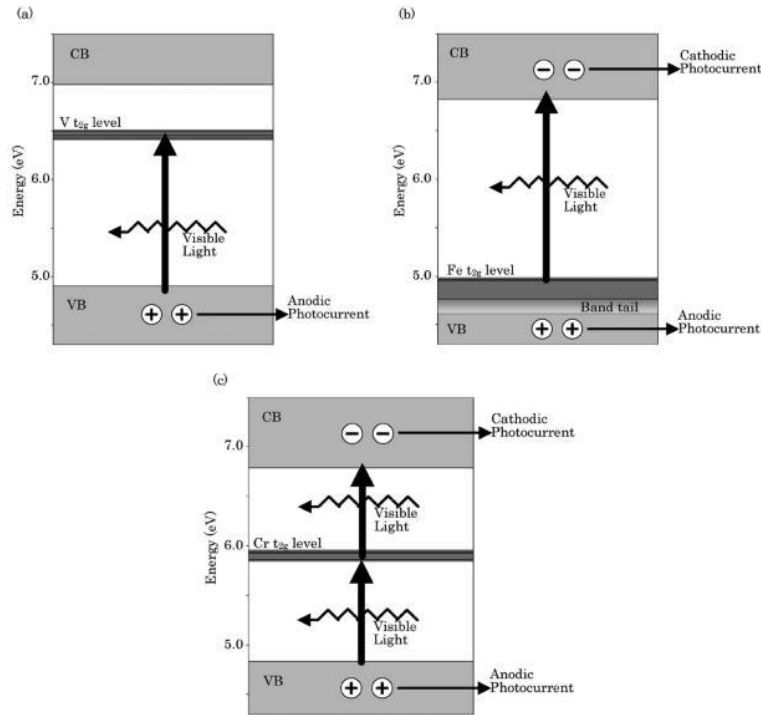


Figure (1-4). Photoexcitation process in (a) V-doped TiO₂ (b) Fe-doped TiO₂ (c) Cr-doped TiO₂. Reprinted from reference [22], Copyright © 2002, With permission from Elsevier.

1-5-Sol-gel method for production of TiO₂ materials

The sol-gel method is a well-known process in manufacturing various ceramic materials [25-26]. In this process, as a result of hydrolysis and polymerization reactions of the precursors, a colloidal suspension or sol is formed. The precursors, which are commonly employed are inorganic metal salts or metal organic compounds such as metal alkoxides. Then, the liquid sol is converted to solid gel by completion of the polymerization reaction or solvent loss. The solid ceramic is finally made by drying and further annealing of the formed gel.

In terms of sol-gel process, TiO_2 materials are manufactured usually via an acid-catalyzed hydrolysis reaction of titanium (IV) alkoxide followed by condensation [27-29]. The conditions of the reaction affect the growth of Ti-O-Ti chain. Low concentration of water in reaction media, low hydrolysis rate and excess amount of titanium alkoxide lead to development of Ti-O-Ti chain. As hydrolysis rate and water percentage elevate in the reaction mixture, formation of $\text{Ti}(\text{OH})_4$ is favored. In other words, when the ratio of water to titanium precursor is high, the hydrolysis of titanium alkoxide is rapid and completion of nucleation and growth is very short. Consequently, the formed titanium dioxide particles are smaller and more unstable leading to precipitation of large aggregates. [27-29].

Among different synthetic methods for the preparation of TiO_2 materials, the sol-gel method has been selected, as it is the most efficient, simple and common way for synthesizing doped titanium dioxides.

1-6-Iron as a dopant for titanium dioxide

Between various elements from the periodic table, iron has been chosen initially as dopant because of the following reasons:

1-Iron is cheap and abundant in nature. Since these kinds of materials have the potential to be applied as a commercial product such as solar cell or photocatalyst, it is recommended to manufacture them from low cost abundant materials.

2-Moreover, iron has very low toxicity and can be found in biological systems. It also has no environmental issue compared to heavy metals.

3-For coordination number 6, the ionic radius of Ti^{4+} and Fe^{3+} are almost the same, 0.68 and 0.64 Å [31], respectively. Thus, iron can be a suitable candidate to insert into TiO_2 matrix.

4-Among transition metals, iron is one of the metals able to trap both electrons and holes after photoexcitation by producing Fe^{2+} and Fe^{4+} , respectively. This resulted in higher efficiency in photocatalytic and photoelectrochemical systems [31].

1-7-Photochemical activity of titanium dioxide

After Fujishima and Honda [32] reported the photoelectrochemical water splitting reaction on TiO₂ electrode in 1972, a novel green chemistry approach has rapidly grown in various areas, such as hydrogen generation [32-35], air purification [36-39], water purification [40-42] and anti-bacteria coating [36,43]. Among all types of semiconductor-based photocatalysts, titanium dioxide is the most appropriate candidate for industrial applications due to its good photoreactivity, high chemical stability, nontoxicity as well as low cost of production [44]. However, TiO₂ suffers from insufficient optical properties due to its wide band gap. This confines the photocatalytic activity of titanium dioxide solely to ultraviolet region, which covers only a small fraction of the sun's energy [11]. Thus, it is a point of interest for many material scientists to synthesize modified TiO₂, which is capable to absorb light in the visible region in order to provide accessibility to a larger area of solar spectrum. Several methods are employed to achieve this goal such as sensitization of TiO₂ with various organic and inorganic dyes as well as doping of titanium dioxide with other elements. The core objective of doping is to introduce intra-band gap states leading to higher absorption in the visible region. As a result, in comparison to pure TiO₂, a photon with lower energy is required for transferring electron from these new energy levels to the conduction band.

1-8-Principles of semiconductor-based photocatalysis

The first documented photocatalysis based on the semiconductors was reported in 1921 by Renz, which consisted in showing a dye solution decolorizing reaction during illumination with sunlight in the presence of titanium dioxide and some other metals oxides [45]. Another paper, which was published in 1938, shed light on the fact that active oxygen species on the surface of titanium dioxide can be detected under UV illumination [46]. It was postulated that these species are responsible for the photobleaching of the dyes.

The schematic mechanism of photocatalysis at a semiconductor nanoparticle is demonstrated in Figure (1-5) [47]. The process is triggered by photon absorption containing equal or larger energy than the semiconductor band gap. This phenomenon results in an electron (e⁻) being excited from the valence band (VB) to conduction band (CB) followed by formation of a hole

(h^+) in the valence band. Each of these separated charges (e^- and h^+) can participate in different processes as represented in Figure (1-5).

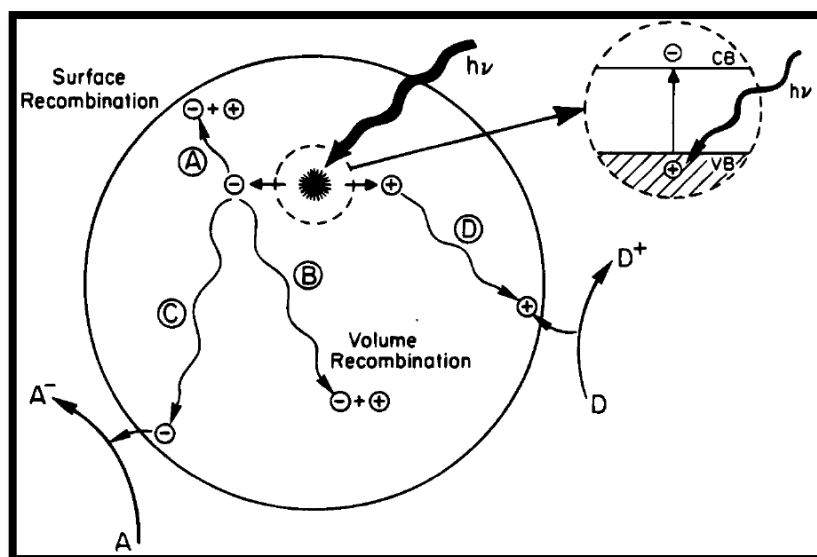


Figure (1-5). Schematic photoexcitation and deexcitation events in a semiconductor.

Reprinted with permission from reference [47], Copyright © 1995, American Chemical Society.

Recombination of electron and hole is detrimental to the performance of the material. It is one of the possible pathways that can occur either on the surface (path A) or in the bulk of the semiconductor particle (path B). Overall, recombination decreases the photocatalytic activity, since it does not allow any free radicals production that are required to promote subsequent catalytic reactions. For a photocatalytic process to occur, the generated electron and hole must migrate towards the surface of the semiconductor particle. On the particle surface, the electron can reduce an electron acceptor species (path C) while the hole can oxidize an electron donor species (path D). Since the life of both negative and positive charge carriers (electron and hole) is very short, both electron acceptor and electron donor species should be either adsorbed on or be very close to the surface of the semiconductor particles for a reaction to occur.

In terms of kinetics, the photon absorption takes place on the order of 10^{-15} s, which is considered a fast process. Recombination happens in the range of picoseconds to nanoseconds [47]. Overall, all the events taking place on the surface of titanium dioxide are faster than the

ones occurring in the bulk (Figure (1-6)) [48a]. However, these events do not always happen in such a fast pace. It has been proven that Ti^{3+} can act as an effective electron trap in the TiO_2 lattice. For example, it was shown that plasma treatment of TiO_2 forms Ti^{3+} as well as oxygen vacancies and that increasing the treatment time increases the amount of Ti^{3+} [48b]. In another study, the number of Ti^{3+} sites is increased using a hydrogen reduction treatment. This was shown to ultimately facilitate charge separation and charge transport [48c].

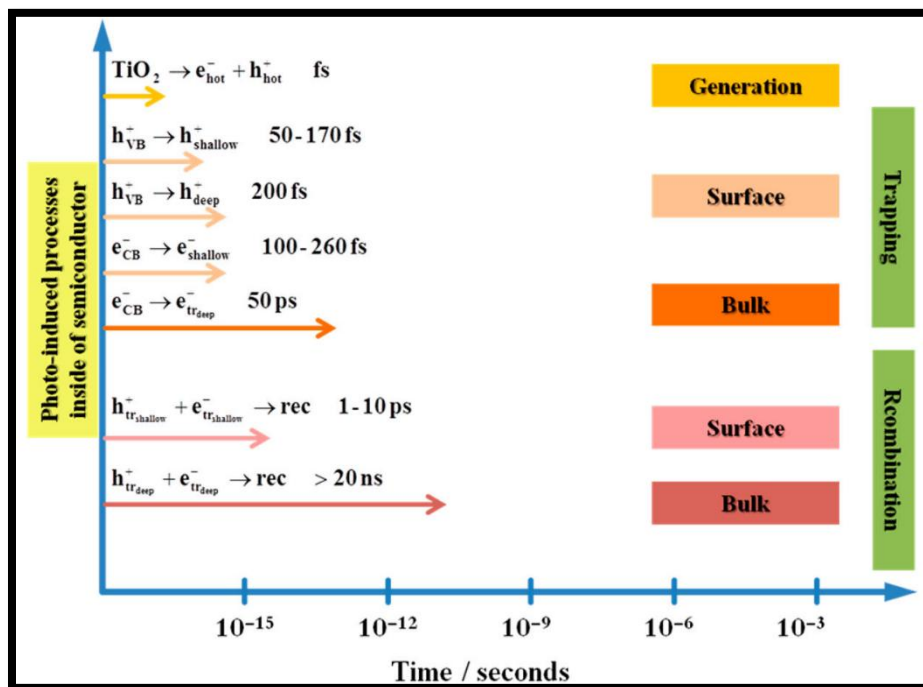
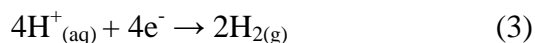
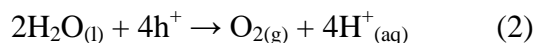
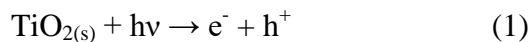


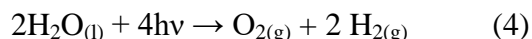
Figure (1-6). Time scales for photoinduced reactions in titanium dioxide. Reprinted with permission from reference [48a], Copyright © 2014, American Chemical Society.

1-8-1-Mechanism of photocatalyzed dye degradation: As it was mentioned earlier, Fujishima and Honda [32] were the first to report the photoelectrochemical water splitting reaction on TiO_2 electrode. They used titanium dioxide electrode connected via an external circuit to a platinum counter electrode. When UV light illumination was applied, a photocurrent was observed. Also, oxygen was released at the TiO_2 electrode (oxidation reaction) while hydrogen was produced at the platinum electrode (reduction reaction), simultaneously. The breakthrough in this process

was the decomposition of water into hydrogen and oxygen gases without applying any external voltage. The proposed mechanism can be depicted in the following steps:

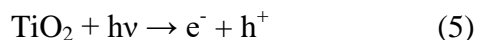


The overall reaction is:



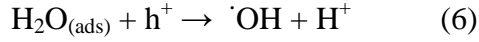
This report coincided with the Oil Crisis of 1973, consequently, the scientific community became motivated to find novel energy resources that can replace crude oil. Hydrogen was identified as one of the promising fuel to address this crisis, which led to development of the field of solar energy conversion for hydrogen production [44,49-51].

By the end of 20th century, a gradual shift of the use of titanium dioxide as photocatalyst towards environmental applications took place. Decomposition of cyanide and sulfite in water has been reported by Frank *et al.* in 1977 [52-53]. Since then, a great amount of research has been performed in the field of removal of harmful organic chemicals as pollutants in water and air [48a,54-56]. There are two significant differences between this process compared to water-splitting system. First of all, both oxidation and reduction reactions happen on the titanium dioxide surface without employing any counter electrode. Secondly, there is no requirement to use an external circuit. Consequently, the overall design and handling of the experiment is simpler. The overall reaction steps which is known as indirect degradation mechanism are summarized below [55]:



The second step comprises the reaction between water and generated holes in the valence band of titanium dioxide which results in the formation of hydroxyl radicals. These radicals are extremely powerful oxidizing agents and form very close to the surface of the catalyst. As a result, they attack either adsorbed organic molecules or the ones that are located very close to the

surface of TiO₂ in a non-selective way, causing them to be mineralized fully or partially based on their chemical structure and stability:



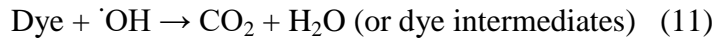
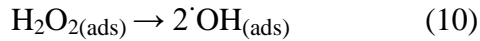
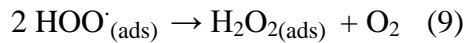
The next step can happen at the same time as step 6 and is the oxygen reduction by the produced electron in the conduction band of titanium dioxide. The source for O₂ is atmospheric oxygen, which can then become dissolved and adsorbed on the surface of TiO₂. The product is anionic superoxide radical:



The generated superoxide ions are consumed in further oxidation reactions as well as inhibiting electron-hole recombination. The protonation of superoxide ion yields to hydroproxyl radical:



Two hydroproxyl radical combine to generate hydrogen peroxide plus oxygen. Finally, hydrogen peroxide is converted to two active hydroxyl radical:



The whole process is demonstrated in Figure (1-7), schematically [55].

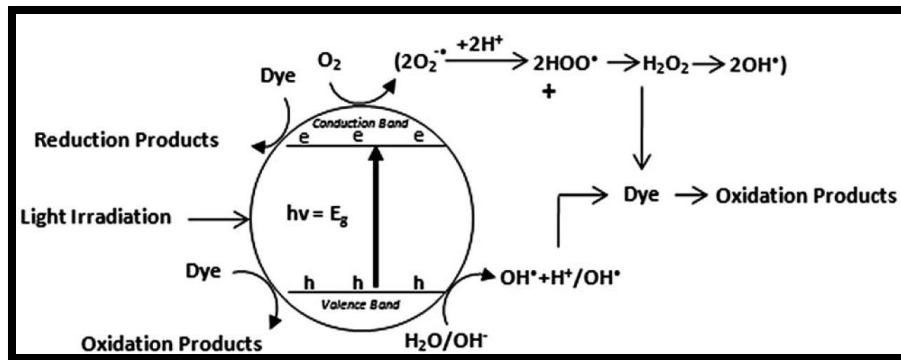
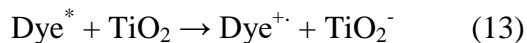


Figure (1-7). Schematic representation of indirect photocatalytic dye degradation.
 Republished with permission from reference [55], Copyright © 2014, RSC Publishing.

The other type of proposed mechanism, which is called direct photocatalytic degradation, involves the dye excitation from its ground state to a triplet state under illumination of a visible light photon. The dye in the excited state injects one electron into the conduction band of titanium dioxide leading to the formation of a semi-oxidized radical cation dye. Trapped electrons and dissolved oxygen in the system form superoxide radical anions which are ultimately converted to active hydroxyl radical in a similar path described for the indirect mechanism (Figure (1-8)) [55]:



Many studies reveal that the indirect pathway is dominant over the direct one [57-59]. Some researchers claim that in terms of kinetics, the direct mechanism is far slower than the indirect mechanism [57,60].

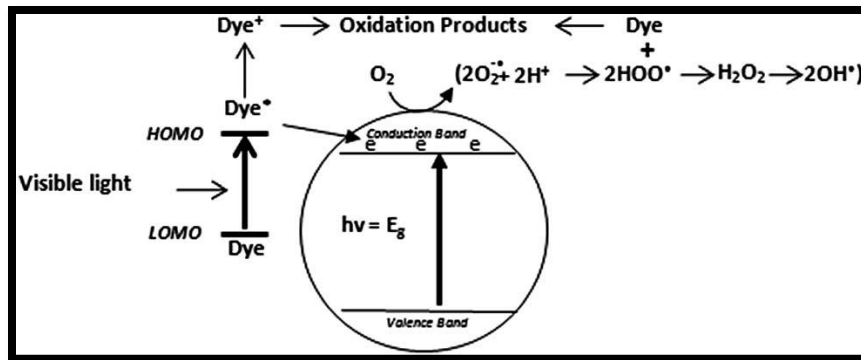
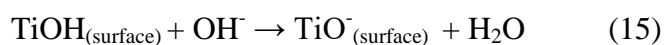
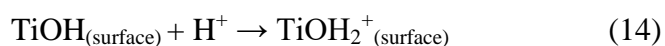


Figure (1-8). Schematic representation of direct photocatalytic dye degradation.
 Republished with permission from reference [55], Copyright © 2014, RSC Publishing.

1-9-Effect of pH on the photocatalytic reactions

pH plays a major role in photocatalytic degradation of dyes by affecting the mechanism in various ways. It can alter the adsorption of dye on the surface of titanium dioxide by influencing both the surface charge of the catalyst and the charge of the dye molecule. It has been shown that pH effect is correlated to surface-charge properties of the TiO₂ and it can be described by the point of zero charge (pzc) concept [61]. Alaton *et al.* determined that for commercial P25 titanium dioxide, the point of zero charge is at pH=6.8 [62]. That means at any pH lower than 6.8, the surface of TiO₂ is positively charged and at any pH higher than 6.8, the surface consists of negative charges based on the following chemical equations:



Since the surface of titanium dioxide possesses positive charges on its surface (below pzc), anions and negative-charged species can be attracted and adsorbed on the TiO₂ surface while cations and positive-charged species are repelled from the catalyst surface. The opposite situation is likely to take place above the pzc. For example, methyl orange is discolored at higher rate at pH=2 due to electrostatic interaction between methyl orange anions and positive charges on the surface of titanium dioxide [61]. The same trend has been observed for another dye called acid yellow 17 which displayed the highest removal rate at pH=3 [63]. Mendret *et al.* reported

higher degradation rate of acid orange 7 as an anionic dye at pH=4 by proposing that the changes in electrical charge of the dye molecule should be considered in addition to electrical charges on the surface of TiO₂ during the pH change. At pH values below the pK_a value, the dye molecule exists as a neutral species while at higher pH values than pK_a, the dye molecule carries a negative charge [64]. In principle, there is a complex electrostatic interaction between photocatalyst surface, solvent molecules, substrate and formed radicals which are all remarkably dependent on the pH of the solution. Some protonated products can even be more stable than their neutral structure under UV radiation [65].

pH variation impacts not only the surface charges of the photocatalyst, but also the reaction mechanism itself. While at neutral or basic pH, hydroxyl radicals are predominantly responsible for oxidation, at acidic pH values, positive holes are dominant oxidizing species because hydroxyl radicals can only be produced at higher pH values. Although hydroxyl radicals can be produced properly at alkaline pH, the created negative charges on the surface of the catalyst is unable to adsorb dye anions due to electrostatic repulsion [66].

Typically, titanium dioxide exerts higher oxidizing activity at lower pH values. However, very high concentration of H⁺ can suppress the reaction rate as well. The reason behind it comes back to the tendency of titanium dioxide particles to agglomerate at low pH, which causes a reduction of the surface area and subsequently light absorption [67-69]. The effect of pH change on photocatalytic degradation rate can also be illustrated by the electrical double layer of solid-electrolyte interface which can act not only as the barrier for separating photogenerated electron and hole, but also adsorption-desorption of molecules on the surface of TiO₂ [70].

1-10-Kinetics of photocatalytic reactions

It is well-known that the reaction kinetics of photocatalytic processes are very complex. However, it was empirically discovered that the degradation of one single compound obeys first-order kinetics on the basis of the Langmuir-Hinshelwood (L-H) model [71-72]:

$$r = -\frac{dC}{dt} = \frac{kK_{ads}C}{1+K_{ads}C} = k_{obs}C \quad (16)$$

Where:

$$k_{\text{obs}} = \frac{kK_{\text{ads}}}{1+K_{\text{ads}}C} \quad (17)$$

r = reaction rate

C = substrate concentration

K_{ads} = Langmuir-Hinshelwood adsorption equilibrium constant

k = pseudo-first order rate constant (attributed to surface reactions on TiO_2)

Equation (17) can be rearranged as below:

$$\frac{1}{k_{\text{obs}}} = \frac{1}{kK_{\text{ads}}} + \frac{C}{k} \quad (18)$$

$$-\ln \frac{C_t}{C_0} = k_{\text{obs}}t \quad (19)$$

C_0 = initial substrate concentration

C_t = remaining substrate concentration

t = irradiation time

The observed rate constant (k_{obs}) for each reaction is calculated by plotting $-\ln \frac{C_t}{C_0}$ versus irradiation time. This value is unique under the conditions of the reaction and any change in pH, temperature, radiation intensity or catalyst loading can alter the obtained constant.

1-11-Reported iron-doped titanium dioxides as photodegradation catalysts

Application of iron-doped titanium dioxide materials as photodegradation catalysts have been studied from different perspectives. In order to have a meaningful view, the literature survey presented below is organized based on the main contribution of each study to the field of photodegradation catalysis and the survey is limited to the use of iron-doped TiO_2 .

1-11-1-Iron-doped titanium dioxide materials used as photodegradation catalysts with focus on synthetic methods: Addition of iron as dopant has a significant impact on the structure of titanium dioxide. Ambrus *et al.* have synthesized iron-doped titanium dioxide within the range between 0 to 10.0 at.% iron. The samples containing low iron (0-1.2 at.%) are dominantly anatase while increasing the amount of iron elevates the amount of amorphous phase. However, no crystalline phase of iron oxide is observed [73]. Increasing the content of iron decreases the particle diameter as it increases the specific surface area. The photocatalyst with 3.0 at.% of iron acts as the most active one in photodegradation reaction of phenol under UV-Vis light [73]. Also, the effect of iron as dopant in phase transition from anatase to rutile has been studied [74]. The extent of phase transition is higher when the load of iron is below 1 mol% in titanium dioxide. A further increase in iron concentration leads to a suppression of phase transition. It has been shown that a composition containing ~ 90 % rutile and remaining anatase exhibits the highest photocatalytic activity [74].

Several synthesis methods for preparation of iron-doped have been proposed. The sol-gel method is one of the most common one, although, there are other ways to prepare Fe-doped TiO₂. Wang *et al.* have investigated the effect of synthesis method of iron-doped titanium dioxide on the photodegradation efficiency of methanol [75]. Three different sol-gel synthesis routes were used for the preparation of iron-doped TiO₂ materials where each used a different type of precursor. All iron-doped titanium dioxides prepared using organic precursors, showed the highest quantum yields. It is concluded that organic precursors have an advantage over inorganic ones in terms of production of materials with an enhanced photoefficiency [75]. Long term sol-gel synthesis (aging time of two months) is applied to obtain well-dispersed iron-doped titanium dioxide particles with different amount of iron up to 7.7 atom% [76]. The best photodegradation results belong to 1 atom% Fe-doped TiO₂, in which 73 % of rhodamine B is degraded after 120 min under standard AM1.5G visible-light illumination [76]. Moreover, the effect of using vinyl-containing ionic liquid as a reaction medium for the synthesis of iron-doped titanium dioxide samples is also studied [77]. It has been determined that the samples made in vinyl-containing ionic liquid (1-Vinyl-3-propylimidazolium iodide) have higher photocatalytic activities due to morphological and structural changes leading to enhanced light absorption in the visible region [77]. In another study, removal of nitrobenzene from water assisted by iron-doped titanium dioxide is reported by Crişan *et al.* [78]. Among 4 different manufactured iron-doped TiO₂

nanopowders with 0.5, 1, 2 and 5 wt.% iron, the one with 0.5 wt.% iron calcined at 400 °C was the best photocatalyst. It is deduced that calcination temperature after sol-gel synthesis of TiO₂ materials is one of the crucial factors influencing the crystal structure and properties of titanium dioxide [78]. Tabasideh *et al.* have worked on sonophotocatalytic degradation of diazinon using iron-doped TiO₂ nanoparticles [79]. It has been demonstrated that the rate of degradation is higher when a combination of ultrasonic waves and UV is applied compared to photodegradation only under UV light. Moreover, among iron-doped TiO₂ powders with 1, 1.5 and 2% iron, the one with 1.5% iron expresses the highest efficiency [79]. Structure and morphology of nanostructures play an important role in photocatalysis. For example, iron-doped TiO₂ nanotubes, synthesized via ultrasonic-assisted hydrothermal route with iron as dopant up to 7 wt.%, are tested as photocatalysts for removal of Reactive Brilliant Red X-3B [80]. All of the iron-doped TiO₂ nanotubes show higher catalytic activities in comparison to pure TiO₂ nanotubes. Incorporation of iron into TiO₂ structure causes alterations in terms of phase composition, particle size and surface area [80].

Ion impregnation is also used as one of the preparation methods for iron-doped titanium dioxide. For example, iron-doped titanium dioxide in the range of 0.5 to 5 wt.% iron load have been prepared from commercial P25 titanium dioxide plus iron (III) acetylacetonate [81]. The XRD diffraction pattern indicates that for samples containing 3-5 wt.% iron, α -Fe₂O₃ are detected as a separate phase representing that iron is not properly embedded into the matrix of titanium dioxide. Thus, this synthesis route is not reliable enough for effective production of Fe-doped TiO₂. Photodegradation of oxalic acid in oxygen-saturated aqueous suspension of catalyst under near-UV irradiation demonstrates that pure titanium dioxide (P25) has the highest photocatalytic performance. However, in between all iron-doped titanium dioxides, the one with 2 wt.% iron shows the best results in terms of photodegradation efficiency [81]. Yen *et al.* have also made thin films of iron-doped TiO₂ by employing ion implantation method [82]. Compared to pure TiO₂ film, a higher photocatalytic activity for iron-doped TiO₂ films are recorded. However, the yield of all photodegradation reactions are very low [82].

1-11-2-Iron-doped titanium dioxide thin films used as photodegradation catalysts:

Preparation of iron-doped TiO₂ is not confined only to bulk synthesis. Thin films of Fe-doped TiO₂ are also manufactured. Iron-doped TiO₂ coatings on microscope glass slides and

polycarbonate plates are fabricated for self-cleaning applications by Carneiro *et al.* [83]. The films deposited on glass substrates are determined to be anatase, while the ones deposited on polycarbonate films are amorphous. The absorption wavelength is shifted towards visible region with increasing the iron concentration. Photodegradation of rhodamine B under UV illumination has been chosen to evaluate the photocatalytic behavior of prepared films. The coating deposited on polycarbonate plastic containing low content of iron possesses the highest photochemical activity [83]. Thin films of iron-doped TiO₂ (0.5, 1 and 2 wt%) are also prepared by spray pyrolysis method on glass substrate [84]. For the one with lowest iron content, thermal treatment at 673 K led to a higher super-hydrophilic performance and consequently the best yield of nitrobenzene removal from water as a model contaminant [84].

As a comparison study, Nagaveni *et al.* have studied the effect of doping titanium dioxide with different metals including iron by utilizing 4-nitrophenol as a model pollutant in photodegradation experiment [85]. Among various selected metals (Cu, V, Zr, Ce, W and Fe), iron-doped TiO₂ expressed the highest photodegradation activity under UV exposure. However, in this study, the load of each metal in titanium dioxide is different. Consequently, it is not easy to compare the obtained results with each other [85].

1-11-3-Organic molecules applied as model pollutant in photodegradation studies with iron-doped titanium dioxide materials: Several organic molecules as model pollutant in photocatalytic decomposition studies for iron-doped TiO₂ have been applied. Wang *et al.* have synthesized iron-doped titanium dioxides with various percentages of iron from 0.05 at.% to 20 at.% [86]. Photodegradation of methyl orange is tested with all samples in order to correlate the amount of iron in TiO₂ to photocatalytic efficiency of this reaction. It is claimed that titanium dioxide containing 1 at.% iron expressed the highest photodegradation activity under visible light due to narrowing of the band gap [86]. Delekar *et al.* also have manufactured three iron-doped titanium dioxides with an iron amount of 1, 2 and 3 mol% through sol-gel method [91]. Based on their experiments, it has been proved that iron-doped TiO₂ with 3 mol% iron acts as the best photocatalyst in terms of photodegradation of rhodamine 6G. This outcome is attributed to lower band gap energy, higher surface area and higher number of hydroxyl groups on the surface of TiO₂ as a result of doping with iron [91].

Dyes are not the only molecules employed in photodegradation reactions. Study of the photocatalytic degradation of phenol with iron-doped TiO₂ materials has shown that between the synthesized Fe-doped titanium dioxides from 0.2 to 10 mol% of iron, the one that has 0.5 mol% gives the best result [87]. It is explained that this optimum concentration of iron is as result of a balance between the excited electron-hole traps by Fe³⁺ centers and the recombination of electron-hole on Fe³⁺ energy levels [87].

Four reports have been found for photodegradation of methylene blue by iron-doped titanium dioxide (Table (1-1)). Nanotube array films of titanium dioxide have been doped by exposing them to iron (III) nitrate solution during their synthesis via electrochemical anodic oxidation of pure titanium dioxide [88]. In this study, the amount of iron is characterized in none of the samples, exactly. It is claimed that there is a correlation between the concentration of the iron (III) nitrate solution used for each synthesis and the real load of iron in titanium dioxide matrix. Photodegradation of methylene blue is utilized as a reaction to evaluate the photocatalytic activity of manufactured iron-doped titanium dioxides. The sample, which is synthesized by the iron (III) nitrate with concentration of 0.1 M, demonstrates the highest photochemical activity in comparison to the two other samples, which are prepared by iron (III) nitrate solutions with concentrations of 0.05 M and 0.15 M [88]. The relationship between the presence of iron dopant ions in TiO₂ structure and properties of the iron-doped TiO₂ has been investigated by Fàbrega *et al.* [89]. It has been determined that iron has control on grain size of particles as well as introducing brookite phase. The impact of annealing temperature of iron-doped TiO₂ on photodegradation of methylene blue dye indicates that increasing the annealing temperature from 400 °C to 800 °C has a negative effect on the kinetics of this reaction [89]. Ganesh *et al.* have conducted an extensive study on photodegradation of methylene blue by iron-doped titanium dioxide with various percentages of iron from 0.1 to 10.0 wt.% iron [90]. Iron-doped titanium dioxide with 0.1 wt.% iron possesses the highest photocatalytic activity in terms of methylene blue photodecomposition under irradiation of simulated solar light. All the Fe-doped TiO₂ powders follow the Langmuir-Hinshelwood first order reaction rate model in this photocatalytic reaction [90]. Manu *et al.* have tested the photodegradation efficiency of methylene blue dye by iron-doped TiO₂ materials synthesized within the range of 0 to 25 at.% [95]. They have found that iron doped TiO₂ photocatalysts with 1, 2 and 5 at.% of iron express higher photocatalytic activity than pure titanium dioxide [95].

Table (1-1). Comparison between different Fe-doped TiO₂ used for photodegradation of methylene blue.

Reference No.	The range of iron load used to dope TiO ₂	The load of iron in the best Fe-doped TiO ₂ photocatalyst	The phase of the best Fe-doped TiO ₂ photocatalyst	Photodegradation percentage of methylene blue after running the reaction for 3 hrs	k _{obs} value for the best Fe-doped TiO ₂ photocatalyst (min ⁻¹)
[88]	0-0.15 M Fe(NO ₃) ₃ *	0.10 M Fe(NO ₃) ₃ *	anatase	Not shown	0.0162
[89]	0-0.65 mol%	0 mol%	anatase	100	Not shown
[90]	0-13.7 mol %	0.14 mol%	anatase	>90	0.00823
[95]	0-25 mol%	1 mol%	anatase	>40 (after 2 hrs)	0.0035**

* In this study, the amount of iron in the samples is not characterized quantitatively. The authors claimed that there is a correlation between the concentration of the iron (III) nitrate solution used for each synthesis.

** In the original paper, the value is listed as 0.0035 s⁻¹ [95], however, when the k_{obs} is calculated based on the data reported in ref. 95 a value of 0.0035 min⁻¹ is obtained.

1-11-4-Mechanism of the photodecomposition reaction promoted by iron-doped TiO₂ materials: The mechanism, in which iron acts as a dopant in titanium dioxide lattice, is a matter of long and controversial discussion between material scientists. One of the studied parameters in this regard is acid-base properties of titanium dioxide. Photo-oxidation of phenol as model pollutant in water is examined by a series of iron-doped TiO₂ samples with different percentages of iron [92]. The maximum photocatalytic activity enhancement is observed for doping level of ~1 wt.% attributed to effective introduction of iron into the structure of titanium dioxide. Modification of acid-base characteristics of TiO₂ as a result of iron doping is one of the critical factors leading to improvement of catalytic activity alongside with changes in electrochemical properties of TiO₂. Existence of high level of iron in titanium dioxide causes high amount of surface segregation of iron-containing phases, which is ultimately leading to lower photodegradation efficiency of the samples with significant content of iron [92]. Also, Carbajo *et al.* have utilized iron-doped TiO₂ with three different iron contents (0.72, 1.6 and 3.4 wt%) to

explore the photodecomposition of ethidium bromide, which is a non-radioactive marker in electrophoresis for visualization of nucleic acid bands [97]. The mechanism of ethidium bromide decomposition is dominated by initial absorption of this molecule on the surface of the catalyst whose strength is dependent on acid-base surface properties of the employed TiO₂. The chemisorption process is favored by slightly basic surfaces corresponding to TiO₂ with lowest iron content. However, the sample with 1.6% of iron gave the best outcomes since, the chemisorption is not the only factor taking part in photocatalysis [97].

In another study, the impact of illumination wavelength on the mechanism of photocatalytic reaction has been evaluated by the photocatalytic oxidation of the azo dye Orange II (Or-II) using iron-doped titanium dioxide under different illumination set-ups [93]. The performance of all iron-doped TiO₂ samples are higher under simulated solar light irradiation than UV radiation. This suggests the recombination of the photogenerated electron-hole pair under UV exposure. Two oxidation pathways have been proposed for Orange II molecule: (1) Degradation of dye due to the charge injection from dye molecule in excited state to the TiO₂ (2) Oxidation through oxidized species produced on the surface of the catalyst [93].

The difference between electron transfer in pure TiO₂ versus iron-doped TiO₂ in photo-oxidation reaction has been studied by Dukes *et al.* [94]. Low level of iron doping (0.5 %) changes the photo-oxidation properties of titanium dioxide. Iron-doped TiO₂ requires molecular oxygen to accept the photogenerated electron. Iron acts as recombination center in the absence of oxygen. Conversely, undoped titanium dioxide transfers the hole rapidly to an electron donor. Extension of absorption edge towards visible region upon doping with iron does not play a significant role in photo-oxidation efficiency. This contradicts the common motivation of doping, which is decreasing the band gap because low doping level introduces only an interband state that can effectively traps electrons. The reaction rate is elevated by factor of 2.95 for 0.5 % Fe-doped titanium dioxide in the photo-oxidation reaction of methanol to formaldehyde and by factor of 2 for 1.0 % Fe-doped TiO₂ [94].

The distribution of iron in the TiO₂ nanoparticles is of remarkable importance in photodegradation reactions. XRD analysis and micro-Raman data have proved that concentration of iron as dopant is higher near the grain boundary of titanium dioxide due to self-purification mechanism [95]. It is concluded that the sharp decrease in photocatalytic activity of the samples

with higher iron contents is correlated to this phenomenon. Among all samples from 1 to 20 at.% of iron, the one with the lowest amount of iron gives the highest photodegradation performance [95].

The surface area of iron-doped TiO₂, as heterogeneous catalyst, is one of the multiple essential factors in photocatalysis. The photocatalytic mineralization of oxalic acid under simulated solar light (1.5 AM) over iron-doped titanium dioxide catalyst was evaluated by determination of the formation rate of carbon dioxide and hydrogen gas [96]. It has been found that mineralization of oxalic acid is proportional to the surface area of the studied photocatalysts. Also, the lower the optical band gap, the higher the photocatalytic activity. Introduction of iron promotes the production of redox sites, which are capable of absorbing photon from visible light region [96].

Different models for the kinetics of the photodegradation reaction on iron-doped TiO₂ have been proposed. Milis *et al.* have studied photo-oxidation of nitrite ion using iron-doped titanium dioxide with various amount of iron in TiO₂ structure ranging from 0.2 to 10 wt.% [98]. The outcome of this study indicated that nitrite photo-oxidation obeys zero-order kinetics for all tested iron-doped TiO₂ samples, which is in contrast with pure titanium dioxide following the Langmuir-Hinshelwood kinetics. The iron-doped TiO₂ with 0.5 wt.% of iron is recognized as the most photoactive catalyst. The rate constants are suppressed with increasing pH value. This phenomenon is understood on the basis of electrostatic interactions between charged titanium dioxide particles and nitrite ions [98]. There is also one report, in which an oxidizing agent has been used to promote the photodecomposition reaction. Photodegradation of Acid Blue 80 dye under UV has been conducted by employing iron-doped titanium dioxide synthesized via ultrasound assisted approach [99]. The reaction kinetics follows pseudo-first order. The degradation amount was 82.53 % after 120 minutes of exposure to UV in the presence of 10 ppm hydrogen peroxide. Similarly, the experiment was performed with ozone with flow rate of 0.5 L/min instead of hydrogen peroxide and the reported degradation percentage is 56.09 %. The other oxidizing agent that has been used instead of H₂O₂ is potassium persulfate with a loading of 0.4 mg/L resulting in 99.59 % degradation of Acid Blue 80 dye after 120 minutes exposure to UV light [99].

1-12-Raman spectroscopy

Raman Spectroscopy, which is named after Indian physicist Sir Chandrasekhara Venkata Raman, who won the Nobel prize in 1930, is a spectroscopic tool for monitoring vibrational modes in the materials [100]. Because vibrational modes are specifically correlated to chemical bonds and symmetry of the molecule under study, it can be used as a fingerprint for that specific molecule. Thus, it is able to provide unique information in terms of chemical characterization [101-104].

The theory of Raman spectroscopy is on the basis of inelastic scattering of light as a result of energy transfer between photons and molecules. Illumination of monochromatic light leads to excitation of the molecule from the vibrational ground state to the virtual states. Through the relaxation process of the excited molecule to the ground state, two possible mechanisms are feasible. The first one, called Rayleigh scattering, is the relaxation to the ground state, elastically, by releasing a photon containing the same energy as the incident photon. In this case, no Raman signal can be detected. The second possible scenario is when the energy of the emitted photon during relaxation process is different from the absorbed photon because the molecule relaxes back to a different vibrational energy level. If the final energy state of the molecule is higher than its ground state, the emitted photon shifts to lower frequency which is called Stokes shift. Otherwise, if the initial state possesses a higher energy than the final energy state of the molecule, the released photons appears at higher frequency which is named anti-Stokes shift [105] (Figure (1-9)).

Raman spectroscopy and infrared (IR) spectroscopy are complementary in terms of selection rules. IR spectroscopy is applicable only for molecules with a dipole moment. However, Raman spectroscopy can be obtained for non-polar molecules such as N_2 and O_2 [105]. In general, for centrosymmetric molecules, an IR transition cannot be Raman active and vice versa, which is recognized as the mutual exclusivity principle [107].

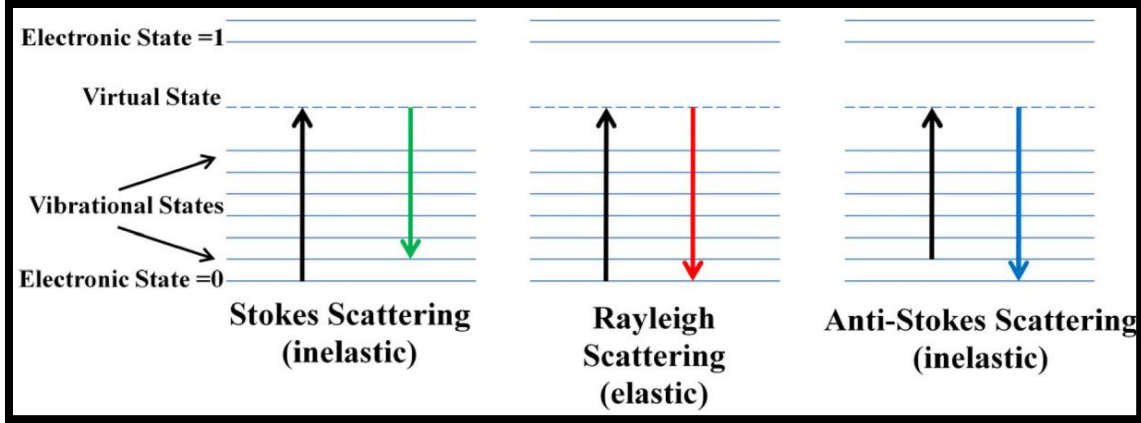


Figure (1-9). Schematic diagram of energy states in Raman spectroscopy. Republished from open-access reference [106], © 2015, Lupoi J. S.; Gjersing E.; Davis M. F.; *Front. Bioeng. Biotechnol.*, 2015, 3, 1., <https://www.frontiersin.org/articles/10.3389/fbioe.2015.00050/full>

For a molecule to be Raman active, only the polarizability of the molecule has to change during the vibration. The Raman scattering can be described as follows: The strength of the electric field of an electromagnetic wave fluctuates as a function of time:

$$\vec{E} = \vec{E}_0 \cdot \cos(2\pi\nu_0 t) \quad (20)$$

where ν_0 is the frequency of the electromagnetic wave (laser beam in case of Raman spectroscopy) and E_0 is the vibrational amplitude. Irradiation of a diatomic molecule with a laser beam results in induction of an electric dipole moment P :

$$\vec{P} = \alpha \cdot \vec{E} = \alpha \cdot \vec{E}_0 \cdot \cos(2\pi\nu_0 t) \quad (21)$$

Where α is a proportionality constant called polarizability. On the other hand, the relationship between the vibrational frequency (ν_m) of a molecule with its nuclear displacement is defined:

$$q = q_0 \cdot \cos(2\pi\nu_m t) \quad (22)$$

Where q is the vibrational amplitude. If the amplitude of vibration is small, there is a linear relationship between α and q :

$$\alpha = \alpha_0 + \left(\frac{\partial\alpha}{\partial Q}\right)_0 q + \dots \quad (23)$$

Where α_0 is the polarizability at the equilibrium position and is $\left(\frac{\partial\alpha}{\partial Q}\right)_0$ the representative of deviation rate of polarizability from its equilibrium point. The abovementioned formulas can be combined as follows:

$$\vec{P} = \alpha \cdot \vec{E}_0 \cdot \cos(2\pi\nu_0 t) \quad (24)$$

$$= \alpha_0 \cdot \vec{E}_0 \cdot \cos(2\pi\nu_0 t) + \left(\frac{\partial\alpha}{\partial Q}\right)_0 q E_0 \cos(2\pi\nu_0 t) \quad (25)$$

$$= \alpha_0 \cdot \vec{E}_0 \cdot \cos(2\pi\nu_0 t) + \left(\frac{\partial\alpha}{\partial Q}\right)_0 q_0 E_0 \cos(2\pi\nu_0 t) \cos(2\pi\nu_m t) \quad (26)$$

$$= \alpha_0 \cdot \vec{E}_0 \cdot \cos(2\pi\nu_0 t) + \frac{1}{2} \left(\frac{\partial\alpha}{\partial Q}\right)_0 q_0 E_0 [\cos\{2\pi(\nu_0 + \nu_m)t\} + \cos\{2\pi(\nu_0 - \nu_m)t\}] \quad (27)$$

Based on the classical theory, the first term corresponds to an oscillating dipole of the light with frequency ν_0 (Rayleigh scattering) and the second term is attributed to the Raman scattering frequency of $\nu_0 - \nu_m$ (Stokes) and $\nu_0 + \nu_m$ (Anti-Stokes). Consequently, if $\left(\frac{\partial\alpha}{\partial Q}\right)_0$ is zero, the vibration is not Raman-active.

The intensity of scattering is determined by the strength of polarization change. But, the Raman shift is a function of the vibrational energy levels involved. A stretching vibrational mode requires a greater amount of energy to happen than a bend. A laser is typically employed as a light source for Raman spectroscopy due to its high intensity, which is crucial for providing significant signal-to-noise (S/N) ratio as well as effective scattering [108].

Overall, Raman spectroscopy is an effective analytical technique for both organic and inorganic materials. Raman spectroscopy has the capability to express strong signals for metal-oxygen bonds which makes it a superior method for titanium dioxide analysis [108].

1-13-Application of Raman mapping for titanium dioxide characterization

Raman spectroscopy has been extensively used for TiO₂ characterization [109-113]. Identification of titanium dioxide in term of its solid polymorphs [109-111,113] and study of the

correlation between particle size and Raman patterns are examples of Raman spectroscopy application for evaluation of TiO₂ properties[112].

Moreover, Raman mapping is also employed as a visual analytical technique to shed light on the characteristics of titanium dioxide. Ajito *et al.* reported a black-and-white image of an anodically grown TiO₂ film showing the relative amount of anatase and rutile phases as demonstrated in Figure (1-10). The selected area is 2 mm × 2 mm. The signal for each of the phases is collected at a specific wavelength [114].

Investigation of the chemical morphology of P25, famous commercial titanium dioxide from Degussa[®], has been reported in 2009. It is well-known that P25 is roughly composed of 80% anatase and 20% rutile. The obtained confocal Raman image, which is recorded from a 10 μm × 10 μm area which is very small area compared to the study discussed above. The recorded images are depicted in Figure (1-11). It can be seen that, small amounts of rutile in the form of aggregate are dispersed in anatase. Cross section analysis shows that by increasing one of the two phases, the other one is decreased [115]. Knoks *et al.* have tried to synthesize titanium dioxide through anodization process with two different electrolytes. The impact of electrolyte on anatase/rutile phase distribution is investigated by Raman imaging. The obtained images for those samples possessing both phases are similar to P25. Rutile phase is distributed like islands in between the anatase phase [116].

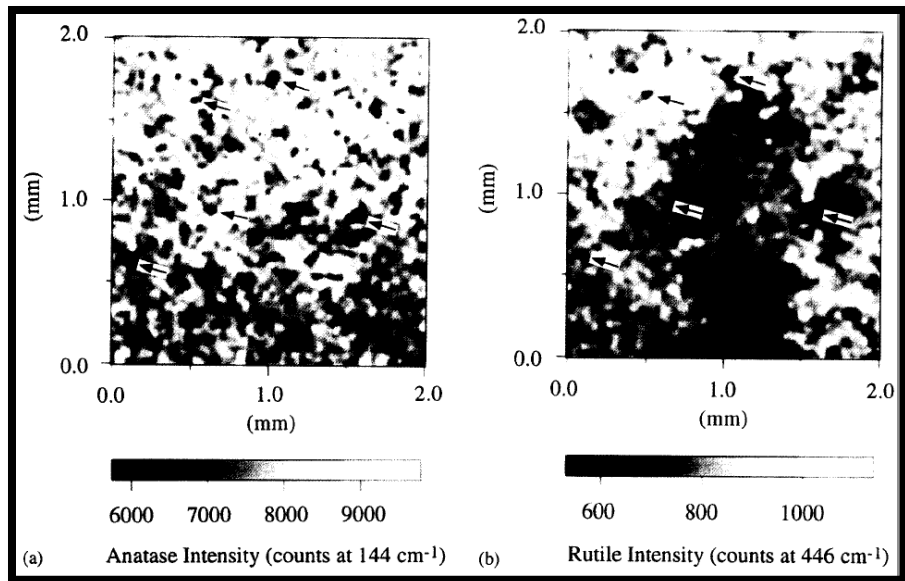


Figure (1-10). Black-and-white Raman images recorded from anodically grown TiO_2 film representing two different polymorphs of TiO_2 . Reprinted from reference [114], Copyright © 1995, With permission from Elsevier.

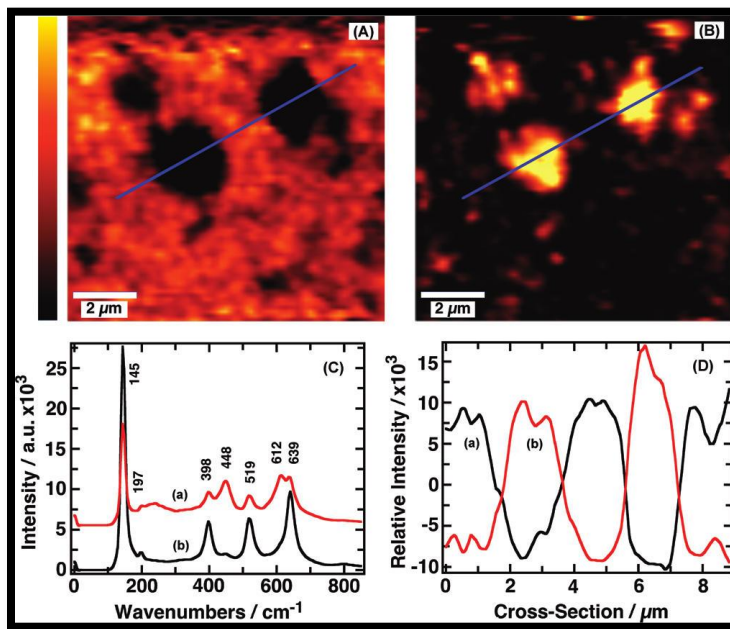


Figure (1-11). Confocal Raman mapping of anatase/rutile distribution on P25 film fired at 450°C . Anatase and rutile are color-coded with black and red, respectively. In image (C) the same color code are applied to exert anatase-rich and rutile-rich spectra. Raman scattering intensity at 398 and 448 cm^{-1} bands across the cross section lines in (A) and (B) are depicted in (D). Reprinted with permission from reference [115], Copyright © 2009, American Chemical Society.

Kment *et al.* reported the Raman imaging of synthesized titanium dioxide based on the dip coating method. The obtained TiO_2 is composed of anatase and brookite phases that are mapped by means of Raman spectroscopy (Figure (1-12)). The distribution of phases in the ring-like film is not homogeneous. The inside of the ring is mainly anatase while brookite can be found both in the center as well as surroundings of the ring-like structure. These ring-like structures are formed during the crystallization process on the surface of titanium dioxide films [117].

Other phases of titanium dioxide are also studied by Raman mapping. The $\alpha\text{-PbO}_2$ structured polymorph of titanium dioxide, which is also called $\text{TiO}_2\text{-II}$, is identified by Raman imaging in samples composed of three different phases of TiO_2 (rutile, anatase and $\text{TiO}_2\text{-II}$). In addition to TiO_2 , other materials such as SiO_2 in the form of quartz and substrate-adhesive epoxy exist in the samples [118].

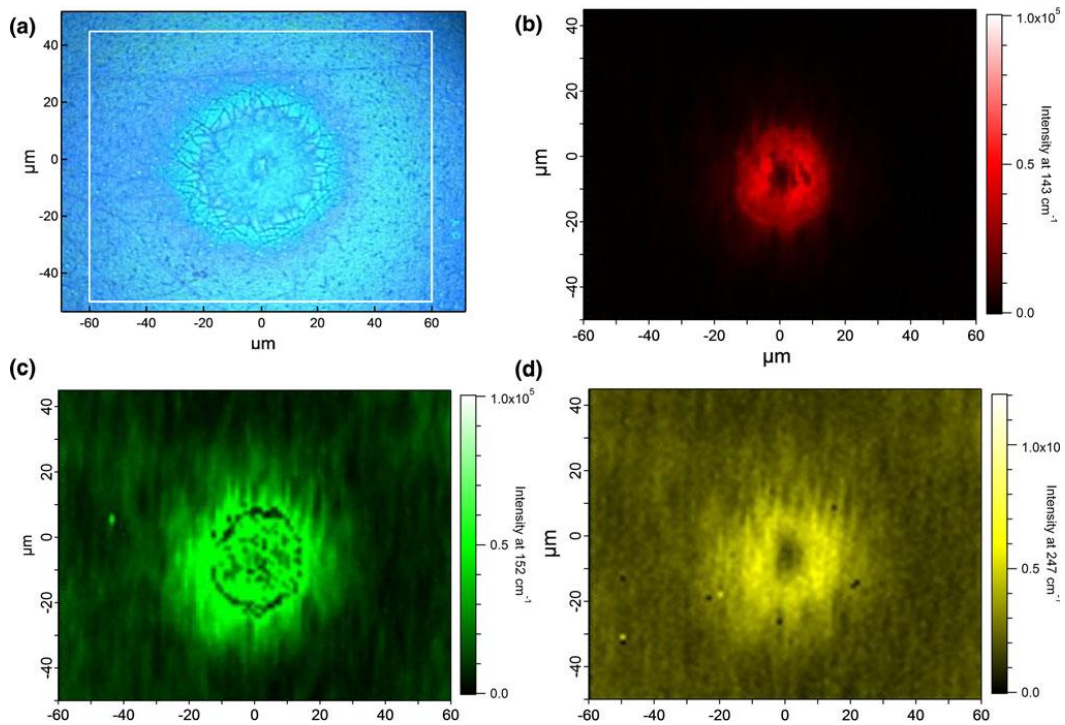


Figure (1-12). Confocal Raman mapping of anatase/brookite distribution on the prepared film: (a) Optical microscope image of the mapped area (b) Raman image of anatase taken at 143 cm^{-1} (c) Raman image of brookite taken at 152 cm^{-1} (d) Raman image of brookite taken at 247 cm^{-1} [117]. Reprinted by permission from Springer Nature: reference [117], Copyright © 2012.

Raman mapping has also been applied to distinguish between titanium dioxide and other materials. Zavalin *et al.* also picked Ti-O and P-O Raman vibrations in order to obtain the distribution abundance image of TiO₂ versus phosphate in porous glass ceramics [119]. Identification of the texture of carbon nanotubes in TiO₂ nanofibers as one of the examples of hybrid materials is expressed via Raman imaging. As depicted in Figure (1-13), both phases coexist and they are mixed homogenously [120].

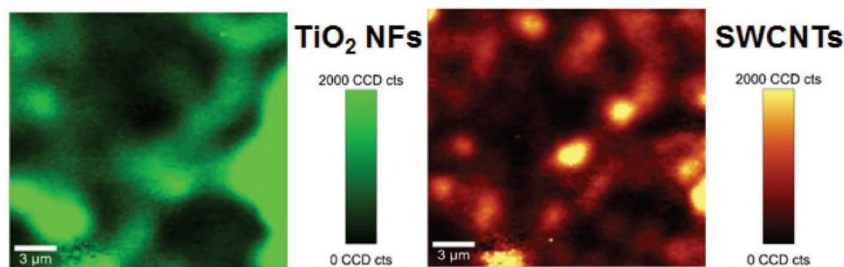


Figure (1-13). Raman images of TiO₂ nanofibers (left side) and carbon nanotubes (right side). Republished from open access reference [120], © 2017 The Authors. Published by WILEY-VCH Verlag GmbH & Co. KGaA, Weinheim, <https://onlinelibrary.wiley.com/doi/10.1002/advs.201600504>.

Among various doped titanium dioxides, carbon-doped TiO₂ has been the center of attention recently. Treschev *et al.* have revealed the correlation between the annealing temperature and phase distribution pattern in carbon-doped TiO₂ with different concentrations of carbon. The Raman images from titanium dioxide with lowest calcination temperature (150 °C) are shown in Figure (1-14). The rutile structure is not likely to exist here since this polymorph usually forms at annealing temperatures higher than 600 °C. Because rutile is detected vicinal to amorphous carbon, it is hypothesized that carbon assists formation of rutile by lowering the phase transformation temperature. However, by increasing the calcination temperature, more rutile has been observed in Raman images [121].

Afterwards, the mechanism behind the phase conversion from anatase to rutile by carbon at lower temperatures has been explained by Chatterjee *et al.* The phase transformation from anatase to rutile has occurred by applying high-power Raman laser for imaging on carbon containing titanium dioxide. Upon annealing by Raman laser, carbon could react with the oxygen

of titanium dioxide creating oxygen vacancies which is in favor of transformation from anatase to rutile [122]. On the contrary, the outcomes of Raman imaging on carbon-doped nanotubes of titanium dioxide have proved that introducing carbon to TiO₂ nanotubes suppresses the formation of rutile [123].

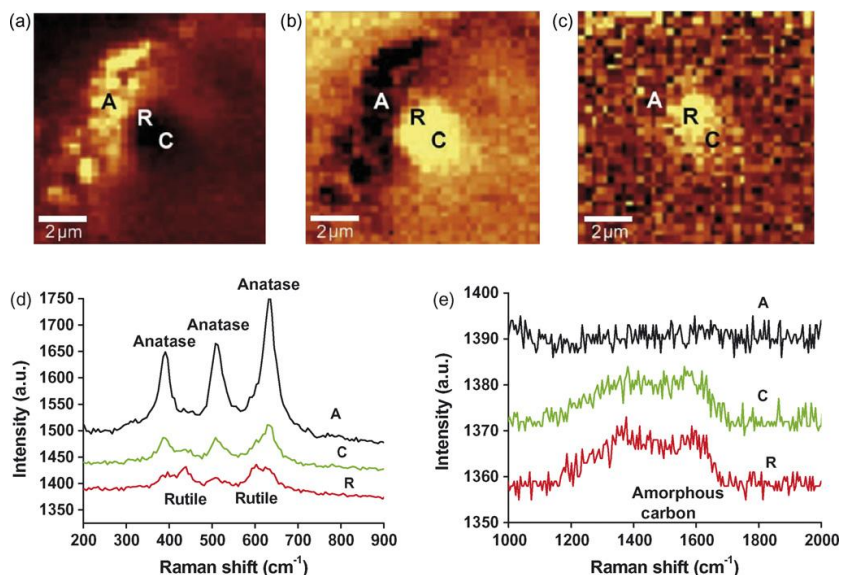


Figure (1-14). The Raman images for (a) anatase (b) rutile (c) amorphous carbon (The brighter color in each image means higher content of that phase). (d) and (e) are Raman spectra taken from different tagged points on the sample. Reprinted from reference [121], Copyright © 2008, With permission from Elsevier.

Raman imaging of titanium dioxide is also employed in biological systems. After some concerns regarding the potential toxicity of nanoparticles were raised, Salehi *et al.* have monitored the intercellular penetration of TiO₂ nanoparticles in living MCF-7 and TERT cells employing Raman mapping as an effective tool. This method is known as one of the label-free imaging techniques in biology. It has been proved that the presence of TiO₂ particles within a cell does not induce apoptosis [124]. Harvanová *et al.* have investigated the cellular uptake of TiO₂ nanoparticles and their distribution in cell environment by means of Raman imaging for toxicological studies. The Raman mapping of TiO₂ nanoparticles in human fibroblasts BJ cell is depicted in Figure (1-15) which confirms the penetration of titanium dioxide nanoparticles when

the cells are exposed to nanoparticles [125]. This phenomenon could possibly impact the cellular metabolism [126-127].

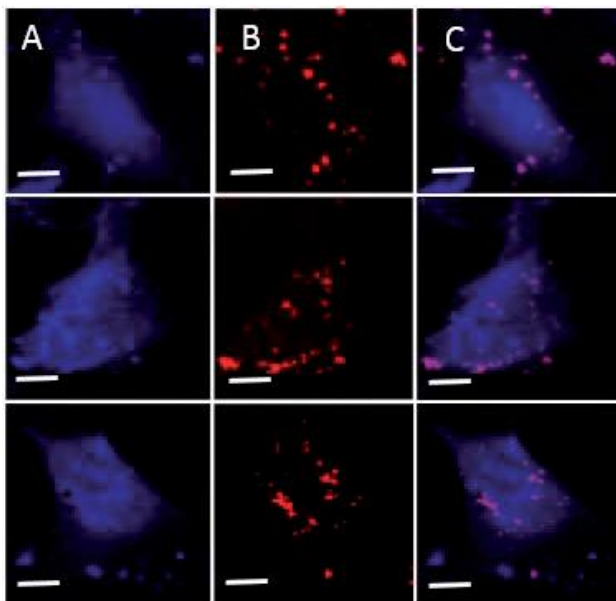


Figure (1-15). Raman images of (a) BJ cells (b) TiO₂ nanoparticles (c) distribution of TiO₂ nanoparticles in BJ cells. Republished from open access reference [125], Harvanová M.; Mašek V.; Jírová D.; Kolářová H.; *Lékař a technika*, 2016, 46(1), 25, <https://ojs.cvut.cz/ojs/index.php/CTJ/article/view/4204/4058>.

1-14-Raman imaging of dye-adsorbed TiO₂ films

To the best of our knowledge, the only available Raman mapping of an adsorbed dye over the surface of titanium dioxide was reported by Lee *et al.* from McGill University in 2010 [128]. The distribution of N719 dye (((bis(tetrabutylammonium)[cis-di(thiocyanato)-bis(2,20-bipyridyl-4-carboxylate-40-carboxylic acid)-ruthenium(II)])) on the surface of titanium dioxide was examined with confocal Raman imaging by choosing anatase band at ca. 640 cm⁻¹ and different bands attributed to different functional groups of the dye as indicators for TiO₂ and the dye, respectively. As it can be observed in Figure (1-16-a), the brighter color means the existence of more bare TiO₂ rather than the covered one with the dye in that area. Previous works showed that the COO⁻_{sym} Raman band can be used as a confirmation of N719 chemisorption [129-130]. Thus, Raman mapping of this peak can indicate where chemisorption exist (Figure 1-16-b). The overall

distribution of N719 dye, regardless of chemisorption or physisorption, can be seen in Figure (1-16-c) by tracking the bipyridine ring-stretching mode. Except few small areas, the whole TiO_2 surface is well covered with N719. The last image (Figure 1-16-d) shows the distribution of free carbonyl groups corresponded to one or more unbound carbonyl group of N719 molecules on the titanium dioxide film [128].

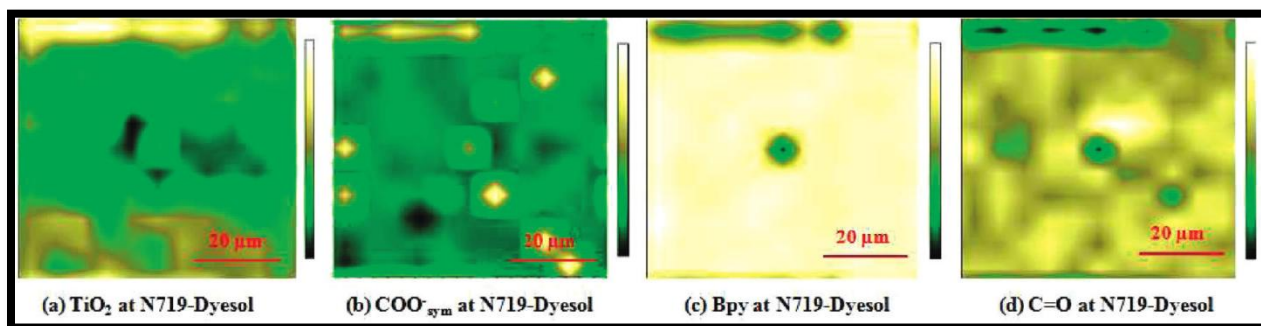


Figure (1-16). Confocal Raman imaging of N719 dye adsorbed on the commercial TiO_2 surface. Reprinted with permission from reference [128], Copyright © 2010, American Chemical Society.

1-15-Thesis objectives

The core objective of this project was to study the effect of iron as dopant in pure titanium dioxide nanomaterials in terms of their structure and photodegradation properties. This work was carried out in three main steps.

In the first step, iron-doped titanium dioxide with various percentages of iron was synthesized by the sol-gel method. In order to compare the effects of the addition of the dopant on the material's structure and properties, materials containing various amounts of iron (from 0.5 to 5.0 mol% iron) as well as pure TiO_2 samples were synthesized.

The second step involved the detailed characterization of the materials synthesized in step one. All samples (including pure TiO_2) were characterized using several analytical methods including Powder XRD (X-Ray Diffraction), EDX (Energy Dispersive X-ray), SEM (Scanning Electron

Microscope), UV-Vis DRS (Diffusive Reflectance Spectroscopy), DSC (Differential Scanning Calorimetry) and Raman spectroscopy imaging.

Finally, in the third step, the photodegradation properties of pure and iron-doped titanium dioxide samples were investigated via photodegradation of methylene blue as a model dye. Among all parameters which are significant for any typical photocatalytic studies, the effect of pH and change in surface charges as a result of pH alteration were carefully studied.

1-16-References

- [1] Pfaff G.; Reynders P.; *Chem. Rev.*, **1999**, 99, 1963.
- [2] Salvador A.; Pascual-Marti M. C.; Adell J. R.; Requeni A.; March J. G.; *J. Pharm. Biomed. Anal.*, **2000**, 22, 301.
- [3] Zallen R.; Moret M. P.; *Solid State Commun.*, **2006**, 137, 154.
- [4] Braun J. H.; Baidins A.; Marganski R. E.; *Prog. Org. Coat.*, **1992**, 20, 105.
- [5] Yuan S. A.; Chen W. H.; Hu S. S.; *Mater. Sci. Eng. C*, **2005**, 25, 479.
- [6] Fujishima A.; Honda K.; *Nature*, **1972**, 37, 238.
- [7] Fujishima A.; Rao T. N.; Tryk D. A.; *J. Photochem. Photobiol. C*, **2000**, 1, 1.
- [8] Tryk D. A.; Fujishima A.; Honda K.; *Electrochim. Acta*, **2000**, 45, 2363.
- [9] Graetzel M.; *Nature*, **2001**, 414, 338.
- [10] Hagfeldt A.; Graetzel M.; *Chem. Rev.*, **1995**, 95, 49.
- [11] Linsebigler A. L.; Lu G.; Yates J. T.; *J. Chem. Rev.*, **1995**, 95, 735.
- [12] Millis A.; Le Hunte S.; *J. Photochem. Photobiol. A*, **1997**, 108, 1.
- [13] Hoffmann M. R.; Martin S. T.; Choi W.; Bahnemann D. W.; *Chem. Rev.*, **1995**, 95, 69.
- [14] Graetzel M.; *J. Photochem. Photobiol. A*, **2004**, 164, 3.
- [15] Graetzel M.; *MRS Bull.*, **2005**, 30, 23.
- [16] Hashimoto K.; Irie H.; Fujishima A.; *Jpn. J. Appl. Phys.*, **2005**, 44(12), 8269.
- [17] Chen X.; Mao S. S.; *Chem. Rev.*, **2007**, 107, 2891.
- [18] Zhang H.; Banfield J. F.; *Chem. Rev.*, **2014**, 114, 9613.
- [19] Zhang J.; Zhou P.; Liu J.; Yu J.; *Phys. Chem. Chem. Phys.*, **2014**, 16, 20382.
- [20] Dambournet D.; Belharouak I.; Amine K.; *Chem. Mater.*, **2010**, 22, 1173.
- [21] Zaleska A.; *Recent Patents on Engineering*, **2008**, 2, 157.
- [22] Umebayashi T.; Yamaki T.; Itoh H.; Asai K.; *J. Phys. Chem. Solids*, **2002**, 63, 1909.
- [23] Park J. H.; Kim S.; Bard A.; *J. Nano Lett.*, **2006**, 6, 24.
- [24] Mor G. K.; Varghese O. K.; Paulose M.; Shankar K.; Grimes C. A.; *Solar Energ. Mater. Solar Cell*, **2006**, 90, 2011.
- [25] Pierre A. C.; Pajonk G. M.; *Chem. Rev.*, **2002**, 102, 4243.

- [26] Lu Z. L.; Lindner E.; Mayer H. A.; *Chem. Rev.*, **2002**, 102, 3543.
- [27] Bessekhoud Y.; Robert D.; Weber J. V.; *J. Photochem. Photobiol. A*, **2003**, 157, 47.
- [28] Oskam G.; Nellore A.; Penn R. L.; Searson P. C.; *J. Phys. Chem. B*, **2003**, 107, 1734.
- [29] Sugimoto, T.; *Adv. Colloid Interface Sci.*, **1987**, 28, 65.
- [31] Lei J.; Li X.; Li W.; Sun F.; Lu D.; Yi J.; *Int. J. Hydrogen Energ.*, **2011**, 36, 8167.
- [32] Fujishima A.; Honda K.; *Nature*, **1972**, 238, 37.
- [33] Dal'Acqua N.; Scheffer F. R.; Boniatti R.; da Silva B. V. M.; de Melo J. V.; da Silva Crespo J.; Giovanela M.; Pereira M. B.; Weibel D. E.; Machado G.; *J. Phys. Chem. C*, **2013**, 117(44), 23235.
- [34] Guo S.; Han S.; Mao H.; Dong S.; Wu C.; Jia L.; Chi B.; Pu J.; Li J.; *J. Power Sources*, **2014**, 245, 979.
- [35] Rayalu S. S.; Jose D.; Joshi M. V.; Mangrulkar P. A.; Shrestha K.; Klabunde K.; *Appl. Catal. B*, **2013**, 142, 684.
- [36] Sopyan I.; Watanabe M.; Murasawa S.; Hashimoto K.; Fujishima A.; *J. Photochem. Photobiol. A*, **1996**, 98, 79.
- [37] Vorontsov A. V.; Besov A. S.; Parmon V. N.; *Appl. Catal. B*, **2013**, 129, 318.
- [38] Lv J.; Zhu L.; *Environ. Technol.*, **2013**, 34(11), 1447.
- [39] Su C.; Ran X.; Hu J.; Shao C.; *Environ. Sci. Technol.*, **2013**, 47(20), 11562.
- [40] Bai H.; Liu L.; Liu Z.; Sun D. D.; *Water. Res.*, **2013**, 47(12), 4126.
- [41] Liu L.; Bai H.; Liu J.; Sun D. D.; *J. Hazard. Mater.*, **2013**, 261(6), 214.
- [42] Wei X.; Cui H.; Guo S.; Zhao L.; Li W.; *J. Hazard. Mater.*, **2013**, 263, 650.
- [43] Chen C.; Wang C.; Yeh J.; *Text. Res. J.*, **2010**, 80(4), 291.
- [44] Hashimoto K.; Irie H.; Fujishima A.; *Jpn. J. Appl. Phys.*, **2005**, 44(12), 8269.
- [45] Renz C.; *Helv. Chim. Acta*, **1921**, 4, 961.

- [46] Doodeve C. F.; Kitchener J. A.; *Trans. Faraday Soc.*, **1938**, 34, 902.
- [47] Linsebigler A. L.; Lu G.; Yates J. T.; *Chem. Rev.*, **1995**, 95(3), 735.
- [48] (a) Schneider J.; Matsuoka M.; Takeuchi M.; Zhang J.; Horiuchi Y.; Anpo M.; Bahnemann D. W.; *Chem. Rev.*, **2014**, 114, 9919. (b) Bharti B.; Kumar S.; Lee H.; Kumar R.; *Sci. Rep.*, **2016**, 6, 32355. (c) Amano F.; Nakata M.; Yamamoto A.; Tanaka T.; *J. Phys. Chem. C*, **2016**, 120, 6467.
- [49] Chen X.; Shen S.; Guo L.; Mao S. S.; *Chem. Rev.*, **2010**, 110, 6503.
- [50] Swierk J. R.; Mallouk T. E.; *Chem. Soc. Rev.*, **2013**, 42, 2357.
- [51] Bolton J. R.; *Sol. Energy*, **1996**, 57(1), 37.
- [52] Frank S. N.; Bard A. J.; *J. Am. Chem. Soc.*, **1977**, 99(4), 303.
- [53] Frank S. N.; Bard A.; *J. Phys. Chem.*, **1977**, 81(15), 1484.
- [54] Chen H.; Nanayakkara C. E.; Grassian V. H.; *Chem. Rev.*, **2012**, 112, 5919.
- [55] Ajmal A.; Majeed I.; Malik R. N.; Idriss H.; Nadeem M. A.; *RSC Adv.*, **2014**, 4, 37003.
- [56] Fröschl T.; Hörmann U.; Kubiak P.; Kucerová G.; Pfanzelt M.; Weiss C. K.; Behm R. J.; Hüsing N.; Kaiser U.; Landfester K.; Wohlfahrt-Mehrens M.; *Chem. Soc. Rev.*, **2012**, 41, 5313.
- [57] Galindo C.; Jacques P.; Kalt A.; *J. Photochem. Photobiol. A*, **2000**, 130, 35.
- [58] Ma Y.; Yao J.; *J. Photochem. Photobiol. A*, **1998**, 116, 167.
- [59] Chen F.; Xie Y.; Zhao J.; Lu G.; *Chemosphere*, **2001**, 44, 1159.
- [60] Zhang F.; Zhao J.; Shen T.; Hidaka H.; Pelizzetti E.; Serpone N.; *Appl. Catal., B*, **1998**, 15, 147.
- [61] Zhu H.; Jiang R.; Fu Y.; Guan Y.; Yao J.; Xiao L.; Zeng G.; *Desalination*, **2012**, 286, 41.
- [62] Alaton I. A.; Balcioglu I. A.; Bahnemann D. W.; *Water Res.*, **2002**, 36, 1143.
- [63] Qamar M.; Saquib M.; Muneer M.; *Dyes Pigm.*, **2005**, 65,1.
- [64] Mendret J.; Hatat-Fraile M.; Rivallin M.; Brosillon S.; *Sep. Purif. Technol.*, **2013**, 118, 406.
- [65] Saien J.; Khezrianjoo S.; *J. Hazard. Mater.*, **2008**, 157, 269.

- [66] Mahvi A. H.; Ghanbarian M.; Nasserli S.; Khairi A., *Desalination*, **2009**, 239, 309.
- [67] Fox M. A.; Dulay M. T.; *Chem. Rev.*, **1993**, 93, 341.
- [69] Neppolian B.; Choi H.; Sakthivel S.; Arabindoo B.; Murugesan V.; *Chemosphere*, **2002**, 46, 1173.
- [70] Bizani E.; Fytianos K.; Poullos I.; Tsiridis V.; *J. Hazard. Mater.*, **2006**, 136, 85.
- [71] Kaneco S.; Katsumata H.; Suzuki T.; Ohta K.; *Chem. Eng. J.*, **2006**, 125, 59.
- [72] Malato S.; Fernandez-Ibanez P.; Maldonado M. I.; Blanco J.; Gernjak W.; *Catal. Today*, **2009**, 147, 1.
- [73] Ambrus Z.; Balázs N.; Alapi T.; Wittmann G.; Sipos P.; *Appl. Catal., B*, **2008**, 81, 27.
- [74] Jaimy K. B.; Baiju K. V.; Ghosh S.; Warriar K. G. K.; *J. Solid State Chem.*, **2012**, 186, 149.
- [75] Wang C.; Böttcher C.; Bahnemann D. W.; Dohrmann J. K.; *J. Mater. Chem.*, **2003**, 13, 2322.
- [76] Andriamiadamanana C.; Laberty-Robert C.; Sougrati M. T.; Casale S.; Davoisne C.; Patra S.; Sauvage F.; *Inorg. Chem.*, **2014**, 53, 10129.
- [77] Deng F.; Luo X.; Li K.; Tu X.; Luo S.; Yang L.; Zhou N.; Shu H.; *J. Mol. Catal. A: Chem.*, **2013**, 366, 222.
- [78] Crișan M.; Răileanu M.; Drăgan N.; Crișan D.; Ianculescu A.; Nițoi I.; Oancea P.; șomăcescu S.; Stănică N.; Vasile B.; Stan C.; *Appl. Catal., A*, **2015**, 504, 130.
- [79] Tabasideha S.; Malekib A.; Shahmoradib B.; Ghahremani E.; *Sep. Purif. Technol.*, **2017**, 189, 186.
- [80] Wei X.; Wang H.; Zhu G.; Chen J.; Zhu L.; *Ceram. Int.*, **2013**, 39, 4009.
- [81] Navío J. A.; Colon G.; Litter M. I.; Bianco G. N.; *J. Mol. Catal. A: Chem.*, **1996**, 106, 267.
- [82] Yen C.; Wang D.; Shih M.; Chang L.; Shih H. C.; *Appl. Surf. Sci.*, **2010**, 256, 6865.
- [83] Carneiro J. O.; Teixeira V.; Portinha A.; Magalhaes A.; Coutinho P.; Tavares C. J.; Newton R.; *Mater. Sci. Eng. B*, **2007**, 138, 144.
- [84] Crișan M.; Mardare D.; Ianculescu A.; Drăgan N.; Nițoi I.; Crișan D.; Voicescu M.; Todan L.; Oancea P.; Adomniței C.; Dobromir M.; Gabrovska M.; Vasile B.; *Appl. Surf. Sci.*, **2018**, 455, 201.
- [85] Nagaveni K.; Hegde M. S.; Madras G.; *J. Phys. Chem. B*, **2004**, 108, 20204.

- [86] Wang X. H.; Li J.-G.; Kamiyama H.; Moriyoshi Y.; Ishigaki T.; *J. Phys. Chem. B*, **2006**, 110, 6804.
- [87] Nahar M. S.; Hasegawa K.; Kagaya S.; *Chemosphere*, **2006**, 65, 1976.
- [88] Sun L.; Li J.; Wang C. L.; Li S. F.; Chen H. B.; Lin C. J.; *Sol. Energy Mater Sol. Cells*, **2009**, 93, 1875.
- [89] Fàbrega C.; Andreu T.; Cabot A.; Morante J. R.; *J. Photochem. Photobiol. A*, **2010**, 211, 170.
- [90] Ganesh I.; Kumar P. P.; Gupta A. K.; Sekhar P. S. C.; Radha K.; Padmanabham G.; Sundararajan G.; *Processing and Application of Ceramics*, **2012**, 6, 21.
- [91] Delekar S. D.; Yadav H. M.; Achary S. N.; Meena S. S.; Pawar S. H.; *Appl. Surf. Sci.*, **2012**, 263, 536.
- [92] Adán C.; Bahamonde A.; Fernández-García M.; Martínez-Arias A.; *Appl. Catal., B*, **2007**, 72, 11.
- [93] Castro C. A.; Centeno A.; Giraldo S. A.; *Mater. Chem. Phys*, **2011**, 129, 1176.
- [94] Dukes F. M.; Iuppa E.; Meyer B.; Shultz M. J.; *Langmuir*, **2012**, 28, 16933.
- [95] Manu S.; Khadar M. A.; *J. Mater. Chem. C*, **2015**, 3, 1846.
- [96] Craciun E.; Predoana L.; Atkinson I.; Jitaru I.; Anghel E. M.; Bratan V.; Gifu C.; Anastasescu C.; Rusu A.; Raditoiu V.; Vasile E.; Anastasescu M.; Balint I.; *J. Photochem. Photobiol. A*, **2018**, 356, 18.
- [97] Carbajo J.; Adán C.; Rey A.; Martínez-Arias A.; Bahamonde A.; *Appl. Catal. B*, **2011**, 102, 85.
- [98] Milis A.; Peral J.; Domènech X.; *J. Mol. Catal.*, **1994**, 87, 67.
- [99] Ambati R.; Gogate P. R.; *J. Water Process Eng.*, **2017**, 20, 217.
- [100] Raman, C. V.; Krishnan, K. S. *Nature*, **1928**, 121, 501.
- [101] Tian Z. Q.; Ren B.; *Annu. Rev. Phys. Chem.*, **2004**, 55, 197.
- [102] Kiefer W.; *J. Raman Spectrosc.*, **2007**, 38, 1538.
- [103] Dresselhaus M. S.; Jorio A.; Saito R.; *Annu. Rev. Condens. Matt. Phys.*, **2010**, 1, 89.

- [104] Thomas G. J.; *Annu. Rev. Bioph. Biom.* **1999**, 28, 1.
- [105] Zhang S.; *Raman Spectroscopy and its Applications in Nanostructures*, First ed., John Wiley & Sons Ltd., **2012**.
- [106] Lupoi J. S.; Gjersing E.; Davis M. F.; *Front. Bioeng. Biotechnol.*, **2015**, 3, 1.
- [107] Huheey J. H.; Keither E. A.; Keiter R. L.; *Symmetry and group theory*, In: Piro J. New York (USA): Prentice Hall, **1997**.
- [108] Skoog D. A.; Holler F. J.; Crouch S. R.; *Principles of Instrumental Analysis*, Sixth edition., California (USA), **2006**.
- [109] Sang L.; Zhao Y.; Burda C.; *Chem. Rev.*, **2014**, 114, 9283.
- [110] Chen X.; Mao S. S.; *Chem. Rev.*, **2007**, 107, 2891.
- [111] Mazza T.; Barborini E.; Piseri P.; Milani P.; *Phys. Rev. B*, **2007**, 75, 045416.
- [112] Gupta S. K.; Desai R.; Jha P. K.; Sahoo S.; Kirin D.; *J. Raman Spectrosc.*, **2010**, 41, 350.
- [113] Su W.; Zhang J.; Feng Z.; Chen T.; Ying P.; Li C.; *J. Phys. Chem. C*, **2008**, 112, 7710.
- [114] Ajito K.; Sukamto J. P. H.; Nagahara L.A.; Hashimoto K.; Fujishima A.; *J. Electroanal. Chem.*, **1995**, 386, 229.
- [115] André L. A. P.; Bonacin J. A.; Toma S. H.; Araki K.; Toma H. E.; *Langmuir*, **2009**, 25(19), 11269.
- [116] Knoks A.; Kleperis J.; Grinberga L.; *Proc. Estonian. Acad. Sci.*, **2017**, 66, 4, 422.
- [117] Kment Š.; Gregora I.; Kmentová H.; Novotná P.; Hubička Z.; Krýsa J.; Sajdl P.; Dejneka A.; Brunclíková M.; Jastrabík L.; Hrabovsky M.; *J. Sol-Gel. Sci. Technol.*, **2012**, 63, 294.
- [118] Smith J. P.; Smith F. C.; Ottaway J.; Krull-Davatzes A. E.; Simonson B. M.; Glass B. P.; Booksh K. S.; *Appl. Spectrosc.*, **2017**, 71(8), 1816.
- [119] Zavalin A.; Cricenti A.; Generosi R.; Luce M.; Morgan S.; Piston D.; *Appl. Phys. Lett.*, **2006**, 88, 133126.
- [120] Batmunkh M.; Macdonald T. J.; Shearer C. J.; Bat-Erdene M.; Wang Y.; Biggs M. J.; Parkin I. P.; Nann T.; Shapter J. G.; *Adv. Sci.*; **2017**, 4, 1600504.

- [121] Treschev S. Y.; Chou P.; Tseng Y.; Wang J.; Perevedentseva E. V.; Cheng C.; *Appl. Catal., B*, **2008**, 79, 8.
- [122] Chatterjee A.; Wu S. -B.; Chou P. -W.; Wong M. S.; Cheng C. -L.; *J. Raman Spectrosc.*, **2011**, 42, 1075.
- [123] Taziwa R.; Meyer E.; Takata N.; *J. Nanosci. Nanotechnol. Res.*, **2017**, 1, No. 1:4.
- [124] Salehi H.; Calas-Bennasar I.; Durand J.; Middendorp E.; Valcarcel J.; Larroque C.; Nagy K.; Turzó K. K.; Dekany I.; Cuisinier F. J. G.; *J. Raman Spectrosc.*, **2014**, 45, 807.
- [125] Harvanová M.; Mašek V.; Jírová D.; Kolářová H.; *Lékař a technika*, **2016**, 46(1), 25.
- [126] Iannarelli L.; Giovannozzi A. M.; Morelli F.; Viscotti F.; Bigini P.; Maurino V.; Spoto G.; Martra G.; Ortel E.; Hodoroaba V.; Rossi A. M; Diomede L.; *RSC Adv.*, **2016**, 6, 70501.
- [127] Bettini S.; Boutet-Robinet E.; Cartier C.; Coméra C.; Gaultier E.; Dupuy J.; Naud N.; Taché S.; Grysan P.; Reguer S.; Thieriet N.; Réfrégiers M.; Thiaudière D.; Cravedi J.; *Sci. Rep.* 7, 40373.
- [128] Lee K. E.; Gomez M. A.; Elouatik S.; Demopoulos G. P.; *Langmuir*, **2010**, 26(12), 9575.
- [129] Leon C. P.; Kador L.; Peng B.; Thelakkat M.; *J. Phys. Chem. B*, **2006**, 110, 8723.
- [130] Shoute L. C. T.; Loppnow G. R.; *J. Am. Chem. Soc.*, **2003**, 125, 15636.

Chapter 2: Synthesis and Characterization of Iron-doped Titanium Dioxide Nanomaterials

2-1-Introduction

In this chapter, the details of the synthesis method of pure and iron-doped nanomaterials and the synthesis of iron (III) oxide will be covered. Thereafter, various characterization methods employed in this work, such as powder X-ray diffraction (XRD), diffusive reflectance UV-Vis spectroscopy (DRS UV-Vis), scanning electron microscope (SEM), Energy-dispersive X-ray (EDX), Cyclic voltammetry (CV) and differential scanning calorimetry (DSC), will be described in detail.

2-2-Synthesis

2-2-1-Synthesis of pure and iron-doped titanium dioxide nanomaterials

2-2-1-1-Background: Among different synthetic methods for the preparation of TiO₂ materials, the sol-gel method has been selected, as it is the most efficient, simple and common way for synthesizing doped titanium dioxide nanomaterials.

In terms of sol-gel process, TiO₂ materials were manufactured usually via an acid-catalyzed hydrolysis reaction of titanium (IV) alkoxide followed by condensation [1-3]. The conditions of the reaction affect the growth of Ti-O-Ti chains. When there is a low concentration of water in the reaction media, low hydrolysis rate and excess amount of titanium alkoxide lead to development of Ti-O-Ti chains. As hydrolysis rate and water percentage are elevated in the reaction mixture, the formation of Ti(OH)₄ is favored [1-3].

2-2-1-2-Experimental: The following chemicals were used: Iron (III) nitrate nonahydrate (Fe(NO₃)₃·9H₂O; ACS Reagent, ≥98%, Sigma-Aldrich), Titanium (IV) isopropoxide (Reagent grade, 97%, Aldrich), Ethanol (Commercial Alcohols Inc., USP).

All glassware was kept at least one night in concentrated sulfuric acid. Then, it was rinsed carefully with tap water and subsequently with deionized water. Pure TiO₂ and iron-doped TiO₂

were synthesized in the same conditions in order to compare them during characterization. All applied steps were completely identical for both materials, except the addition of iron (III) nitrate nonahydrate to one of the reactions.

First, a round-bottom flask was filled with 69 ml of anhydrous ethanol and 69 ml of deionized water (Millipore, Milli-Q gradient 10) in order to make 1:1 ethanol solution in water. The appropriate amount of iron (III) nitrate nonahydrate (table 2-1) was added to the one used for preparation of iron-doped TiO₂. Then, 12.40 ml of titanium (IV) isopropoxide was added to 56 ml of anhydrous ethanol and then transferred to a dropping funnel. Afterwards, titanium (IV) isopropoxide solution was added drop-wise to the reaction mixture. After gel formation completion, the product was suction-filtered and rinsed several times with ethanol while filtering. Subsequently, the filtered material was placed over night in the oven at 110 °C to dry. Then, the dried material was grounded by pestle and mortar. The obtained fine powders of TiO₂ or iron-doped TiO₂ were calcined in an electrical furnace at 450 °C for two hours. The color of the samples has changed gradually from white to brownish by increasing the amount of iron from 0 to 5 mol.%. All samples were in the form of fine powder stored in clean vials into a big desiccator.

Table (2-1). The amount of Fe(NO₃)₃.9H₂O used to prepare iron-doped TiO₂ samples.

Theoretical percentage of the iron (mol%)	0.5	0.7	1.7	2.1	3.0	4.0	5.0
Amount of iron (III) nitrate nonahydrate (g)	0.0832	0.1165	0.2827	0.3492	0.4988	0.6651	0.8314

2-2-2-Synthesis of iron (III) oxide

2-2-2-1-Background: Iron (III) oxide nanoparticles have been synthesized in order to investigate the origin of the solid state UV-Vis spectra of iron-doped TiO₂ samples. The UV-Vis spectrum was collected from each iron-doped sample and compared with samples prepared simply by mixing the titanium dioxide nanoparticles with a known amount of iron (III) oxide nanoparticles.

2-2-2-2-Experimental: Fe₂O₃ is prepared based on the sol-gel method [4-5]. 200 ml of 0.1 M solution of iron (III) nitrate nonahydrate is added drop wise to 800 ml of roughly 0.2 M

monohydrated citric acid as a ligand with vigorous stirring. The resulting solution is heated to 70-90 °C until most of the water is evaporated leading to the formation of a gel. Then, the gel is dried in the oven overnight at 70 °C. The formed solid is ground and calcined in the electrical furnace at 450 °C. The obtained product is ground, carefully, and a fine brown powder of iron (III) oxide is collected. The final product is in the form of fine powder with a dark brown powder, which is stored in a clean vial into a big desiccator.

2-3-Characterization of the synthesized nanomaterials

2-3-1-Methodology

2-3-1-1-Powder XRD diffraction

2-3-1-1-1-Background: X-ray diffraction (XRD) is a technique employed to study the crystal structure of materials. This characterization tool provide information about the degree of crystallinity of a system, the percentage of each phase of each compound and average grain size of crystals. The International Center for Diffraction Data keeps the diffraction pattern data for all known substances in a huge database. The outcome of each XRD run is compared with information in the database to determine the constituents of the tested material [6].

In a typical XRD apparatus, a X-ray beam is projected onto sample from 0° to 180°. If atoms are assembled in ordered planes with identical distances as they are in a specific crystal structure, they diffract the x-Ray beam at certain angles. The aforementioned angles are determined by Bragg's law [7]:

$$n.\lambda=2d.\sin \theta \quad (1)$$

Where d is the distance between the identical planes, n is an integer attributed to the number of planes utilized for analysis of Bragg's law, λ is the wavelength of incident X-ray beam and θ is the Bragg's angle.

The well-known Scherrer equation is used to calculate the average grain size in XRD technique:

$$D = \frac{K.\lambda}{\beta.\cos \theta} \quad (2)$$

Where K is a shape factor with a typical value of 0.9 (close to unity), λ is the wavelength of the X-ray radiation, θ is the Bragg angle for the selected peak and β is the line width at half-maximum height of the peak.

2-3-1-1-2-Experimental: The XRD powder patterns are collected by a Philips X-ray Diffraction system (model number: PW3710) using Cu K_{α} radiation source at the Department of Geology at University of Toronto.

2-3-1-2-Diffusive Reflectance UV-Vis spectroscopy (UV-Vis DRS)

2-3-1-2-1-Background: UV-Vis DRS is the most common method to evaluate the band gap and optical properties of semiconductor materials. It is reproducible, non-destructive and relatively fast. Doping of titanium dioxide can change its optical properties such as increasing the absorption in the visible region.

2-3-1-2-2-Experimental: All experiments have been carried out on prepared materials in the form of pellets. We used a PerkinElmer Lambda 950 UV-vis-NIR spectrophotometer equipped with a 150 mm integrating sphere from Professor Jennifer Chen's lab at Department of Chemistry at York University.

2-3-1-3-Scanning electron microscopy (SEM)

2-3-1-3-1-Background: Scanning electron microscopy (SEM) is a powerful imaging technique that uses focused electron beams instead of typical light source to generate high-resolution images.

In this technique, a generated electron beam is directed towards a sample holder. The energy of the incident electron beam can be adjusted as low as 100 eV or above 30 keV, based on the nature of the understudied sample. Typically, secondary electrons, which are produced by the excited atoms illuminated by the incident electron beam, are detected and subsequently analyzed to generate an image. The obtained high-resolution image shows the surface topography of the sample [8].

2-3-1-3-2-Experimental: The SEM images are taken by FEI Quanta three-dimensional (3D) dual-beam Field Emission-Focused Ion Beam (FEG-FIB) scanning electron microscope with an Everhart-Thornley detector working under high vacuum. The acceleration voltage is 20 kV for pure and iron-doped titanium dioxides and 25 kV for iron (III) oxide.

In order to prepare the materials for SEM experiments, each sample is deposited in the form of a fine powder on a piece of carbon tape following by coating a thin layer of gold on them. The gold is deposited by Desk V Sample Preparation (DENTON VACCUM) equipped for both evaporation and sputtering.

2-3-1-4-Energy Dispersive X-ray (EDX) analysis

2-3-1-4-1-Background: EDX is an analytical tool applied for elemental analysis using electron beam. Commonly, EDX is part of SEM instrument and can be used whenever it is required. The illuminated electron beam on the sample specimen can excite the inner-shell electrons of different types of atoms leading to removal of electron from this shell. To fill the vacancy in the inner-shell energy level, one outer-shell electron can relax into the vacant orbital by releasing a high-energy X-ray photon, which is specific for each element. The abundance of each element in the sample can be estimated from each characteristic X-ray attributed to each specific element.

2-3-1-4-2-Experimental: EDX analysis is performed employing the same equipment used to record the SEM images equipped with EDAX X-ray detector.

2-3-1-5-Differential Scanning Calorimetry (DSC)

2-3-1-5-1-Background: Differential scanning calorimetry is one of the analytical thermal techniques, which determines the energy input difference between the sample and a reference material as a function of temperature. Both the analyte and the reference material are studied carefully with temperature-controlled program. The recorded heat flow is deduced from the temperature difference between the sample and the reference [9].

2-3-1-5-2-Experimental: Differential scanning calorimetry (DSC) has been conducted by TA Instrument, DSC Q20. The scan rate was 2.00 °C/min.

2-3-1-6-Cyclic Voltammetry (CV)

2-3-1-6-1-Background: We used CV as a tool to study the electroactivity of our samples. CV has been used in the past to observe changes in i-V response with time while changing the environment such as pH change or UV illumination [10-12].

2-3-1-6-2-Experimental: The electrochemical properties of the pure and iron-doped titanium dioxide samples are measured by performing cyclic voltammetry experiments in a home-made three-electrode cell arrangement with the voltammetric analyzer PGZ 402 VoltaLab from Radiometer Copenhagen. The working electrode is titanium dioxide thin film deposited on conductive FTO glass, which is mounted in the cell by pressing it against the opening located on the bottom of the cell employing an o-ring seal with an approximate surface area of 1 cm². The applied counter electrode and reference electrodes are a large surface-area platinum coil and standard calomel electrode (SCE), respectively. 0.1 M potassium perchlorate in a mixture of acetonitrile (ACN) and DMF is used as electrolyte. Using the mixture of ACN and DMF allows us to assign redox processes related to TiO₂. Before starting measurements, all cell parts as well as electrolyte are purged with a stream of high-purity argon gas. The potential is scanned at first anodically from 0 to +500 mV in 3 consecutive cycles. Consequently, the experiment is repeated in the same condition and on the same sample with a larger scan window of 0 to +1000 mV, +1500 mV and +2000 mV (3 cycles for each one). Afterwards, the potential is reversed from +2000 mV to -250 mV and decreased gradually in -250 mV increments to -2000 mV. The scan rate for all implemented tests is 50 mV/s.

2-3-2-Results and Discussion

2-3-2-1-Powder XRD diffraction

2-3-2-1-1-Powder XRD diffractions of pure and iron-doped titanium dioxide nanomaterials: The powder XRD spectra of iron-doped titanium dioxide samples are presented in the Figure (2-1). All samples are composed predominantly of titanium dioxide in the anatase phase. Only three of them contain some amounts of the brookite phase. Rutile phase is not present in any of the prepared materials. For comparison purposes, the XRD pattern of pure anatase, pure brookite and pure rutile is provided in appendix 1.

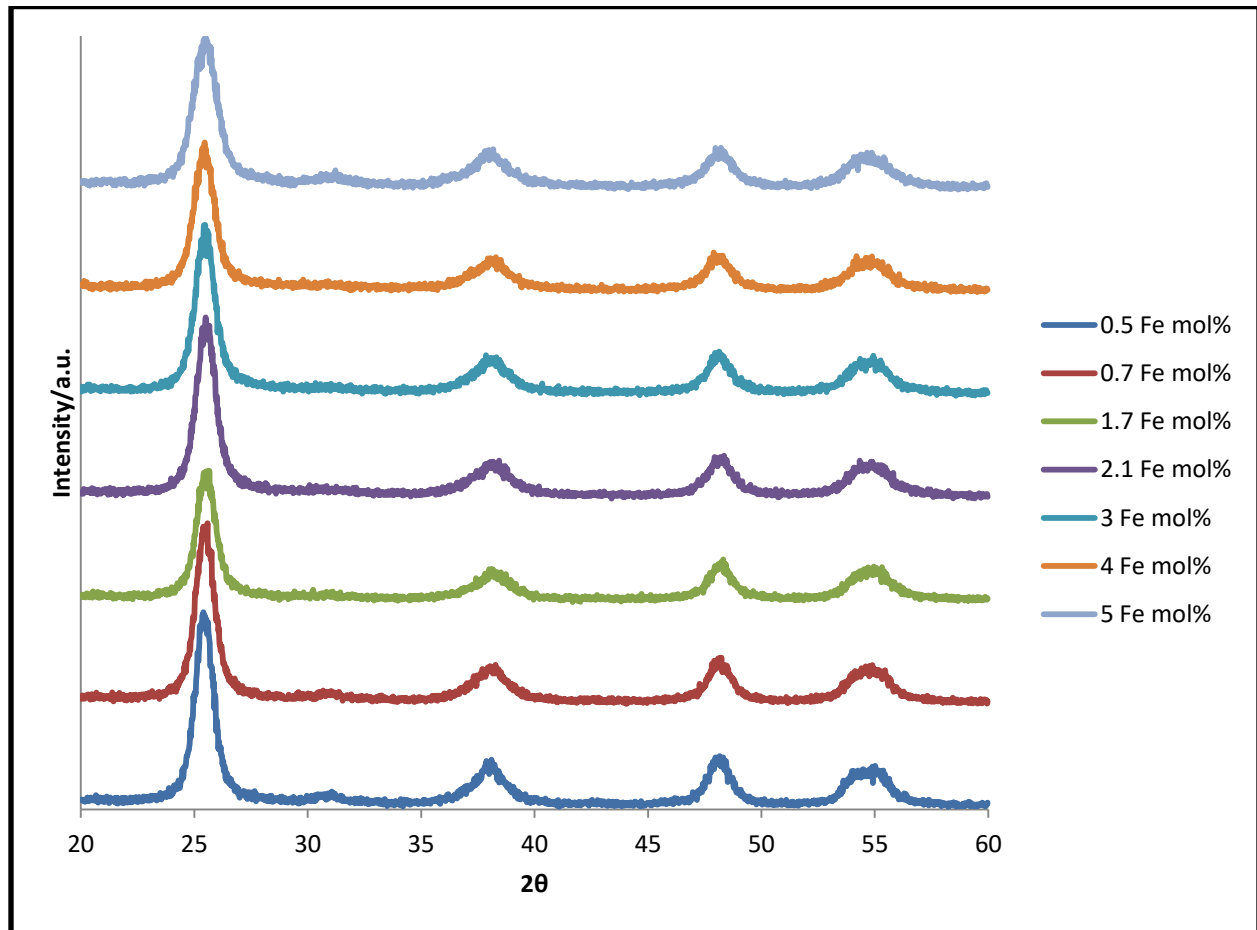


Figure (2-1). The powder XRD spectra of iron doped titanium dioxides according to the theoretical iron percentage as dopant.

The formation of brookite phase by addition of iron as dopant to the TiO₂ has been reported by Fàbrega *et al.* [13]. In Reference 13, pure TiO₂ is 100% anatase and all iron-doped TiO₂ materials have some contents of brookite. However, there is no meaningful relationship between the amount of iron and the amount of formed brookite [13]. There are several possible reasons behind this phenomenon. The change in concentration of iron used for the series of iron-doped TiO₂ nanomaterials can change the ionic strength of the reaction mixture, which affects condensation during the sol-gel process [14]. Popa *et al.* proposed that the formation of the brookite phase in iron-doped TiO₂ could arise from changes in the arrangement of the crystal structure, where the amount of the brookite phase increases by increasing the iron loading in the titanium dioxide [15]. Conversely, Crişan *et al.* claimed that increasing the amount of iron in the TiO₂ decreases the amount of brookite and increases anatase phase. However, these authors also came to the conclusion that the type of TiO₂ phases formed in the final product is strongly dependent not only on annealing parameters, but also on the factors taking part in the synthesis such as synthesis environment, reflux time, pH, solvent and type of precursors used [16]. Despite of effect of dopant on the brookite phase formation, it has been shown that the pH of reaction mixture has a crucial influence in this regard [17]. Concisely, the formation of brookite alongside with anatase is still a matter of debate between scientists and the reasons behind this need to be investigated more deeply in the future.

In order to reveal more detailed information about the composition and some other structural and physical features of the analyzed samples, all diffraction patterns were processed with the Rietveld profile fitting software Topas¹. As an example, the Rietveld fitting used for analysis of iron-doped TiO₂ containing 0.5 mol.% iron is demonstrated in Figure (2-2). There are no indications of the presence of another phase (component) in the samples rather than the two mentioned above. Special care was taken to detect possible traces of iron and iron oxides/hydroxides that could form as a result of doping. No such compounds were detected. As expected, this is due to the low concentration of iron in titanium dioxide matrix and formation of a solid solution [13]. It might be also due to low annealing temperature used for iron-doped materials (450 °C), since the formation temperature of iron phases such as Fe₂O₃ and Fe₂TiO₅ are 600°C and 800°C, respectively [13].

¹ Topas, v. 3.0, (2006) General profile and structure analysis software for powder diffraction data, User's Manual, Karlsruhe, Germany.

The calculated lattice plane spacing (d-spacing) for different planes in all samples for anatase as a tetragonal system show no meaningful difference with respect to introducing iron to TiO_2 crystal structure. This can be because of the very small difference between the ionic radius of Ti^{4+} and Fe^{3+} for coordination number 6, as explained in chapter 1. This is in accordance with the data reported previously, where a negligible difference in terms of d-spacing is found between the pure TiO_2 and iron-doped TiO_2 (up to 2.5 at.%) [19]. Similarly, the results from another study looking at anatase iron-doped titanium dioxide powders supports that a and c lattice constant values are not affected greatly by increasing iron dopant concentration from 0 to 10 wt.% [20].

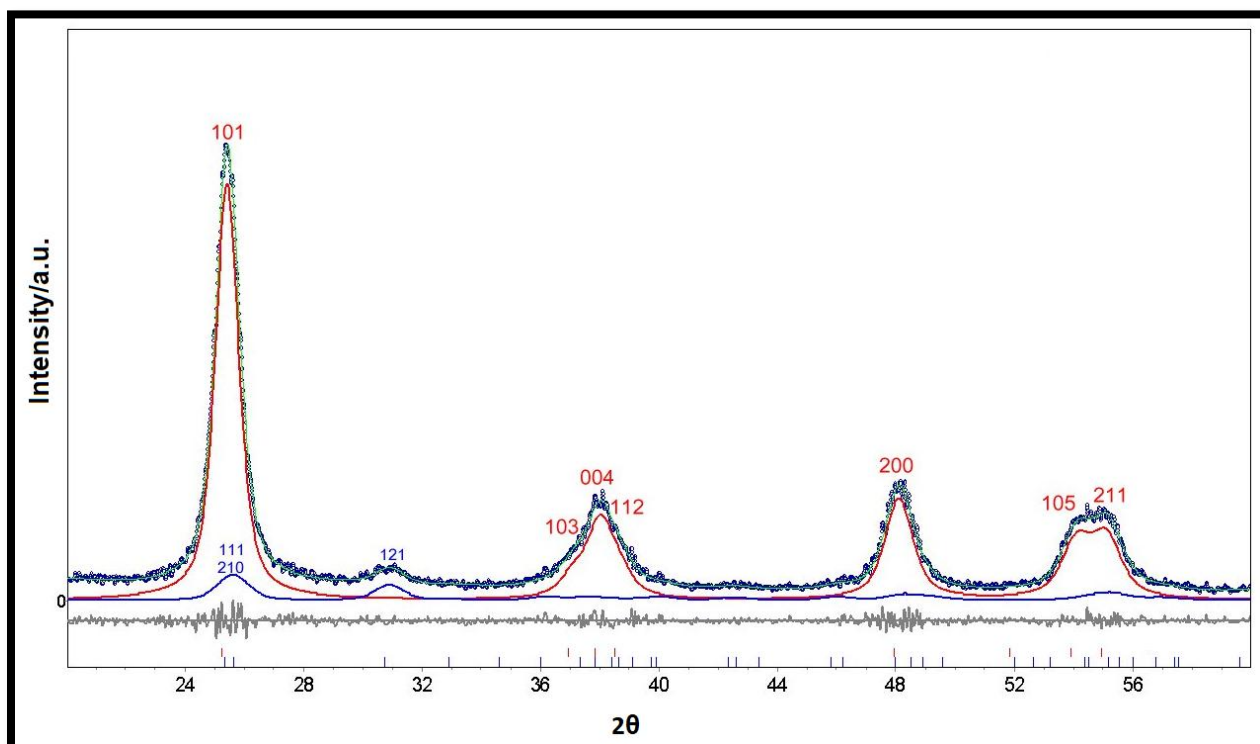


Figure (2-2). Rietveld fitting utilized for XRD pattern analysis of iron-doped TiO_2 (0.5 mol% iron).

The increasing distortion and broadening of the peaks by increasing the amount of iron in iron-doped titanium dioxides is an indication of distortion of the lattice and could be due to the

presence of iron as an impurity in the system. This result is in accordance with the fact that Fe^{3+} may be inserted in the TiO_2 matrix as a substituent for Ti^{4+} or interstitially located [21].

The quantitative analysis resulting from XRD method is demonstrated in table (2-2). It should be noted that the quantified amount of brookite phase in samples containing this phase of TiO_2 is overestimated due to the broadening of both anatase and brookite peaks as a result of peak overlap.

Table (2-2). XRD results for all samples.

Theoretical percentage of the iron (mol%)	0.5	0.7	1.7	2.1	3.0	4.0	5.0
Anatase (%)	88.03	88.61	100	100	100	100	83.63
Brookite (%)	11.97	11.39	0	0	0	0	16.37
Lo (nm) for anatase (± 2) [*]	9	15	14	22	18	27	12
Lo (nm) for brookite (± 2) [*]	6	6	NA	NA	NA	NA	6

(Lo=average grain size; NA=Not Applicable)

^{*}Uncertainties are calculated by fitting software Topas, which is used for Rietveld analysis.

2-3-2-1-2-Powder XRD diffraction of iron (III) oxide: The powder XRD pattern of iron (III) oxide is shown in Figure (2-3). The pattern obtained shows that the synthesized sample is composed of $\alpha\text{-Fe}_2\text{O}_3$ without any detectable impurity. The peaks at 33.05° and 35.39° are the two main characteristic signals attributed to Fe_2O_3 α -phase [22-23]. The XRD pattern matches the one reported in the literature as pure α -phase Fe_2O_3 (Figure (2-4)) [23] both in terms of the peaks' positions and intensities.

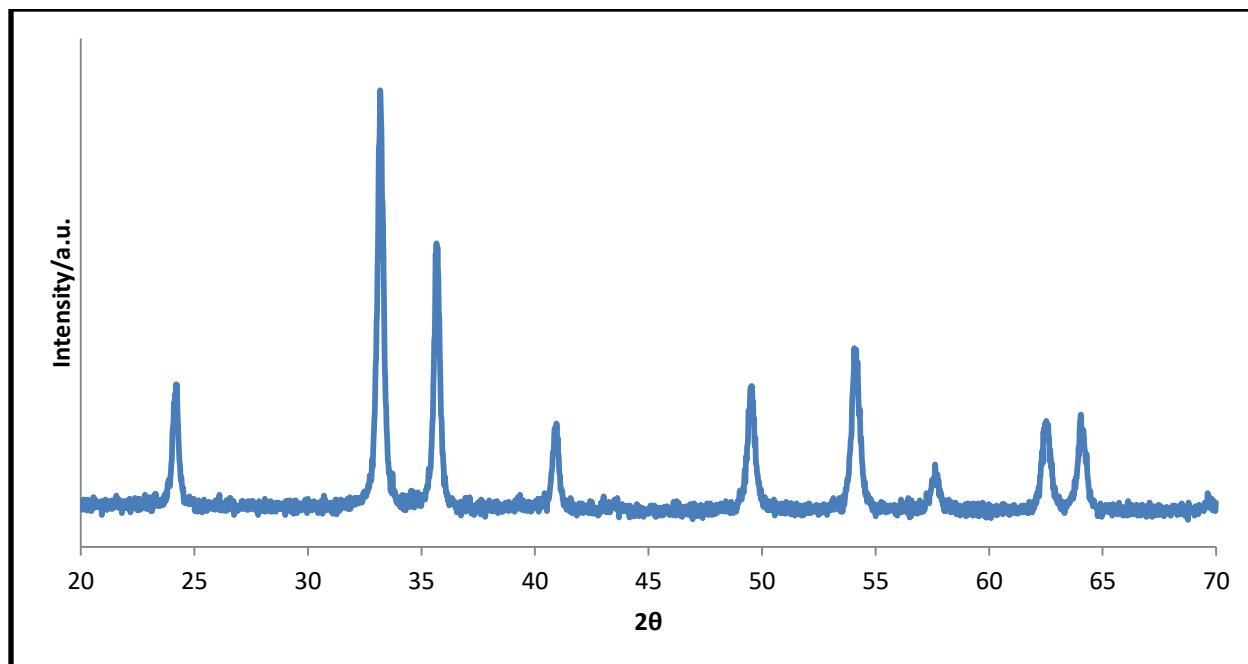


Figure (2-3). The powder XRD pattern of iron (III) oxide nanoparticles.

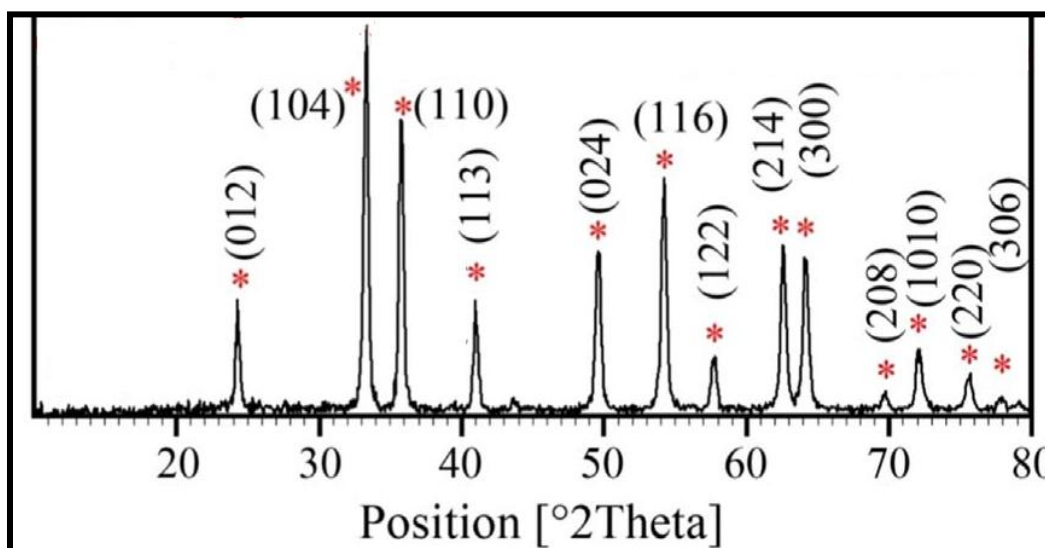


Figure (2-4). The powder XRD pattern of α -phase iron (III) oxide. Reprinted from reference [23], Copyright © 2016, With permission from Elsevier.

2-3-2-2-Diffusive Reflectance UV-Vis spectroscopy (UV-Vis DRS)

The DRS UV-Vis spectra of prepared doped titanium dioxide samples are presented in Figure (2-5).

The DRS UV-Vis spectrum of TiO₂ consists of a single and broad intense absorption band below 400 nm due to charge transfer from the valence band (mainly formed by 2p orbitals of the oxide anions) to the conduction band (mainly formed by 3d orbitals of the Ti⁴⁺ cations) [21].

Also, in the doped TiO₂ samples, absorption bands are shifted towards higher wavelength. This band shift is linked to a decrease in the band gap of the material upon doping, which is consistent with previously reported studies [24-25]. Delekar and his coworkers have shown that the band gap of titanium dioxide dropped from 3.23 to 2.26 eV by addition of 3 mol% of iron to titanium dioxide, which was only composed of the anatase phase [24]. In spite of the small change in the band gap, the reaction rate constant for photodegradation of Rhodamine 6G roughly doubles for the doped materials [24]. However, in another study, the TiO₂ band gap changed from 3.41 to 3.22 eV after doping with 5 % iron where the dominant detected phase is anatase with small amount of rutile [25]. This shows how dependent the band gap is on the structure of the material.

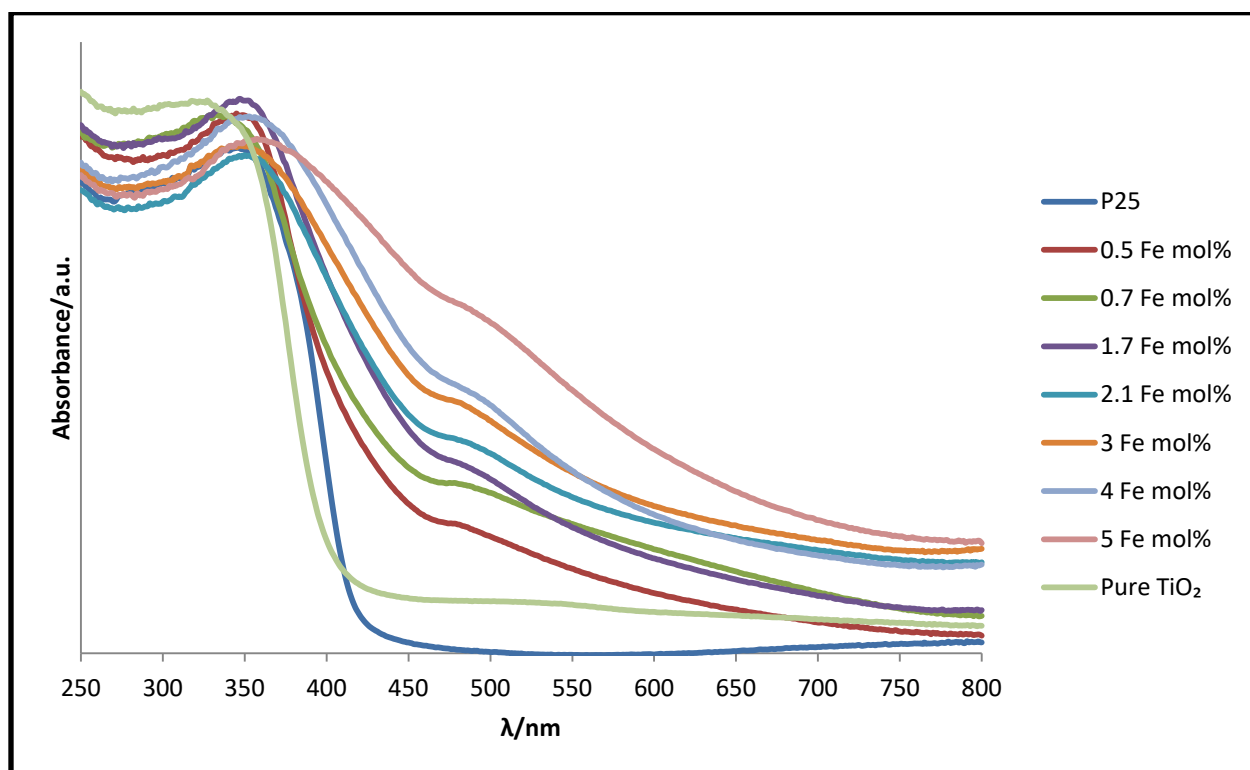


Figure (2-5). The DRS UV-Vis spectra of P25 (commercial TiO₂), pure synthesized TiO₂ and iron doped titanium dioxides.

In order to see if the observed trend in DRS UV-Vis spectra are a result of iron doping, solid mixtures composed of synthesized iron (III) oxide and synthesized pure titanium dioxide with molar ratios similar to doped samples, i.e. 0.7, 1.7 and 5 mol% iron were prepared and DRS UV-Vis was carried out.

Several factors have been considered as part of the literature review to find an appropriate procedure to synthesize Fe_2O_3 nanoparticles. First of all, the sol-gel method is selected as a simple and fast but efficient route for nanomaterial preparation. Secondly, it is noted that the synthesis method should be chosen in a way that the annealing temperature of 450 °C can be applied since this temperature was used for annealing the iron-doped titanium dioxides. Lastly, because of the similarity between the two protocols (for iron-doped TiO_2 and pure Fe_2O_3 particles preparation) it is expected that the particle size would be similar in all samples. This is important since the particle size can affect the optical properties in terms of light reflection and scattering. To ensure that all these concerns are taken into account, SEM, EDX and XRD were carried out as well to confirm our hypothesis.

The results are shown below in Figures (2-6) and (2-7). The spectrum of pure synthesized TiO_2 is added for comparison. As illustrated, the spectra of these mixtures are remarkably different from that of the iron-doped samples. The absorption band below 400 nm and around 500 nm correspond to TiO_2 and Fe_2O_3 , respectively. In spectra of doped samples, the TiO_2 absorption band has a higher intensity while in the mixtures, the iron (III) oxide bands are surprisingly much more intense and broader than what is observed in the doped-samples. In the doped samples, there is consistency between the titanium dioxide to Fe_2O_3 ratio and the absorbance intensity. This may support the formation of solid solutions that yields to a homogeneous distribution of iron atoms through the crystal structure of TiO_2 .

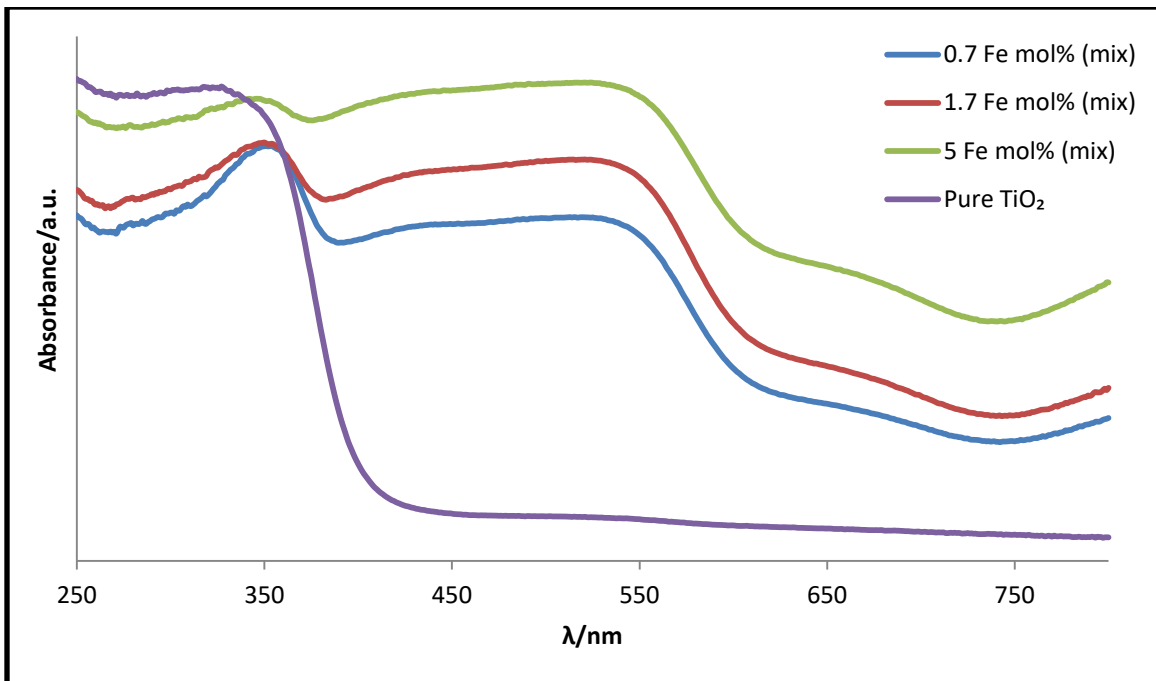


Figure (2-6). The DRS UV-Vis spectra of solid mixtures composed of synthesized iron (III) oxide and synthesized pure titanium dioxide with molar ratios similar to doped samples with 0.7, 1.7 and 5 mol% iron.

Moreover, the relationship between the intensity of iron (III) peak (at 480 nm) in DRS UV-Vis spectra of iron-doped samples and experimental molar percentage of iron (obtained from EDX data) has been studied (Figure (2-8)). As indicated, there is a linear relationship between these two parameters. This further supports the fact that the increase in absorbance after addition of iron to titanium dioxide can be attributed to extra energy levels that result from iron incorporation into TiO_2 structure.

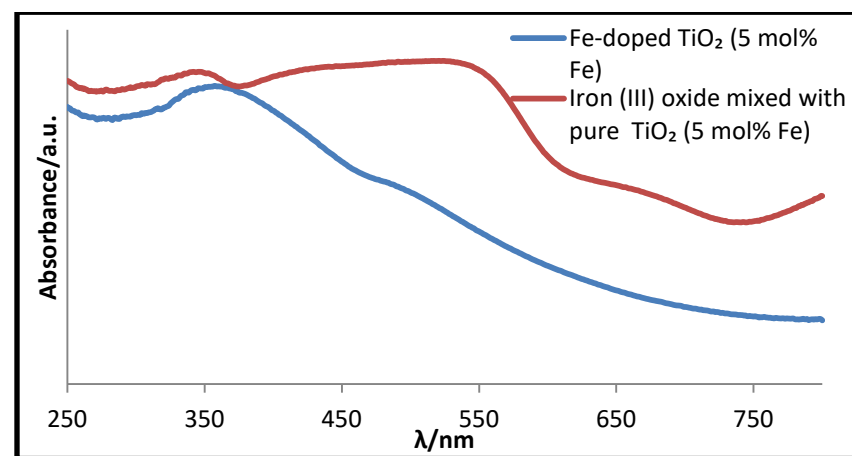
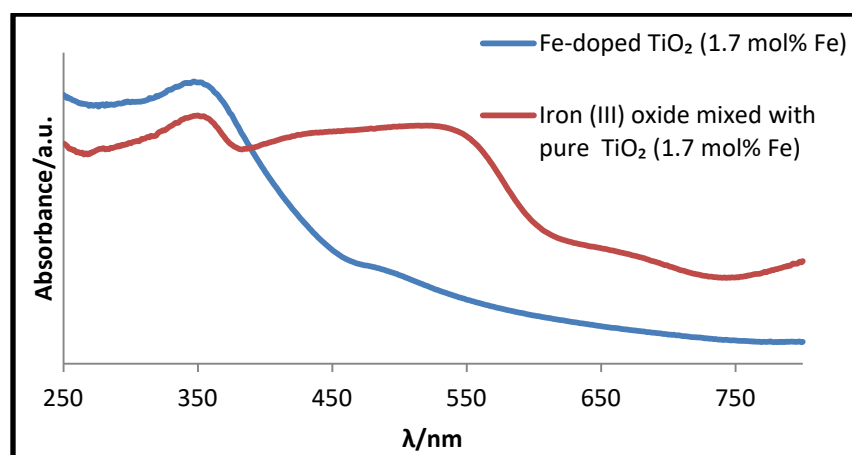
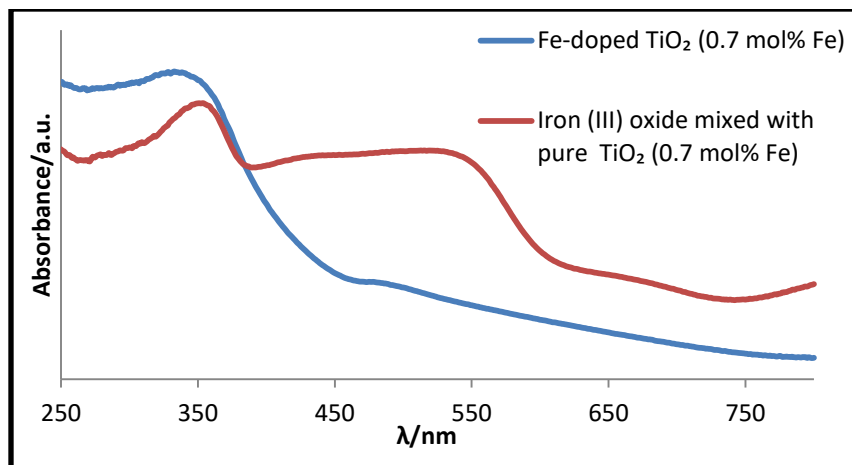


Figure (2-7). Comparison between the spectra of the iron-doped TiO₂ and its corresponding mixture of iron (III) oxide and titanium dioxide.

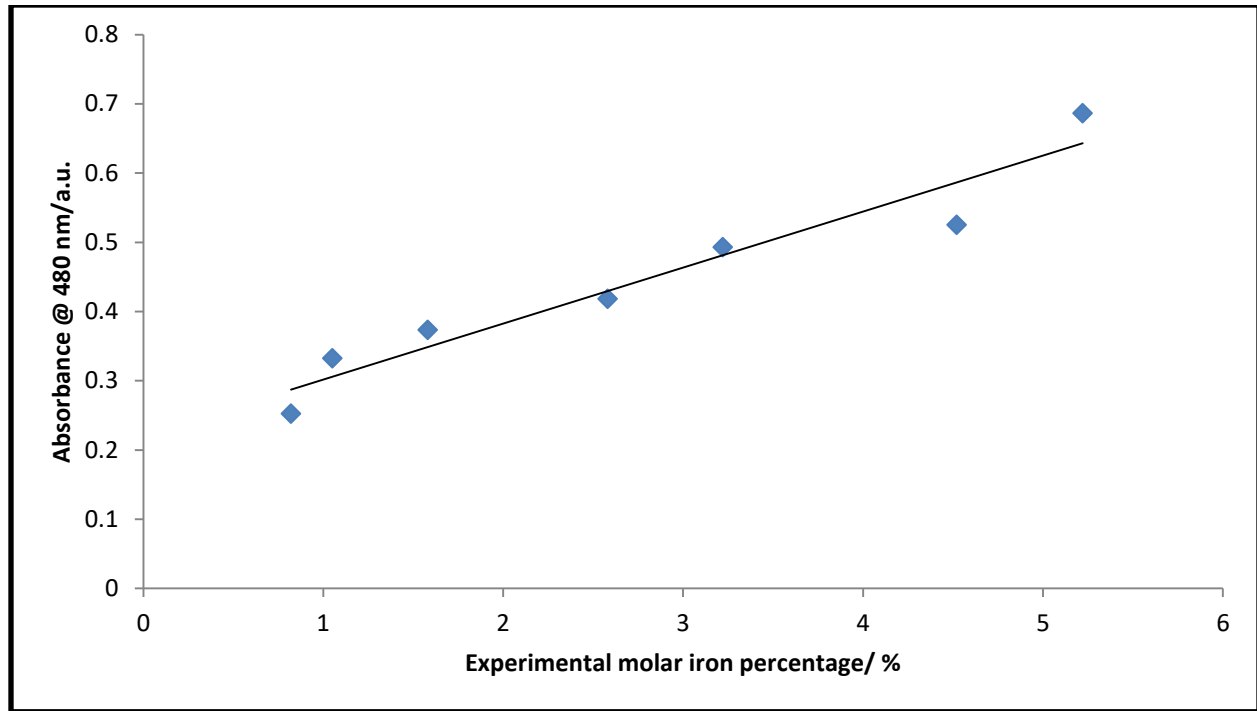


Figure (2-8). The linear relationship between iron (III) peak (at 480 nm) in DRS UV-Vis spectra of iron-doped samples and experimental molar percentage of iron (obtained from EDX data)

The band gap of the synthesized materials can be calculated based on the Kubelka-Munk theory. This theory is widely applied for analysis of the diffuse reflectance spectra obtained from weakly absorbing samples. The Kubelka-Munk equation at any wavelength is:

$$F(R) = \frac{(1-R)^2}{2R} \quad (3)$$

where R is the absolute reflectance of the sample and F(R) is the so-called Kubelka-Munk function. The mathematical relationship between the Kubelka-Munk function and absorbance is:

$$\alpha = \frac{F(R)}{t} \quad (4)$$

Here, α is called the linear absorption coefficient and t is the thickness of the layer of the tested material. There are two types of optical transitions in semiconductor materials, indirect and direct transitions. The value of the band gap can be calculated via the fundamental absorption,

which is correlated to the electronic transition from the valence band to conduction band. This optical band gap is determined by the following equation:

$$\alpha h\nu = \frac{F(R)h\nu}{t} = A(h\nu - E_g)^n \quad (5)$$

where A is an energy-independent constant, E_g is the optical band gap and n is a constant, which is dependent on the type of optical transition. The values of n are 0.5 and 2 for direct and indirect allowed transition, respectively. Titanium dioxide is known as a semiconductor with indirect band gap. Thus, by plotting $(\alpha h\nu)^{0.5}$ (or $(\frac{F(R)h\nu}{t})^{0.5}$ in this case) versus photon energy, $h\nu$, the direct band gap can be obtained. Extrapolation of the linear portion (at the point of inflection) to the x axis (photon energy axis) gives the optical band gap values as demonstrated for one sample in Figure (2-9) [26]. The extrapolation line fits the linear portion of the diagram by performing linear regression on these points.

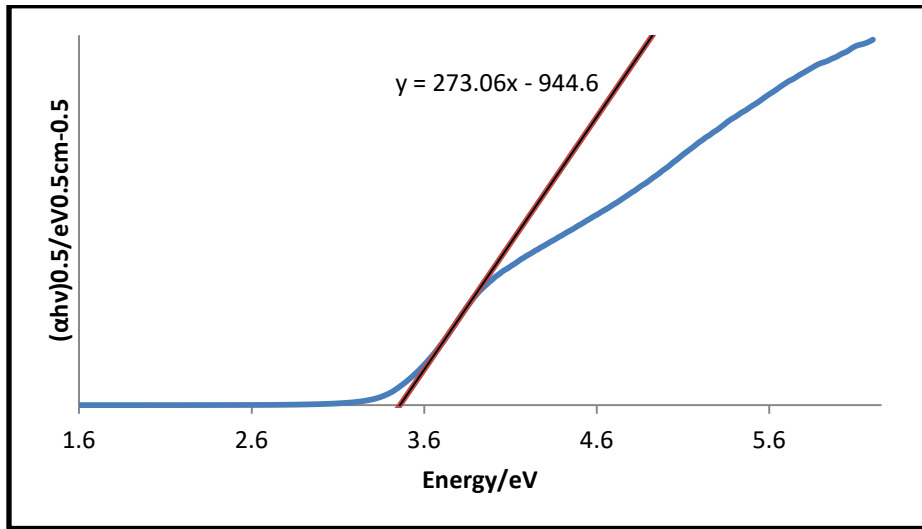


Figure (2-9). Extrapolation of the linear portion of the Kubelka-Munk diagram to the x axis (energy/eV) in order to find the band gap for one of the iron-doped TiO_2 samples.

However, there is much disagreement about the type of transition associated with experimental calculations of the band gap via this method for titanium dioxide [27]. In addition, various calculation methods were employed. In some papers, the band gap is calculated by directly plotting the absorbance versus λ [28-33] or by plotting %R versus λ [34-36]. Some other authors

estimated the band gap only by plotting α^2 versus λ or by plotting $\alpha^{1/2}$ versus λ [37-42]. Another point of contradiction is using direct and indirect allowed transition for evaluation of band gap in different publications [43-46]. *Lopez et al.* have done an extensive study in this regard by comparing different calculation methods. They showed that indirect allowed transition is highly preferred since it would ultimately give the most accurate results [27].

Table (2-3). The calculated band gaps of the prepared samples.

Theoretical percentage of the iron (mol%)	Pure TiO ₂	P25	0.5	0.7	1.7	2.1	3.0	4.0	5.0
Band gap (eV) (± 0.04)	3.12	3.05	2.90	2.84	2.76	2.64	2.50	2.38	2.30

The values obtained in our work are comparable with literature as presented in Figure (2-10). *Ganesh et al.* implemented a comparative study on calculation of band gaps [20]. It is shown that the band gap shifted from 3.214 to 2.904 eV by changing the concentration of iron from 0.1 to 5 wt% [20]. It was also demonstrated in a similar study that the band gap is decreased from 3.12 to 2.87 eV by doping titanium dioxide with 1.5 mol% iron [47]. *Delekar et al.* also showed that when 3 mol% iron is incorporated in the TiO₂ structure, the band gap is reduced from 3.23 to 2.26 eV [24]. *Wang et al.* found 1 mol% iron can lower the band gap of TiO₂ from 3.39 to 3.22 eV [48] These reported changes are comparable with our prepared materials.

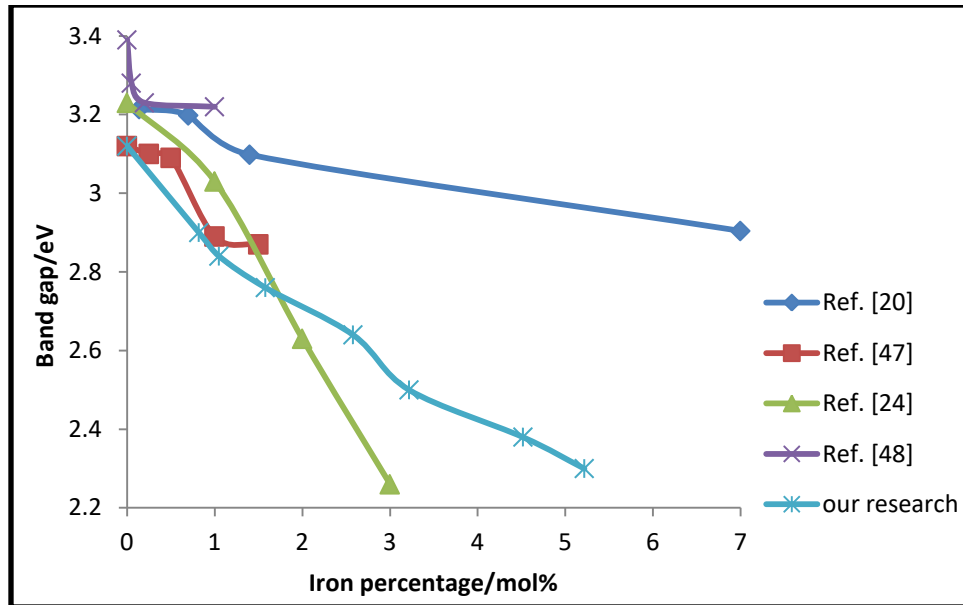


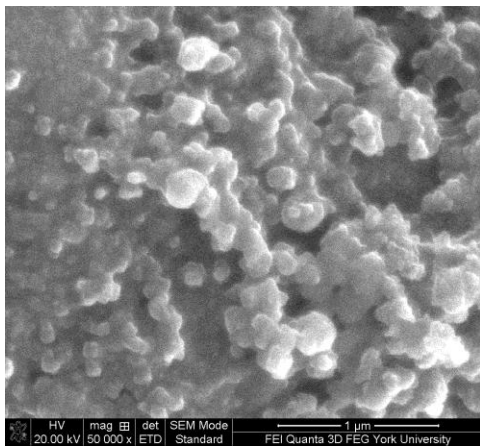
Figure (2-10). The band gap change by increasing the iron content in titanium dioxide in our study as well as some other publications.

2-3-2-3-Scanning electron microscopy (SEM)

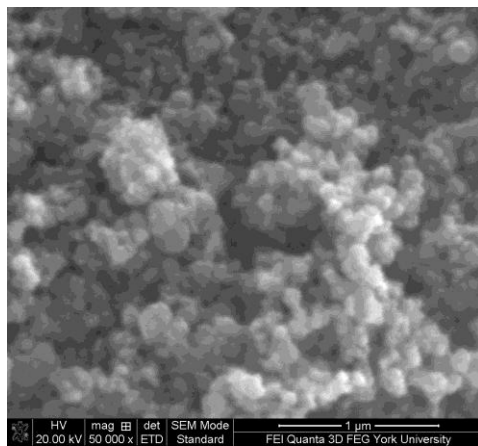
2-3-2-3-1-Scanning electron microscopy (SEM) of pure and iron-doped titanium dioxides:

The SEM images of synthesized materials are shown in Figure (2-11).

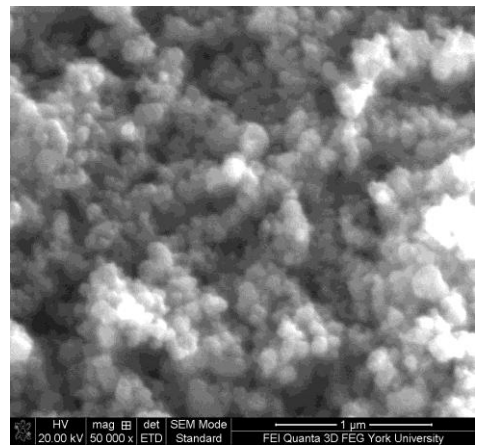
All the images are top view images that are representing the sample topography using a grey scale where lighter grey represent features that are positioned higher with respect to the sample support. All the images displayed below show that the samples consist of nanoparticles in the form of agglomerates. The size distribution of the agglomerates is broad but below 180 nm in diameter. These agglomerates form during synthesis, drying and annealing.



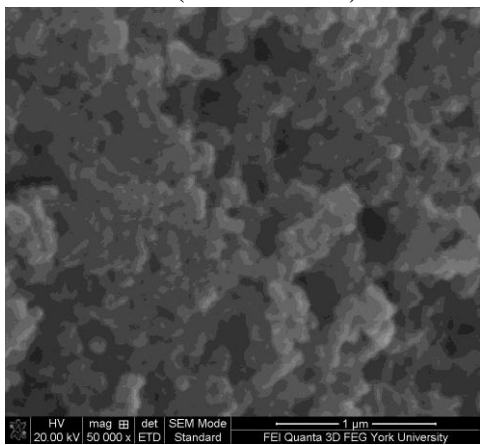
(0.5 mol% Fe)



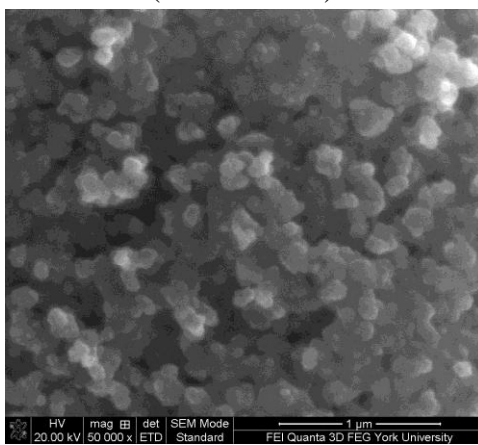
(0.7 mol% Fe)



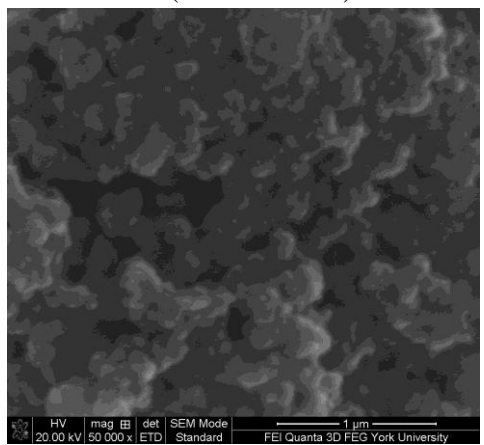
(1.7 mol% Fe)



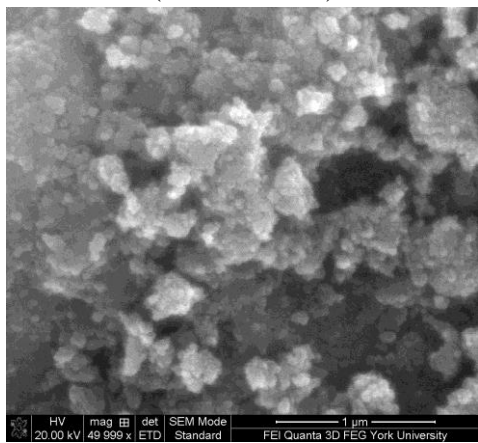
(2.1 mol% Fe)



(3.0 mol% Fe)



(4.0 mol% Fe)



(5.0 mol% Fe)

Figure (2-11). SEM images of the synthesized samples according to theoretical molar percentage of doped iron.

2-3-2-3-2-Scanning electron microscopy (SEM) images of iron (III) oxide: SEM analysis has been carried out on the iron (III) oxide sample in the form of a fine powder deposited on a piece of carbon tape. No gold coating is required for iron (III) oxide because it is conductive enough to obtain a proper image with an acceptable resolution. The obtained SEM image is depicted in Figure (2-12). The nanoparticles form agglomerates showing a similar spherical morphology. The size of the particles is estimated to be between 20 to 40 nm.

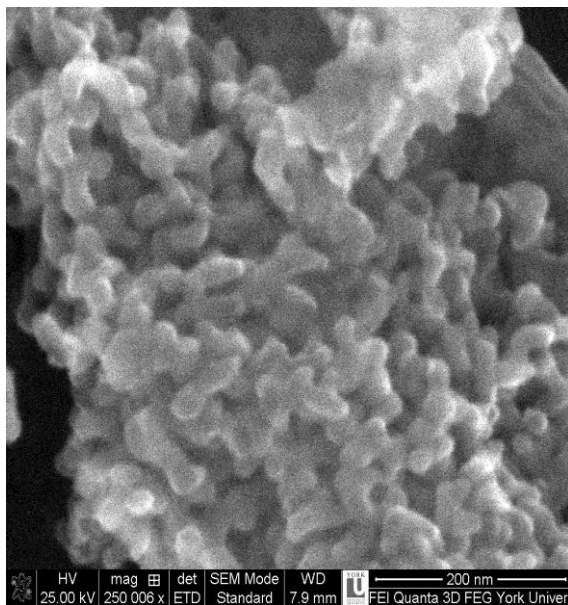


Figure (2-12). SEM image of iron (III) oxide nanoparticles.

2-3-2-4-Energy Dispersive X-ray (EDX) analysis

2-3-2-4-1-Energy Dispersive X-ray (EDX) analysis of pure and iron-doped titanium dioxide nanomaterials: The appearance of the gold peaks is a result of coating the samples with a very thin layer of this metal to avoid charging during imaging. The carbon peaks are attributed to the carbon tape employed to deposit titanium dioxide on the SEM sample holder. As expected, the titanium peaks are remarkably intense. Due to low concentrations of iron, the iron peaks have a very low intensity (Figure (2-13)). The outcome of this test for all samples is depicted in appendix 2.

The experimental mole percentages of the iron in various titanium dioxides are calculated based on EDX analysis and compared with the expected theoretical values in table (2-4) and Figure (2-

14). For each sample, multiple EDX measurements are carried out. Then, the average and standard deviation for samples are calculated and reported in the table below. For a majority of the samples, there is an acceptable agreement between the theoretical and experimental iron percentage values. These measurements show that the iron-doped titanium dioxides are prepared with an appropriate precision. Moreover, it demonstrates that most of the introduced iron is consumed during the course of the synthesis in order to produce a doped structure.

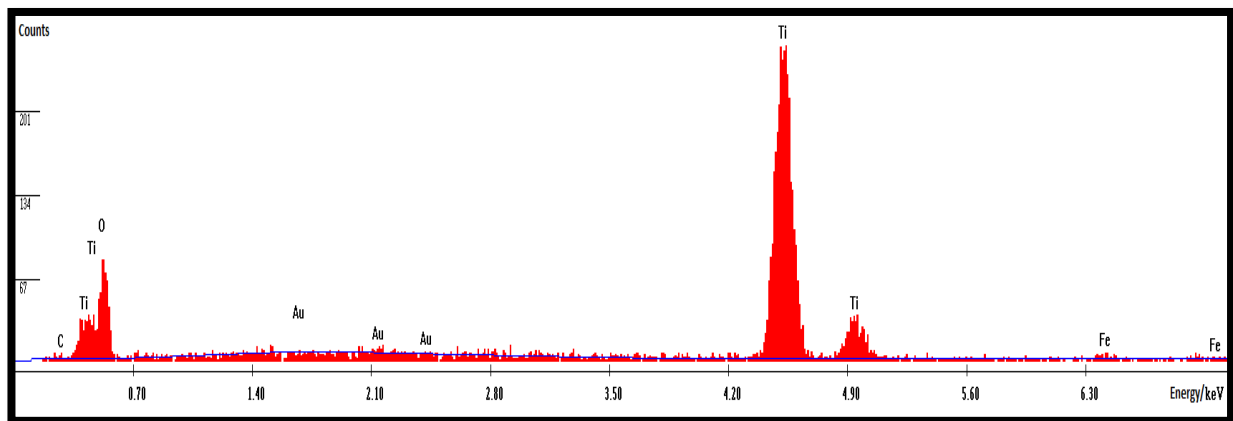


Figure (2-13). EDX spectrum of the typical iron-doped TiO_2

As mentioned previously, the data from powder XRD characterization provide no evidence for the presence of any iron oxide pure phases in all iron doped titanium dioxide samples. The EDX measurements support the existence of iron in all synthesized materials. As a result, it can be deduced that iron appears in the form of solid solution in all of our samples.

Table (2-4). The theoretical and real amount of iron as a dopant, based on the EXD results.

Mole percentage of iron based on EDX (real values)	0.82 ±0.22	1.05 ±0.20	1.58 ±0.65	2.58 ±0.17	3.22 ±0.58	4.52 ±0.31	5.22 ±1.0
Mole percentage of iron based on synthesis (theoretical values)	0.5	0.7	1.70	2.10	3.0	4.0	5.0

*Uncertainties are standard deviations obtained from three measurements at least.

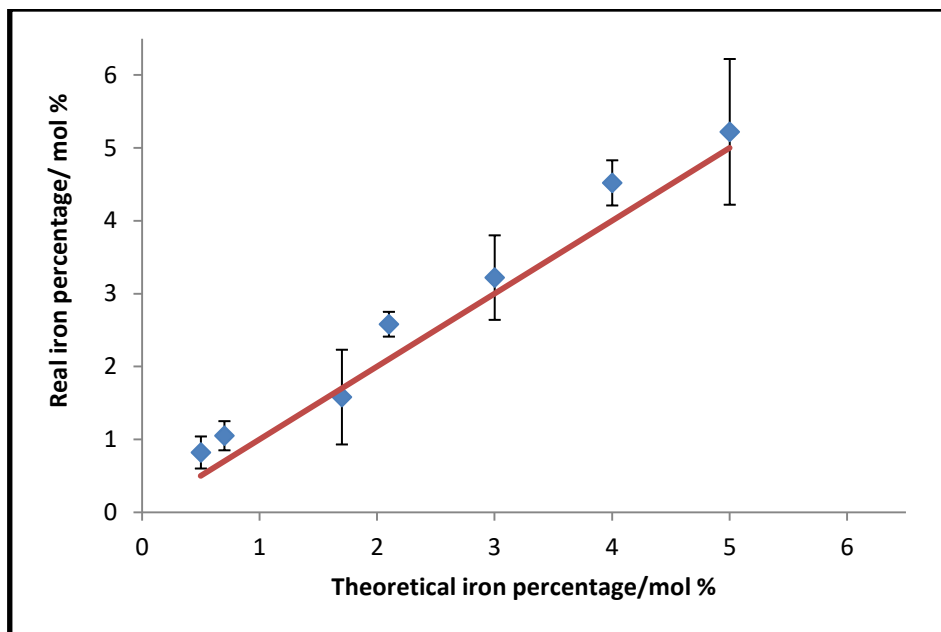


Figure (2-14). The relationship between the theoretical and the real amount of iron as a dopant, based on the EXD results.

2-3-2-4-2-Energy Dispersive X-ray (EDX) analysis of iron (III) oxide: The EDX spectrum is measured using the same equipment used to record the SEM images. The sample is deposited on a piece of carbon tape in the form of powder.

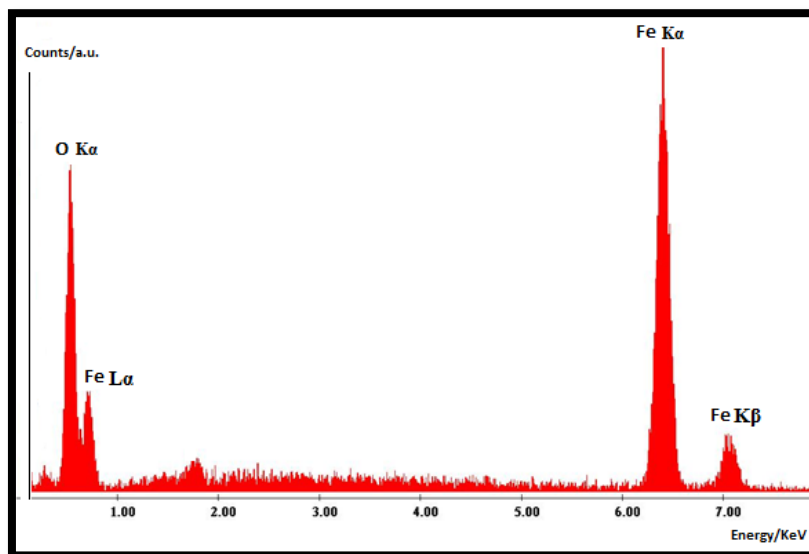


Figure (2-15). EDX analysis of α -Fe₂O₃

Figure (2-15) reports the EDX pattern obtained for iron (III) oxide. As it is expected, only iron and oxygen peaks are detected and it corresponds to pattern reported in the literature [49-50]. The intensity of $K\alpha$ peak is greater than $K\beta$ since the probability of filling the K vacancy shell by an electron in L shell is more than M shell. In addition, the $K\beta$ revealing higher energy because of larger energy gap between K and M shells compared to K and L ones.

2-3-2-5-Differential Scanning Calorimetry (DSC)

Differential scanning calorimetry (DSC) has been performed on three iron-doped titanium dioxides (Figure (2-16)). The DSC profile of all samples express similarities associated with different thermal events. The large endothermic signal below 150 °C is ascribed to loss of physically adsorbed moisture. The minor peaks between 150 °C and 450 °C are related to removal of chemically adsorbed water or other solvents as well as burning of some organic functional groups. This shows that the prepared samples are fairly free from impurities. Finally, phase transition from anatase to rutile happens around 540 °C [20,51].

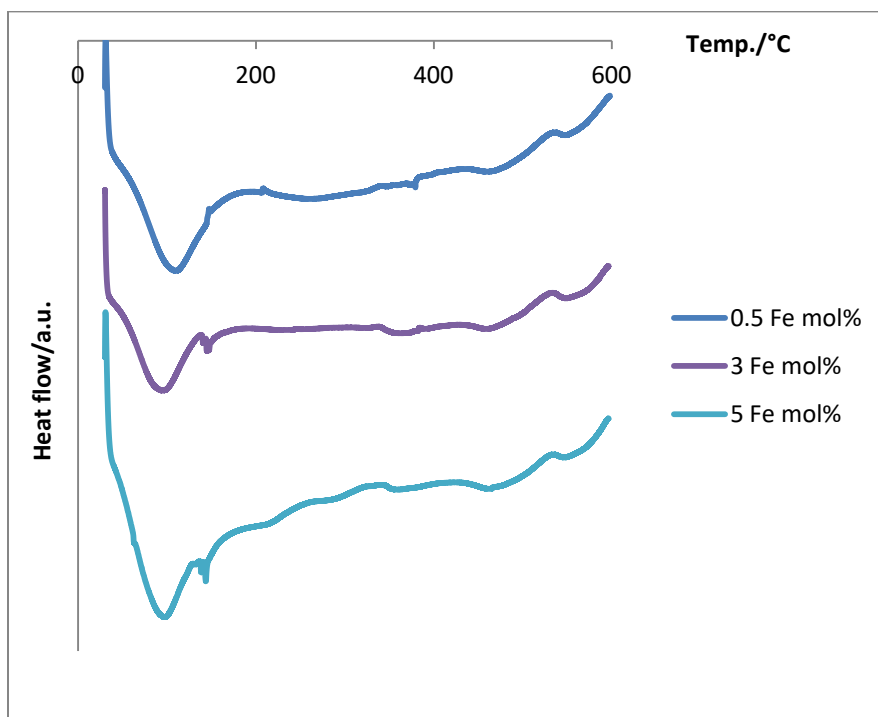


Figure (2-16). Differential scanning calorimetry (DSC) of three selected iron-doped titanium dioxides.

2-3-2-6-Cyclic Voltammetry (CV)

The experiments for the iron-doped TiO₂ with 5 mol% of iron is depicted in appendix 3. The very last one is represented in Figure (2-17).

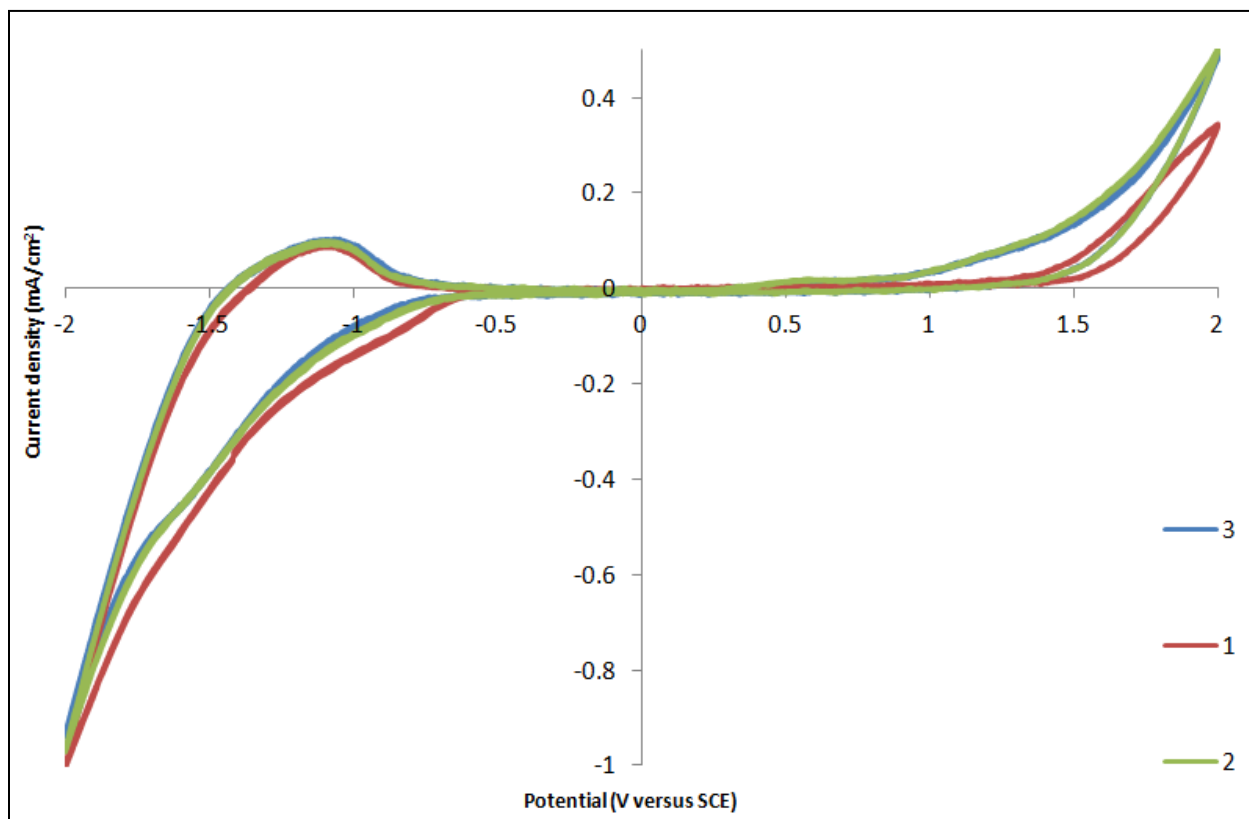
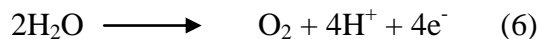
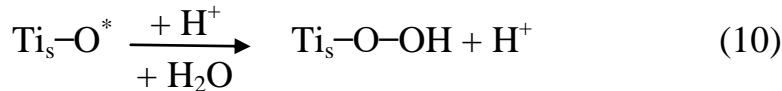
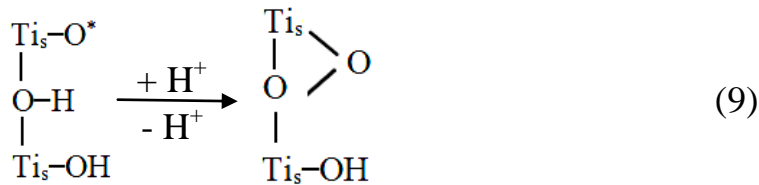
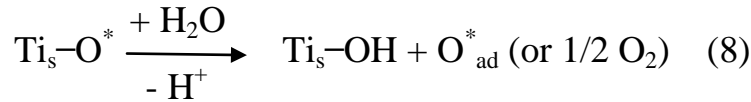
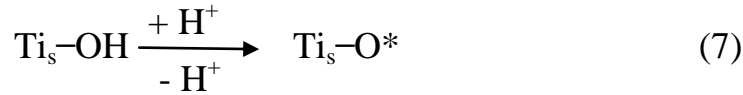


Figure (2-17). Cyclic voltammetry experiment for iron-doped TiO₂ (5 mol% Fe). CV is repeated for three cycles.

To have a clear picture of what has happened when the scan range is expanded, the third cycle from each measurement is selected and showed on one single diagram (Figure (2-18)). By widening the signal range toward negative potentials, both anodic and cathodic peaks are growing and the amount of measured current density is increasing. The cathodic peak located on the right hand side of the diagram (Figure (2-18)) is attributed to oxygen evolution reaction rising from water in the solvent as an impurity (OER) [52]:



The oxygen evolution potential is comparable with a value of 1455 mV versus SCE reported in the literature [52]. The observed pattern for the cyclic voltammetry of TiO₂ thin film is relatively similar [52-54]. However, there is a deviation between the reported potentials due to multiple parameters governing the experiment such as particle size, surface area, film thickness and the substrate used from TiO₂ film deposition [54]. The anodic oxygen evolution can also change the surface properties of titanium dioxide [52]. Some higher oxidation states of oxygen such as Ti_s-O* radicals (reaction No. 2; where Ti_s denotes the titanium atoms located on the surface of TiO₂), absorbed or adsorbed oxygen atoms (reaction No. 3) and titanium peroxo species (reactions No. 4 and 5) can form on the surface of titanium dioxide film. This can explain why the very first cycle of CV (Figure (2-17)) has a different oxygen evolution peak (showing a higher overpotential) compared to the second and third cycle. Another reason for this change can be the production of hydroxide ions as a result of hydrogen evolution, which react with H⁺ produced from oxygen evolution leading to the decrease of the oxygen evolution reaction overpotential.



The sharp anodic peak located at the far end of other side of the diagram (Figure (2-18)) corresponds to hydrogen evolution reaction (HER) [52,54]:



This region of the CV where the current grows rapidly is reported to appear at -1495 mV and -1200 mV versus SCE on the anodic and cathodic scans, respectively. These peaks were determined by testing TiO₂ with different properties, such as the change in particle size and also by changing the CV experimental parameters such as scan length [54].

The other anodic peak with lower intensity (roughly at -1.10 V) can be assigned to filling the surface states below the conduction band leading to the reduction of Ti⁴⁺ to Ti³⁺ on the surface of the oxide film, which is close in values to those reported in the literature: -0.8 V, -1.05 V, -1.25 V versus SCE [52-54]. At the same time, adsorption of positive species, e.g. proton or K⁺ on the surface of titanium dioxide takes place for reaching charge balance [54]

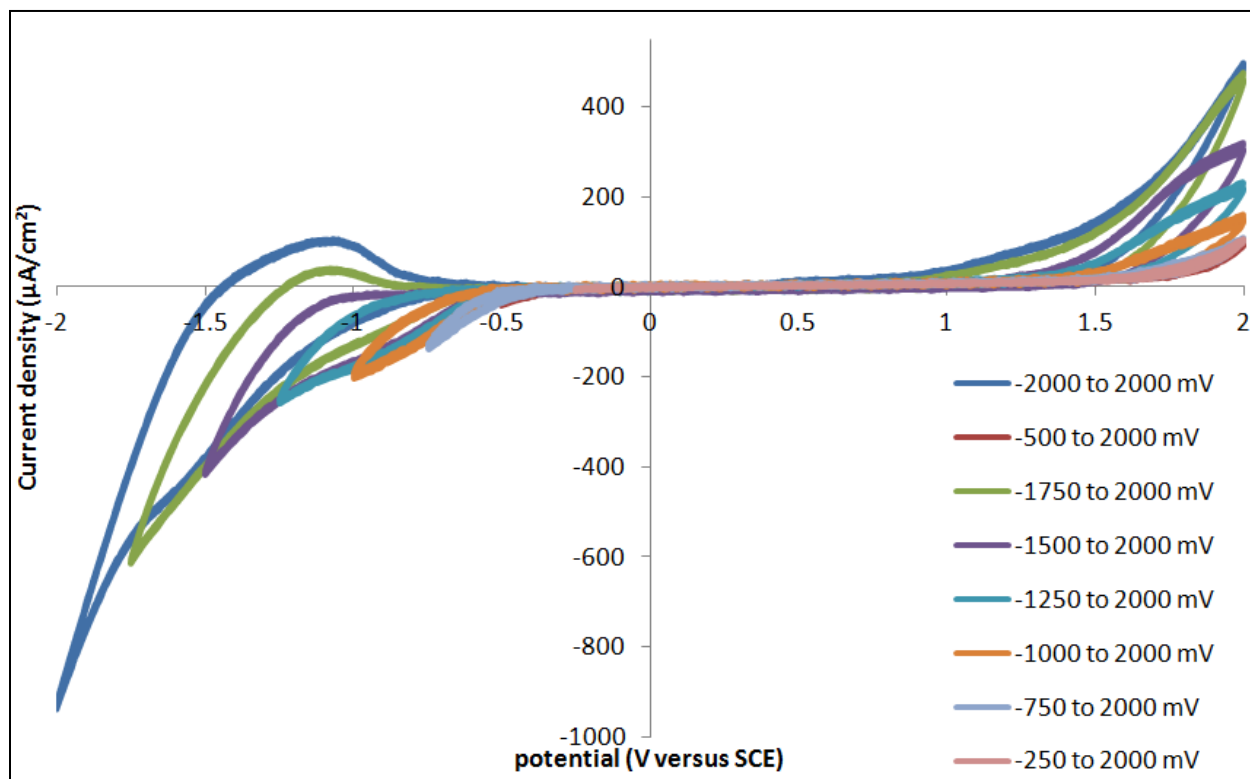
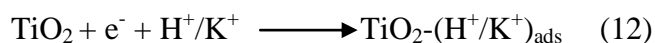


Figure (2-18). Cyclic voltammetry experiment for iron-doped TiO₂ (5 mol% Fe).

As a comparison, the same experimental method is repeated with a different electrolyte (0.1 M potassium perchlorate in water). The CV is very similar to that obtained in 0.1 M potassium

perchlorate in acetonitrile and DMF (Figure (2-19)). The current intensity at a given potential is higher in water compared to the organic solvent mixture. This can be related to lower electrical resistance of the aqueous solution as well as ease of accessibility of the TiO_2 surface to water for oxygen evolution and hydrogen evolution reactions.

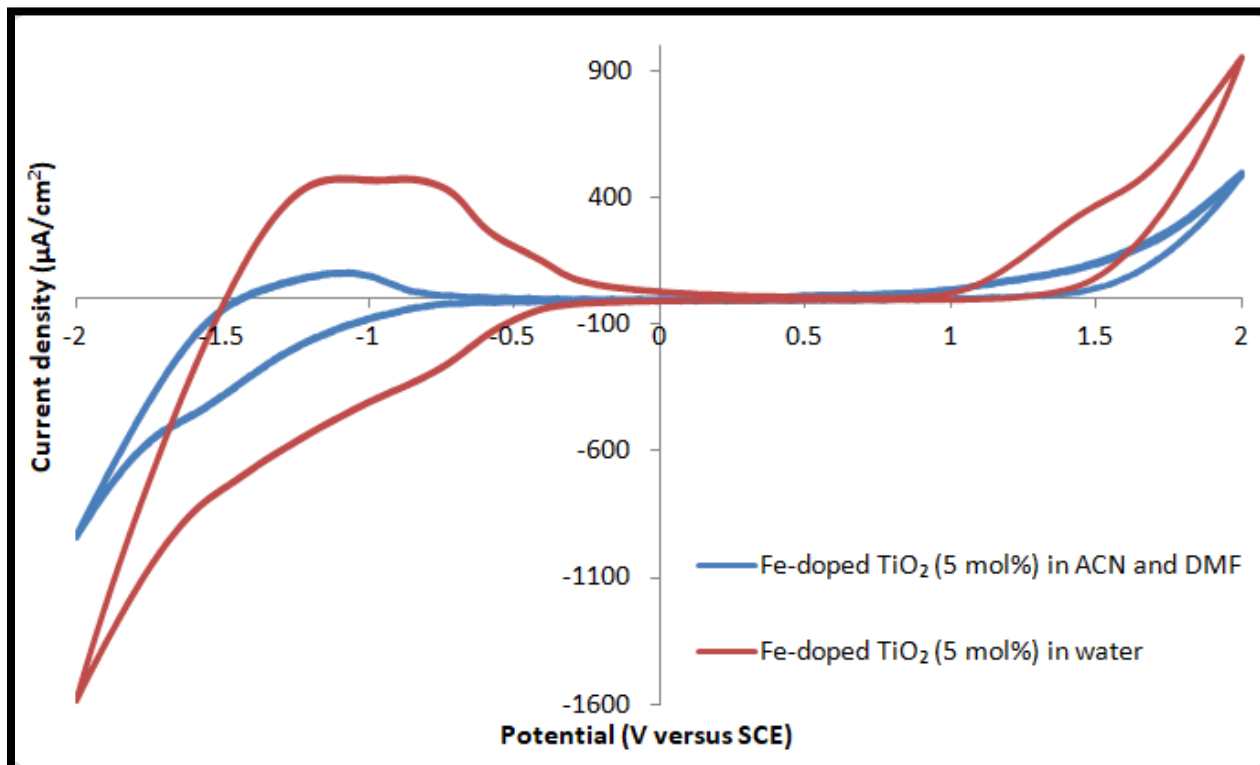


Figure (2-19). Cyclic voltammetry experiment for iron-doped TiO_2 (5 mol% Fe) in water (0.1 M potassium perchlorate) and also in acetonitrile and DMF (0.1 M potassium perchlorate).

The cyclic voltammogram of pure titanium dioxide is also compared with two iron-doped titanium dioxides with highest amount of iron (4 mol% and 5 mol% of iron) in Figure (2-20). The impact of iron as a dopant on the CV patterns is obvious. Addition of iron is increasing the overall conductivity of the TiO_2 . Both oxygen evolution peaks and hydrogen evolution peaks represent higher current densities. Typically, the oxidation peaks are weaker than the reduction peaks in nanoporous materials because of the larger band gap of this category of materials at higher potential [55]. Insertion of iron into the titanium dioxide matrix improves the oxidation peaks by decreasing the band gap.

Overall, it can be concluded that iron-doped titanium dioxide samples are potentially able to act as more effective catalysts compared to pure titanium dioxide.

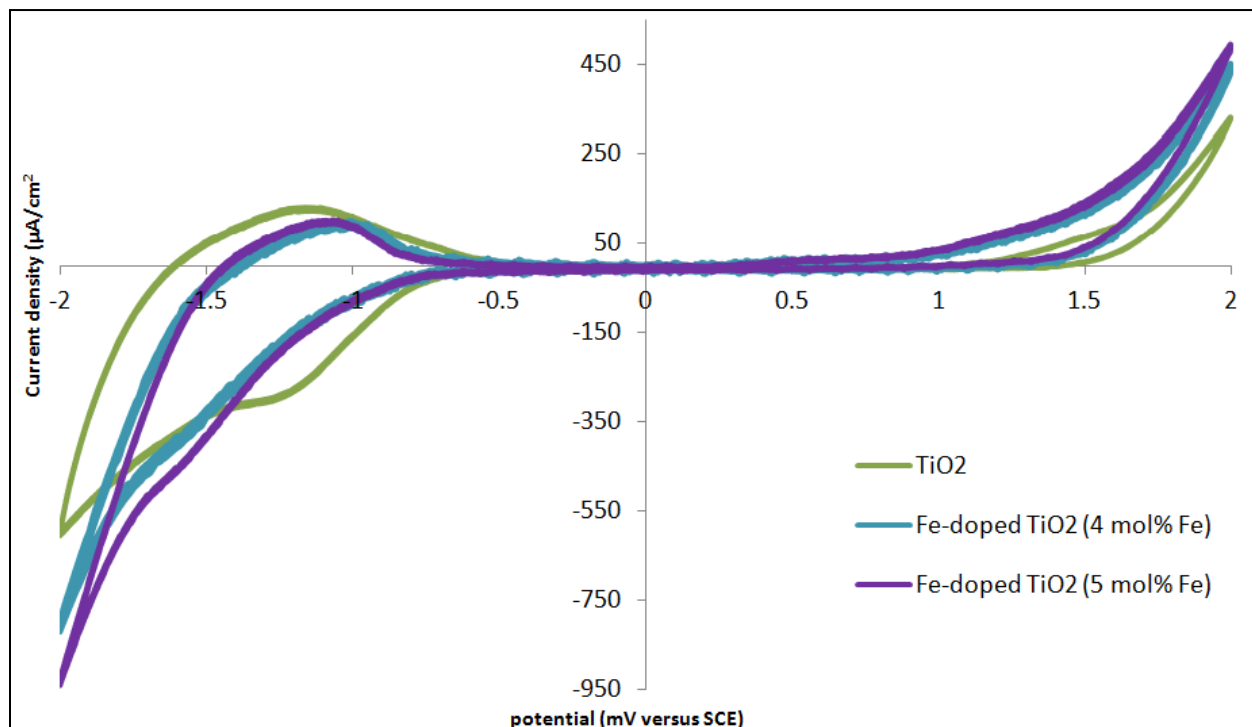


Figure (2-20). Cyclic voltammetry experiment for iron-doped TiO₂ (5 mol% and 4 mol% Fe) and pure TiO₂ in acetonitrile-DMF (0.1 M potassium perchlorate).

2-4-Conclusion

Iron-doped titanium dioxide nanomaterials with different percentages of iron have been prepared successfully. XRD patterns support this fact that all of our iron-doped samples are composed of mainly anatase. Brookite have been observed in few samples. No iron oxide or iron hydroxide phases are detected in any of the prepared materials. DRS UV-Vis prove that iron is successfully incorporated into the titanium dioxide matrix. Moreover, it shows us that the absorption edge of TiO₂ is shifted from UV to visible region by increasing the load of iron in titanium dioxide. SEM images demonstrate that all of our iron-doped titanium dioxide nanomaterials express the same morphology pattern in the form of agglomerated nanoparticles. EDX shows the existence of iron in our iron-doped TiO₂ samples as further proof of the successful synthesis of these

materials. CV shows that addition of iron to titanium dioxide has a significant impact on the electrochemical properties of titanium dioxide.

2-5-References

- [1] Bessekhoud Y.; Robert D.; Weber J. V.; *J. Photochem. Photobiol. A*, **2003**, 157, 47.
- [2] Oskam G.; Nellore A.; Penn R. L.; Searson P. C.; *J. Phys. Chem. B*, **2003**, 107, 1734.
- [3] Sugimoto T.; *Adv. Colloid Interface Sci.*, **1987**, 28, 65.
- [4] <https://arxiv.org/abs/cond-mat/0408480> (a document from Cornell University Library)
- [5] Kayani Z. N.; Arshad S.; Riaz S.; Naseem S.; *IEEE Trans. Magn.*, **2014**, 50, 8.
- [6] Azaroff L.; Kaplow R.; Kato N.; Weiss R. J.; Wilson A. J. C.; Young R. A.; *X-ray Diffraction*, **1974**, McGraw Hill.
- [7] Clegg W.; *Crystal Structure Determination*, **1998**, Oxford University Press, Oxford.
- [8] Cheney B.; *Introduction to Scanning Electron Microscopy*
http://www.sjsu.edu/people/anastasia.micheals/courses/MatE143/s1/SEM_GUIDE.pdf
- [9] Blaine R.L., "*The Case for a Generic Definition of Differential Scanning Calorimetry*", Du Pont Instruments, by DuPont Company.
- [10] Du Y.; Gan Y.; Yang P.; Cuie Z.; Hua N.; *Mater. Chem. Phys.*, **2007**, 103, 446.
- [11] Berger T.; Lana-Villarreal T.; Monllor-Satoca D.; Gomez R.; *J. Phys. Chem. C*, **2007**, 111, 9936.
- [12] Fabregat-Santiago F.; Mora-Sero I.; Garcia-Belmonte G.; Bisquert J.; *J. Phys. Chem. B*, **2003**, 107, 758.
- [13] Fàbrega C.; Andreu T.; Cabot A.; Morante J. R.; *J. Photochem. Photobiol. A*, **2010**, 211, 170.
- [14] Andriamiadamanana C.; Laberty-Robert C.; Sougrati M. T.; Casale S.; Davoisne C.; Patra S.; Sauvage F.; *Inorg. Chem.*, **2014**, 53, 10129.
- [15] Popa M.; Diamandescu L.; Vasiliu F.; Teodorescu C. M.; Cosoveanu V.; Baia M.; Feder M.; Baia L.; Danciu V.; *J. Mater. Sci.*, **2009**, 44, 358.

- [16] Crişan M.; Răileanu M.; Drăgan N.; Crişan D.; Ianculescu A.; Niţoi I.; Oancea P.; şomăcescu S.; Stănică N.; Vasile B.; Stan C.; *Appl. Catal., A*, **2015**, 504, 130.
- [17] Cassaignon S.; Koelsch M.; Jolivet J. -P.; *J. Phys. Chem. Solids*, **2007**, 68, 695.
- [18] Qi K.; Fei B.; Xin J. H.; *Thin Solid Films*, **2011**, 519, 2438.
- [19] Wang C.; Böttcher C.; Bahnemann D. W.; Dohrmann J. K.; *J. Mater. Chem.*, **2003**, 13, 2322.
- [20] Ganesh I.; Kumar P. P.; Gupta A. K.; Sekhar P. S. C.; Radha K.; Padmanabham G.; Sundararajan G.; *Processing and Application of Ceramics*, **2012**, 6, 21.
- [21] Avasarala B. K.; Tirukkovaluri S. R.; Bojja S.; *J. Hazard. Mater.*, **2011**, 186, 1234.
- [22] Kayani Z. N.; Arshad S.; Riaz S.; Naseem S.; *IEEE Trans. Magn.*, **2014**, 50(8), 2200404.
- [23] Davar F.; Hadadzadeh S.; Sadat Alaedini T.; *Ceram. Int.*, **2016**, 42, 19336.
- [24] Delekar S. D.; Yadav H. M.; Achary S. N.; Meena S. S.; Pawar S. H.; *Appl. Surf. Sci.*, **2012**, 263, 536.
- [25] Dholam R.; Patel N.; Adami M.; Miotello A.; *Int. J. Hydrogen Energy*, **2009**, 34, 5337.
- [26] Aydin C.; Abd El-Sadek M. S.; Zheng K.; Yahia I. S.; Yakuphanoglu F.; *Opt. Laser Technol.*, **2013**, 48, 447.
- [27] López R.; Gómez R.; *J. Sol-Gel Sci. Technol.*, **2012**, 61, 1.
- [28] Khan S.; Al-Shahry M.; Ingler W. B.; *Science*, **2002**, 297, 2243.
- [29] Yang J.; Bai H.; Tan X.; Lian J.; *Appl. Surf. Sci.*, **2006**, 253, 1988.
- [30] He C.; Li X. Z.; Graham N.; Wang Y.; *Appl. Catal. A*, **2006**, 305, 54.
- [31] Graf C.; Ohser-Wiedemann R.; Kreisel G.; *J. Photochem. Photobiol. A*, **2007**, 188, 226.
- [32] Gómez R.; López T.; Ortiz-Islas E.; Navarrete J.; Sánchez E.; Tzompantzi F.; Bokhimi X.; *J. Mol. Catal. A Chem.*, **2003**, 193, 217.
- [33] López T.; Hernandez-Ventura J.; Gómez R.; Tzompantzi F.; Sánchez E.; Bokhimi X.; García A.; *J. Mol. Catal. A Chem.*, **2001**, 167, 101.

- [34] Tang H.; Prasad K.; Sanjines R.; Schmid P. E.; Lévy F.; *J. Appl. Phys.*, **1994**, 75, 2042.
- [35] Fan X.; Yu T.; Zhang L.; Chen X.; Zou Z.; *J. Chem. Phys.*, **2007**, 20, 733.
- [36] Sudhagar P.; Sathyamoorthy R.; Chandramohan S.; *Appl. Surf. Sci.*, **2008**, 254, 1919.
- [37] Kumar P.; Malhotra L. K.; *Electrochim. Acta*, **2004**, 49, 3355.
- [38] Lekha P. C.; Subramanian E.; Padiyan D. P.; *Sens. Actuators B*, **2007**, 122, 274.
- [39] Herman D.; Sicha J.; Musil J.; *Vacuum*, **2006**, 81, 285
- [40] Simpson J. R.; Drew H. D.; *Phys. Rev. B*, **2004**, 69, 193205.
- [41] Miao L.; Jin P.; Kaneko K.; Terai A.; Nabatova-Gabain N.; Tanemura S.; *Appl. Surf. Sci.*, **2003**, 212, 255.
- [42] Beke S.; Giorgio S.; Körösi L.; Nánai L.; Marine W.; *Thin Solid Films*, **2007**, 516, 4659.
- [43] Stengl V.; Bakardjieva S.; Murafa N.; Houskova V.; Lang K.; *Micropor. Mesopor. Mater.*, **2008**, 110, 370.
- [44] Ryu S. Y.; Balcerski W.; Lee T. K.; Hoffmann M. R.; *J. Phys. Chem. C*, **2007**, 111, 18195.
- [45] Zaghbi K.; Mauger A.; Goodenough J. B.; Gendron F.; Julien C. M.; *Chem. Mater.*, **2007**, 19, 3740.
- [46] Li Q.; Xie R.; Li Y. W.; Mintz E. A.; Shang J. K.; *Environ. Sci. Technol.*, **2007**, 41, 5050.
- [47] Christoforidis K. C.; Iglesias-Juez A.; Figueroa S. J. A.; Di Michiel M.; Newton M. A.; Fernández-García M.; *Catal. Sci. Technol.*, **2013**, 3, 626.
- [48] Wang C.; Siao H.; Chiu Y.; *Surf. Coat. Tech.*, **2013**, 232, 658.
- [49] Mansour A. M.; *RSC Adv.*, **2015**, 5, 62052.
- [50] Cheng Z.; Tan L. A. K.; Tao Y.; Shan D.; Ting K. E.; Yin X. J.; *Int. J. Photoenergy*, Volume 2012 (2012), Article ID 608298, 5 pages.
- [51] Kim H.; Jeong K.; Bae D.; *Kor. J. Mater. Res.*, **2012**, 22(5), 249.
- [52] Han J.; Choi H.; Lee J.; Tak Y.; Yoon J.; *J. Electrochem. Sci. Technol.*, **2016**, 7(1), 76.
- [53] Kong D.; Wu J.; *J. Electrochem. Soc.*, **2008**, 155 (1), C32.
- [54] Löberg J.; Holmberg J. P.; Mattisson I.; Arvidsson A.; Ahlberg E.; *Int. J. Dent.*, Volume 2013, Article ID 139615.

[55] Li J.; Han T.; Wei N.; Du J.; Zhao X.; *Biosens. Bioelectron.*, **2009**, 25, 773.

[56] Monai M.; Montini T.; Fornasiero P.; *Catalysts*, **2017**, 7(10), 304.

2-6-Appendix 1: XRD patterns of pure anatase, pure brookite and pure rutile

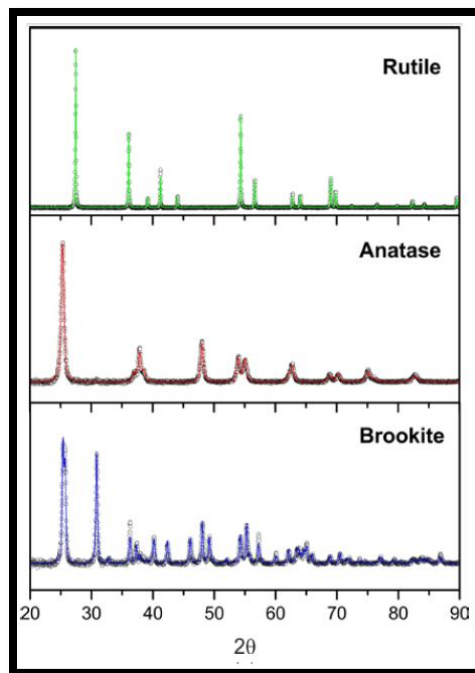
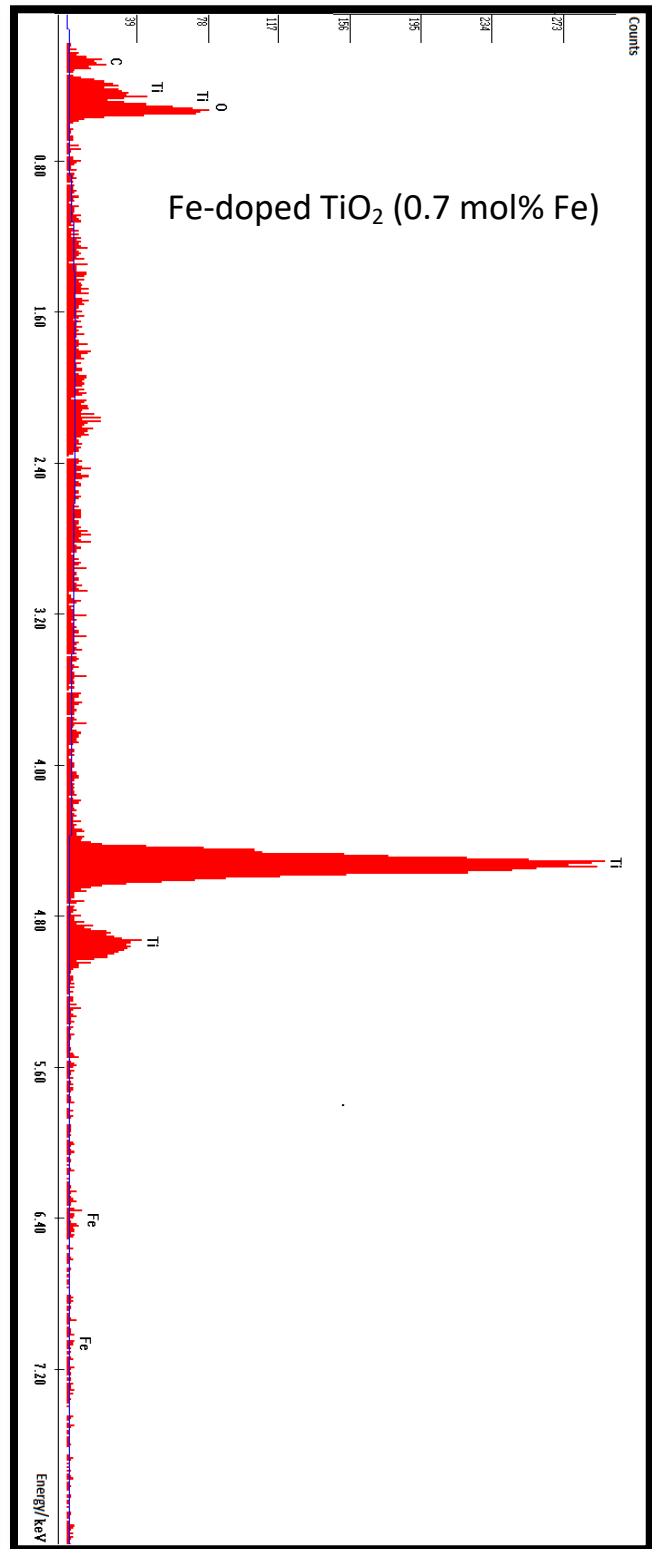
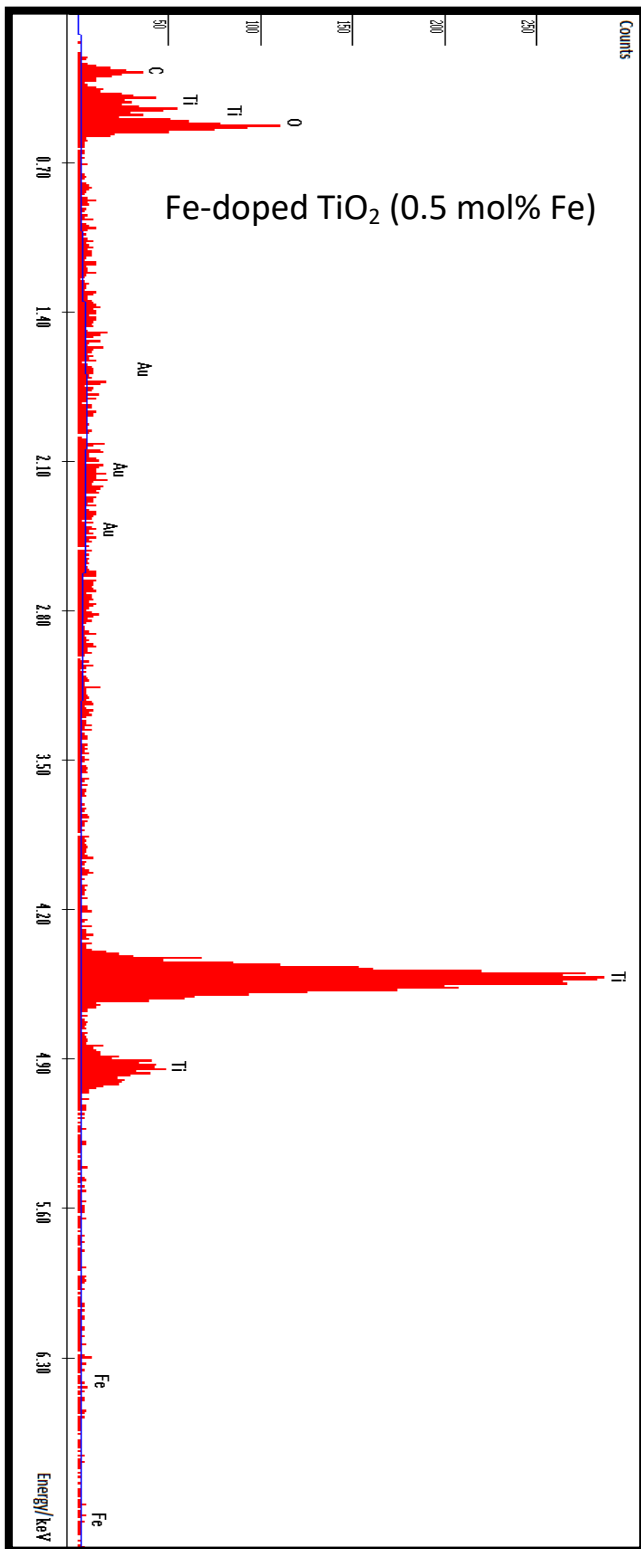
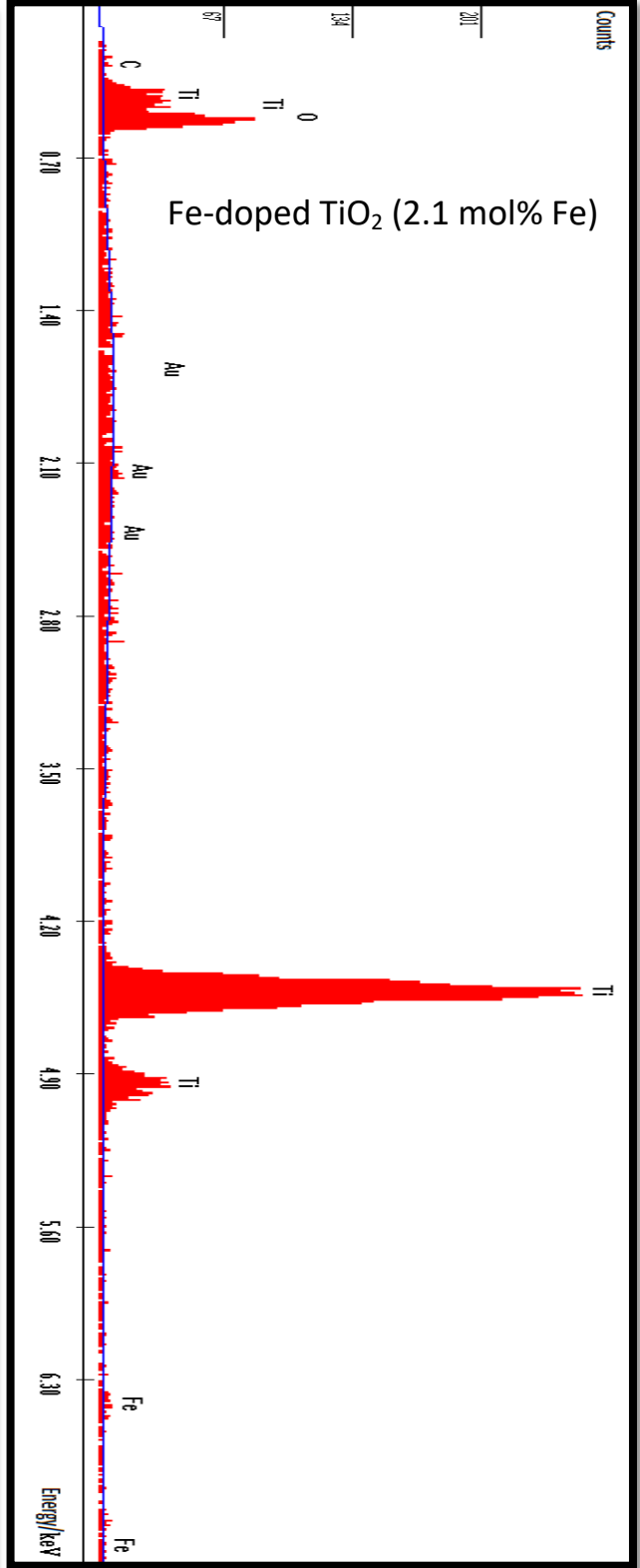
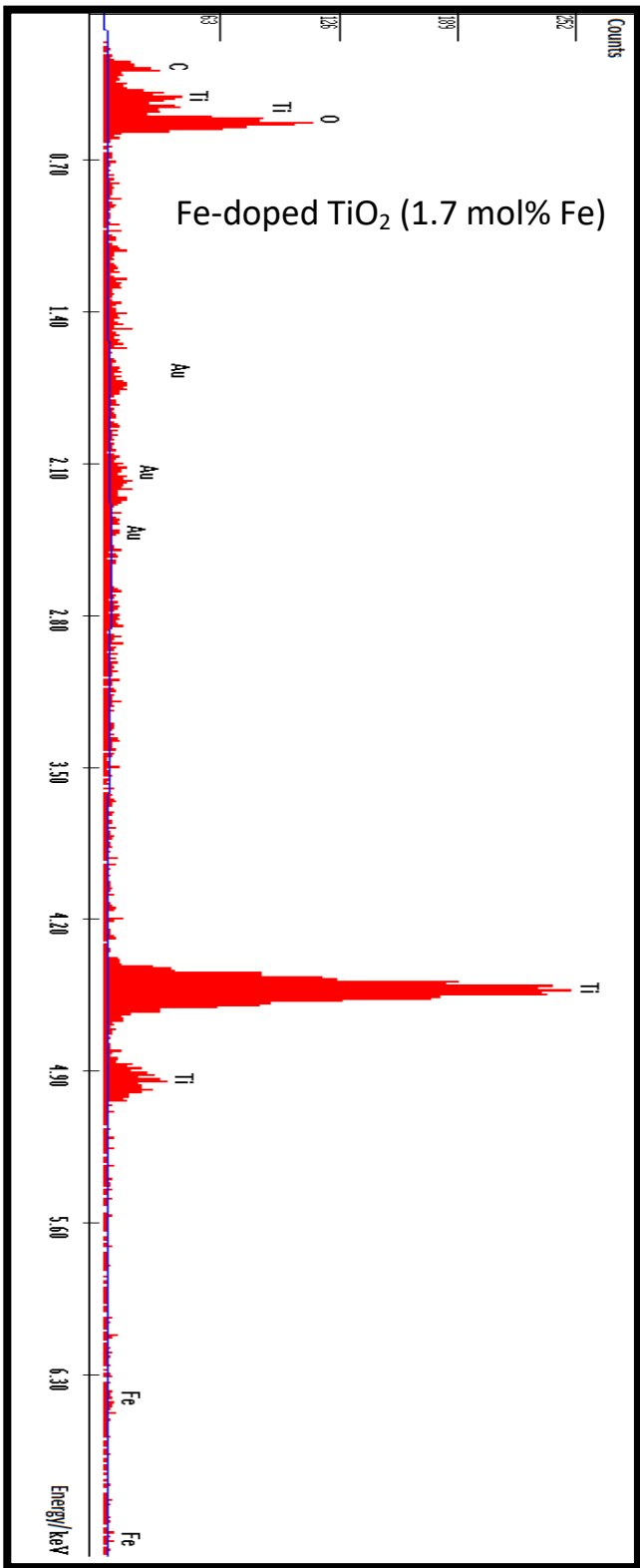


Figure (2-21). XRD-pattern of pure anatase, pure brookite and pure rutile. Republished from open-access reference [56] © 2017 by the authors. Licensee MDPI, Basel, Switzerland, <https://www.mdpi.com/2073-4344/7/10/304>.

2-7-Appendix 2: EDX experiment for all iron-doped TiO₂ nanomaterials





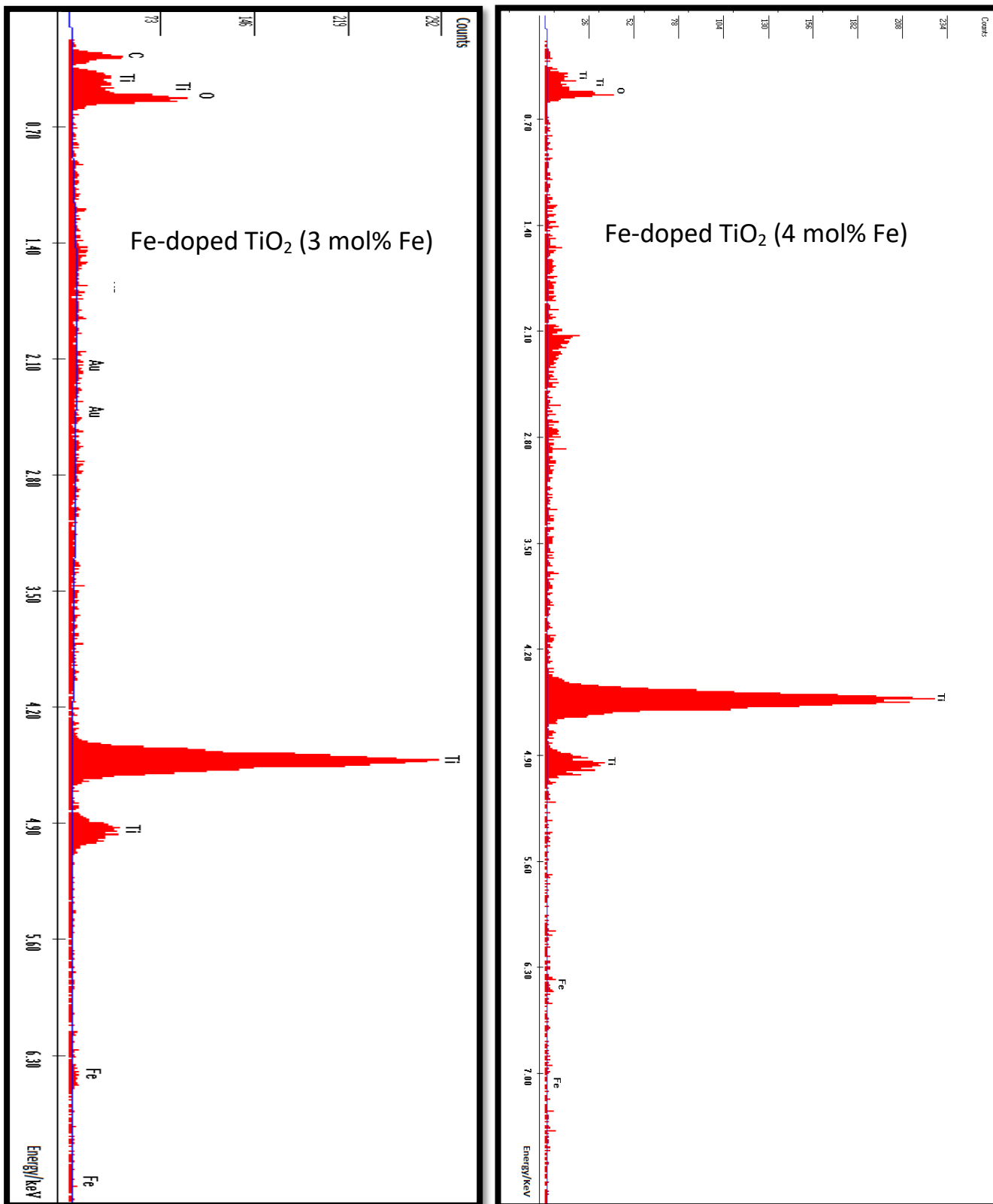
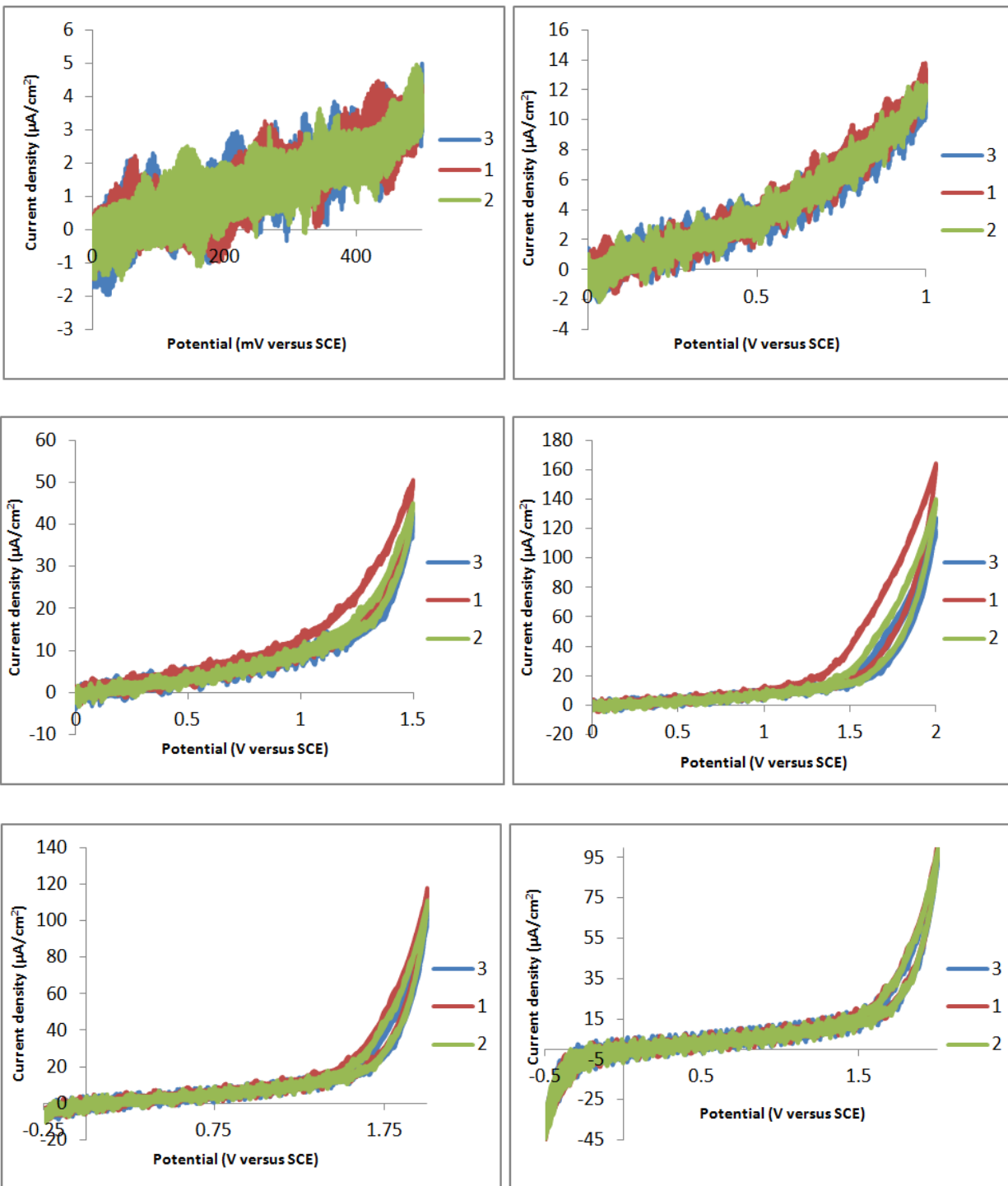


Figure (2-22). EDX experiment for all iron-doped TiO₂ nanomaterials.

2-8-Appendix 3: Cyclic voltammetry experiment for iron-doped TiO₂ (5 mol% Fe). Each experiment contains three consecutive cycles



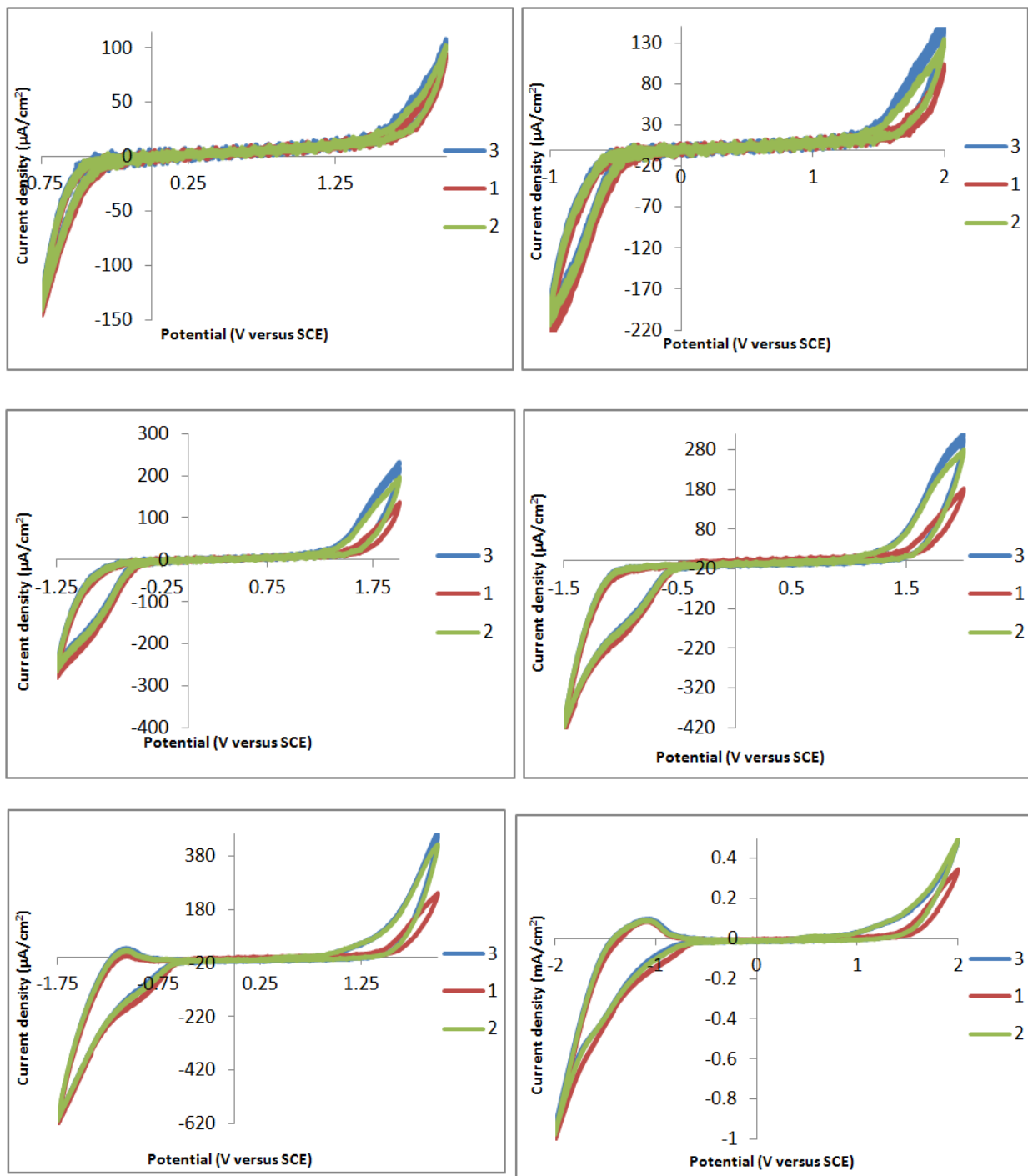


Figure (2-23). Cyclic voltammetry experiment for iron-doped TiO₂ (5 mol% Fe). Each experiment contains three consecutive cycles.

Chapter 3: Confocal Raman Mapping

3-1-Introduction

In this chapter, the details about Raman mapping experiment from the literature are described, followed by a discussion of the outcomes of the Raman mapping experiments on pure and iron-doped titanium dioxide as well as the commercial P25 TiO₂. Finally, Raman imaging results of two carboxyl-anchoring dyes, N3 and Z907, chemisorbed on the surface of pure and iron-doped TiO₂ are presented and discussed.

Confocal Raman microscopy is a combination of confocal microscopy and Raman spectroscopy. In a typical confocal microscope, a point-like light source and a pinhole located in front of the detector are employed to exclude out-of-focus signals (Figure (3-1)) [1]. The name "confocal" arises from this specific instrument configuration. In comparison to normal wide-field microscopes, the optical resolution of confocal microscopes is higher, since the light is collected from an area which is very close to the confocal plane. The minimum achievable thickness of confocal plane is a function of the numerical aperture, wavelength of excitation laser, pinhole size and magnification of the objective lens. Combining a sensitive Raman spectrometer with a confocal microscope gives high resolution Raman images that are used for obtaining the relative distribution of different components of a material.

A schematic diagram of the WITec confocal Raman microscope (alpha 300 R+) is shown below. Optical fiber is used to transmit the laser beam from a laser source to the microscope and from the microscope to the detector. A scan table is equipped with motors to move the sample while scanning with a laser Raman beam.

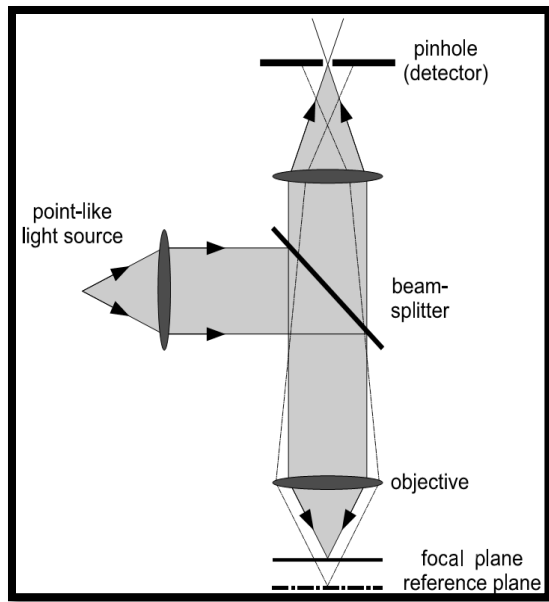


Figure (3-1). Schematic diagram of a typical confocal microscope. Reprinted by permission from Springer Nature: reference [1]. Copyright © 2010.

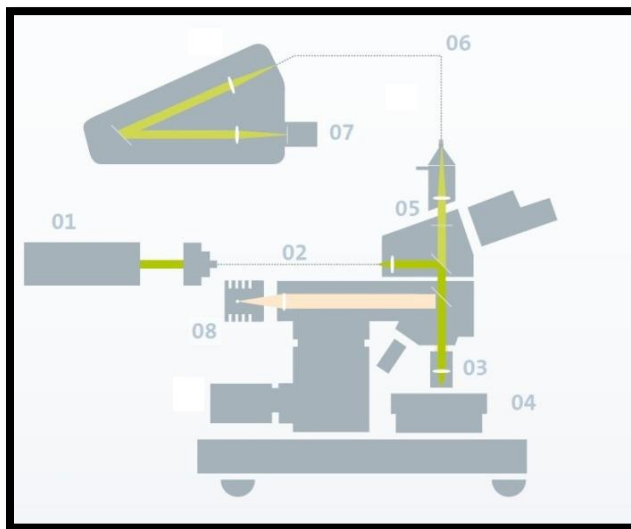


Figure (3-2). Schematic diagram of WITec confocal Raman microscope (alpha 300 R+): (01) Excitation laser (02) Optical fiber (03) Objectives (04) Scan table and/or stepper motor (05) Filter set (06) Optical fiber (07) CCD detector (08) White-light illumination [2].

3-2-Raman imaging of pure and iron-doped titanium dioxide nanomaterials

3-2-1-Experimental

The first step in the thin film sample preparation is to obtain a homogenous dispersion of each TiO₂ sample. Approximately, 1 g of TiO₂ is weighed and 1.5 mL of deionized water (Millipore, Milli-Q gradient 10) is added gradually followed by addition of 0.06 mL of Acetyl-acetone (Fluka, 99.5%). Then, the resulting paste is stirred for ca. 30 min. and sonicated in an ultrasound bath for another ca. 30 min. The mixture is then stirred for the rest of the day. This stirring/sonicating process (30 min. each) is repeated three times per day for three days. Then, the mixture is gradually diluted with 2 mL of deionized water. The same stirring/sonicating process is applied to obtain a suspension for two more days. Finally, 0.06 mL of Triton X-100 (Sigma-Aldrich) is added and the final suspension is stirred for one day.

Thereafter, titanium dioxide thin films are deposited on the glass using the doctor blade method. Then, they are dried on the hotplate following by calcination at 450 °C. Confocal Raman spectroscopy is employed to identify the distribution of anatase and brookite phases on the surface of the thin films for both pure and iron-doped titanium dioxide samples. This technique is carried out by WITec confocal Raman microscope (alpha 300 R+) using a laser excitation wavelength of 532 nm. The images are recorded from several areas of thin films with the dimension of 10 μm × 10 μm. The image is obtained by scanning across a straight lines collecting 100 points on each line. In other words, each pixel on the image has a dimension of 0.1 μm × 0.1 μm. The diameter of the laser beam as well as resolution of the mechanical parts controlling the movement of sample stage from one point to the next are the two factors controlling the size of the pixels.

All experiments were carried out in WITec GmbH located in Ulm, Germany under the supervision of Dr. Elena Bailo. For data analysis, a free software (WITec Project 4.0) was provided by WITec GmbH.

3-2-2-Results and discussion

3-2-2-1-Raman imaging of synthesized pure and iron-doped titanium dioxides: One of the most important structural characteristics of materials is their content and distribution pattern of various polymorphs of the same chemical formula. Based on the synthesis route, the distribution of the polymorphs could be uniform or non-uniform. In this work, according to our XRD data, only one iron-doped TiO₂ samples contained the brookite and the anatase phases while all other synthesized pure and iron-doped titanium dioxides contained only the anatase phase as determined using XRD.

If we wish to generate a Raman image from TiO₂ samples containing both anatase and brookite phases, the Raman spectra for these phases have to be examined carefully. The Raman spectra for pure anatase and pure brookite are shown in Figure (3-3) [3]. To generate accurate and meaningful Raman images, one peak from each phase should be considered with no, or at least minimum, overlap between them. Based on these criteria, the brookite peak at ca. 247 cm⁻¹ is a good candidate. It is relatively strong and has no overlap with any peak at the same wavenumber in the anatase Raman spectrum. In the case of the anatase phase, the peak at ca. 515 cm⁻¹ is the best candidate for Raman imaging. The other anatase peaks have significant overlaps with other brookite peaks.

As a result, the peaks at 515 cm⁻¹ and 247 cm⁻¹ are utilized to identify anatase and brookite, respectively, for the imaging Raman measurements. The average Raman spectrum including peak assignments of iron-doped titanium dioxide containing 0.7 mol.% Fe is shown in Figure (3-4). The average spectrum is obtained from the sum of all Raman spectra acquired over the whole image sampling area and divided by the number of pixels (equal to 10,000 pixels for our experiment). The XRD data shows that this particular sample contains 11.75% of the brookite phase and 88.25% of the anatase phase. Based on this information, we can set the average intensity of the brookite peak in the average Raman spectrum to be equal to 11.75% brookite. This will be the reference point for the color scale used in the Raman image.

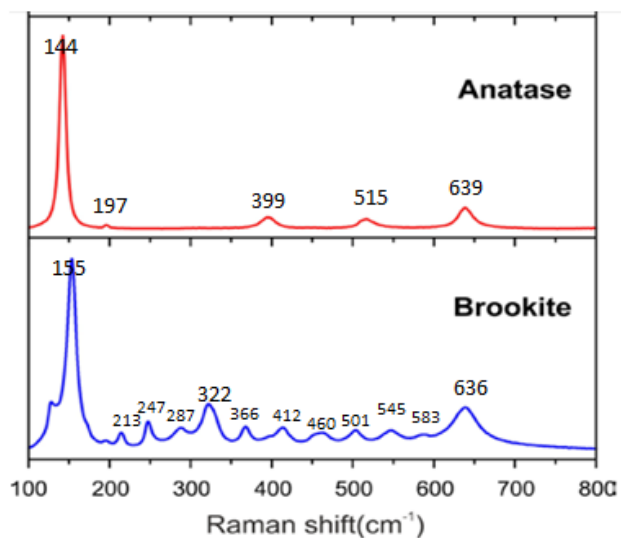


Figure (3-3). Raman spectra of (a) brookite TiO₂ (b) anatase TiO₂. Republished from open access reference [3].© 2017, Monai M.; Montini T.; Fornasiero P.; *Catalysts*, 2017, 7, 304, <https://www.mdpi.com/2073-4344/7/10/304>.

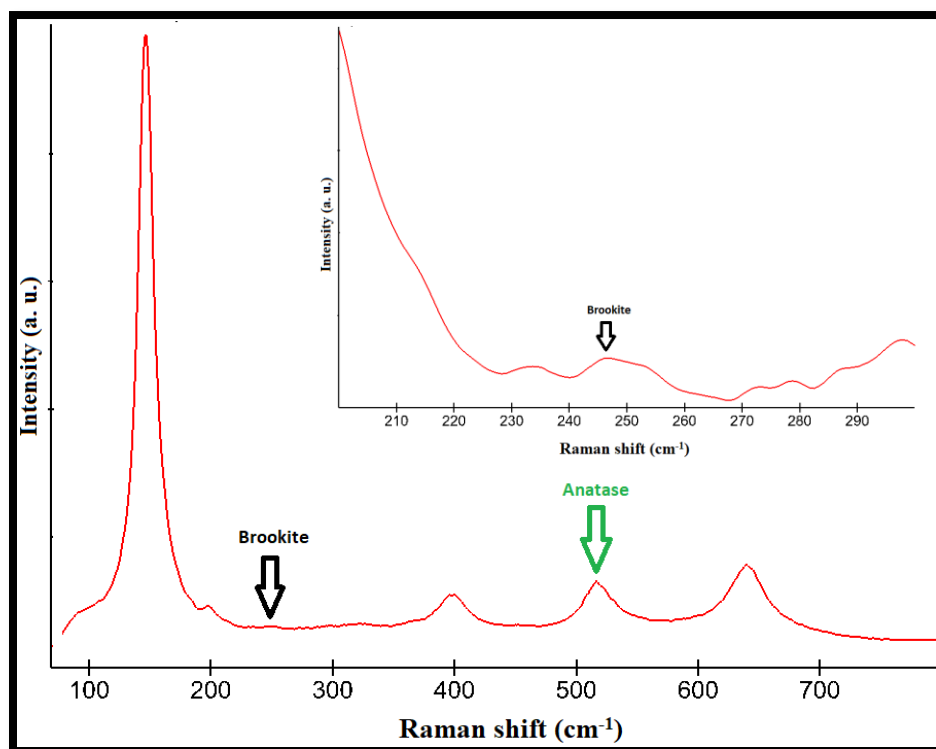
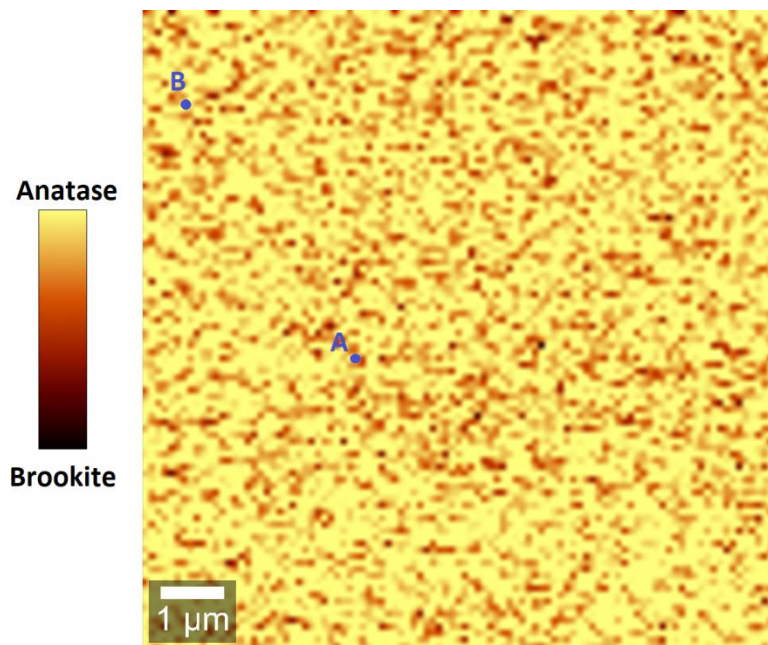
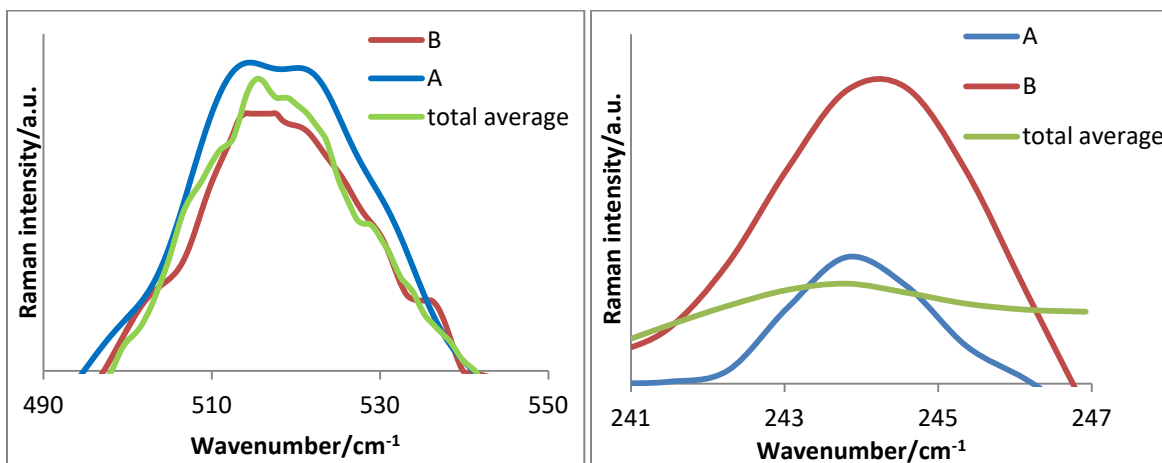


Figure (3-4). The peaks assigned for anatase and brookite in Raman spectrum of iron-doped titanium dioxide (0.7 mol.% Fe) containing 11.75% brookite phase in order to perform Raman imaging.

Figure (3-5) demonstrates the Raman mapping for our prepared iron-doped titanium dioxide (0.7 mol.% Fe). The lighter color areas in this image indicate a higher percentage of anatase phase. It should be noted that the lightest point on the image is very close to 100% anatase and the darkest point is about 40% brookite and 60% anatase (see discussion below related to sources of errors). This applies to Figures (3-5) and (3-7). As expected, the areas that show a higher amount of anatase contain lower amount of brookite. We can see that brookite can be found mostly as agglomerates in the anatase phase. Moreover, the expanded normal Raman spectra at point A (rich in anatase) and point B (rich in brookite) in Figure (3-5a) for the peaks assigned to anatase and brookite are depicted in Figures (3-5b) and (3-5c), respectively. For comparison purpose, the total average spectrum of the whole mapped area is also shown in Figures (3-5b) and (3-5c) as green lines. As it is expected, the intensity of the peak assigned to anatase is higher in point A than point B and the intensity of the peak attributed to brookite is higher in point B than point A. The intensity of total average spectrum of the whole imaged area can be correlated to values obtained by XRD. In other words, we can assume that the intensity of the total average spectrum for the anatase and brookite peaks are representative of their percentages in the sample, which are 88.25% and 11.75%, respectively. Based on this assumption, in the anatase case (Figure 3-5b), the intensity of total average spectrum lies between the ones for point A and point B. So, the amount of the anatase is estimated to be 91.6% and 80.4%, respectively. However, in case of the brookite peak (Figure 3-5c), the average intensity value is lower than the ones for both point A and point B. In this case, the estimated values for the brookite percentages at points A and B are 14.9% and 34.4%, respectively. It is expected that the summation of estimated percentages of anatase and brookite for each point does not exceed 100%, which is not true here. This might be due to small shifts observed in the maximum of the brookite peak (Figure 3-5c) and small variations in the spectrum baseline, which cannot be accounted for easily. To investigate these effects further, the Raman spectra for multiple points in the generated Raman image are selected. The obtained results are demonstrated in Figure (3-6), that shows the extent of the shift. Consequently, the amount of the brookite shown in the Raman images might be underestimated or overestimated, because only a fixed range of wavenumber values can be selected to determine the maximum Raman intensity when an image is generated.



(a)



(b)

(c)

Figure (3-5). (a) Raman mapping of iron-doped titanium dioxide (0.7 mol.% Fe). The darker areas are richer in anatase and lighter areas are richer in brookite (b) The expanded Raman spectra of point A, point B and total average spectrum of the whole mapped area at ca. 515 cm⁻¹ representing anatase phase (c) The expanded Raman spectra of of point A, point B and total average spectrum of the whole mapped area at ca. 244 cm⁻¹ representing anatase phase.

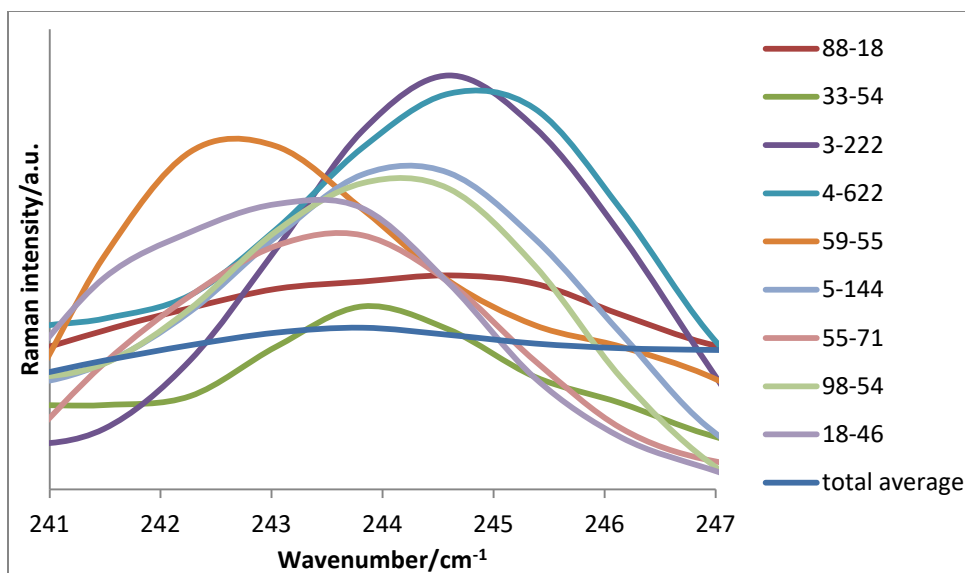


Figure (3-6). The expanded Raman spectra of multiple points in the Raman image from Figure (3-5a) and total average spectrum of the whole mapped area at ca. 244 cm^{-1} representing anatase phase. The numbers used to label each point are the x and y position of each used pixel from the image.

In the same way, the Raman image of iron-doped TiO_2 with 0.9 mol.% iron is recorded (Figure (3-7)). Based on the XRD, this sample contains 100% anatase. There is no evidence of the existence of any other phases, such as brookite from the XRD data. However, Raman imaging is able to detect brookite in this sample. Figure (3-8) shows the expanded average Raman spectra taken from the imaged area for both iron-doped TiO_2 nanomaterials with 0.7 and 0.9 mol% iron. As can be observed, the intensity of brookite peak at 247 cm^{-1} is higher for iron-doped TiO_2 (0.7 mol% iron) compared to the one with 0.9 mol% iron. Since, based on the XRD results, the former sample has 11.75% brookite, the sample containing 0.9 mol% iron would be expected to contain less brookite. Hence, Raman spectroscopy is a more sensitive analytical technique and helped us detect a small amount of brookite phase. Also, the Raman imaging for iron-doped TiO_2 with 0.7 mol% iron and with 0.9 mol% iron showed that addition of more iron to titanium dioxide enhanced the dispersion of the brookite phase in the sample leading to a more homogenous mixture of the two phases.

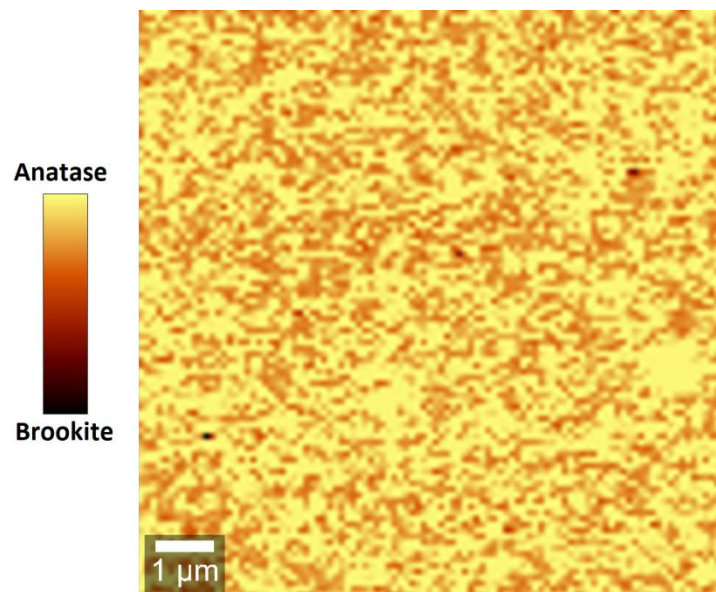


Figure (3-7). Raman mapping of iron-doped titanium dioxide (0.9 mol.% Fe). The lighter areas are richer in anatase and the darker areas are richer in brookite.

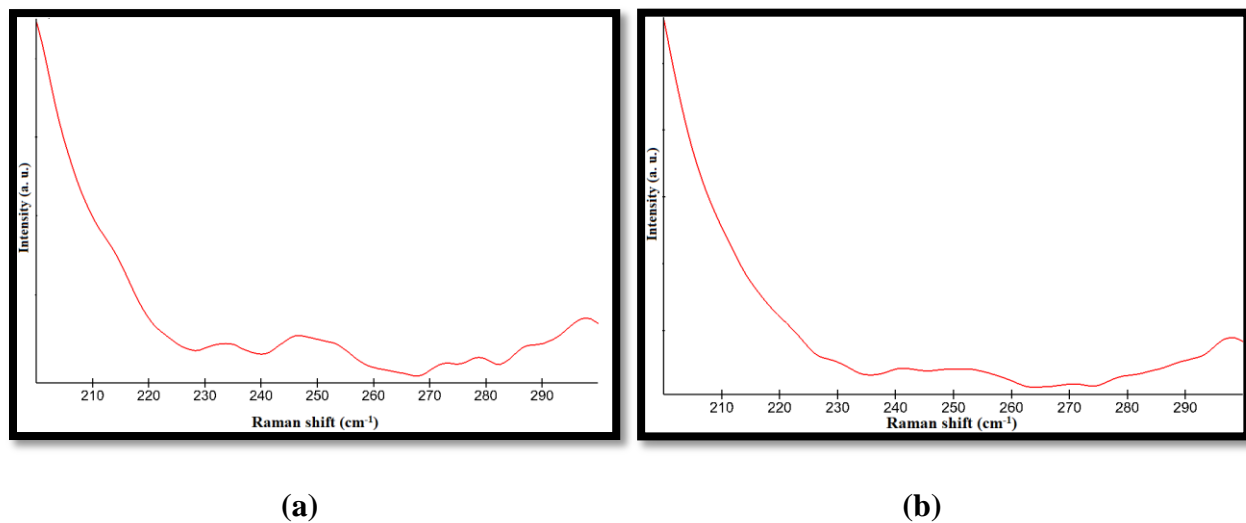


Figure (3-8). Average Raman spectra of the imaged area for (a) iron-doped TiO_2 (0.7% mol% iron) containing 11.75% brookite phase based on the XRD results (b) iron-doped TiO_2 (0.9 mol% iron) containing no brookite based on the XRD results.

In summary, the collected images are the first report of Raman imaging of iron-doped titanium dioxide samples and in a broader view, the first reported Raman imaging of metal-doped TiO_2 semiconductors. Although, based on the XRD patterns, there is no evidence of existence of

brookite phase in any of our samples except iron-doped TiO_2 (0.7 mol% Fe), Raman imaging showed the existence of brookite in our iron-doped TiO_2 samples and also the effect of iron on the distribution pattern of the anatase and brookite polymorphs in the sample. By addition of iron to titanium dioxide structure, the dispersion of brookite phase in the anatase is enhanced.

3-2-2-2-Raman imaging of commercial Aeroxide P25: Aeroxide P25 is a commercial titanium dioxide product from Degussa[®], which has been extensively applied in dye-sensitized solar cells and also photocatalytic systems [4-7], was also studied using the Raman imaging technique. It is composed of ca. 80% anatase and 20% rutile according to XRD studies [8-9]. To obtain accurate Raman imaging the peaks at 516 cm^{-1} and 445 cm^{-1} were selected as representative peaks for anatase and rutile phases, respectively [10]. As demonstrated in Figure (3-9), these two peaks do not overlap with each other in the Raman spectrum of TiO_2 . Therefore, they can be successfully employed in Raman imaging.

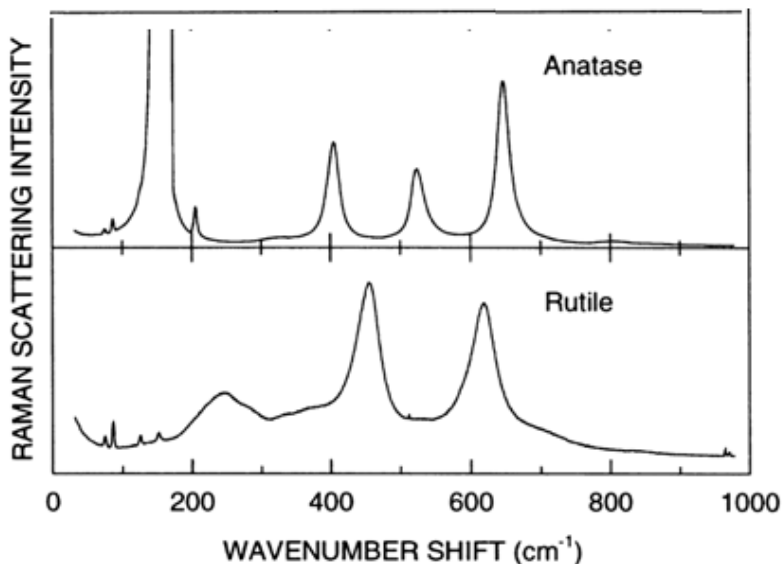


Figure (3-9). Raman spectra of pure anatase TiO_2 and pure rutile TiO_2 . Reprinted from reference [10] , Copyright © 2000, With permission from Elsevier.

The average Raman spectrum from all the measurements used to generate the image of the P25 sample is shown in Figure (3-10) and the peaks for the rutile and anatase phases are labeled on the spectrum.

Figure (3-11) shows the Raman image that resulted from the analysis of the P25 sample. Based on the defined color codes, the intensity of brown color is directly proportional to the amount of anatase that exists in that specific area. The image indicates that the rutile phase is mixed in some areas with anatase one. Although, in some small areas, mostly the rutile phase is observed, these areas display localized white spots in the image. Figure (3-11b) shows the expanded Raman spectra taken from point A and B plus the total average spectrum of the whole mapped area for comparison purposes. As displayed, the peak intensity at ca. 445 cm^{-1} as representative of rutile phase is significantly stronger at point B than point A, which means the amount of the rutile phase is enormously more in point B than point A. On the contrary, the signal intensity attributed to anatase phase, which is located at ca. 519 cm^{-1} , is stronger in point A than point B. However, the variation of signal intensities are not too intense like the rutile signal. That means although the dominant phase is anatase everywhere, rutile can be found as highly concentrated spots in the sample. As discussed before, based on the reported XRD studies, the amount of anatase and rutile in P25 sample is ca. 80% and 20%, respectively. These values can be correlated to the signal intensity of total average spectrum of the anatase and the rutile following by estimating the amount of the anatase and the rutile in point A and B. The amount of the anatase in point A and B is estimated 83.9% and 75.2%, respectively. In case of the rutile phase, the estimated values are 12.7% and 80.5% for point A and B, respectively. The amount of the rutile in point B is significantly higher than the one in point A. That proves that rutile is located as very concentrated areas in the anatase phase. The summation of the anatase and the rutile percentage for point A is close to 100%, which means that the relative estimation of the two phases at point A is fairly accurate. However, this summation for point B is considerably higher than 100% due to a large increase in the rutile peak intensity. If we consider only the anatase peak to estimate the amount of each phase, it can be said that at the darkest and brightest points in figure (3-11a), the content of the anatase is ca. 80% (and consequently the amount of rutile phase is ca. 20%). The rutile rich area appear circular and are below one micron in diameter.

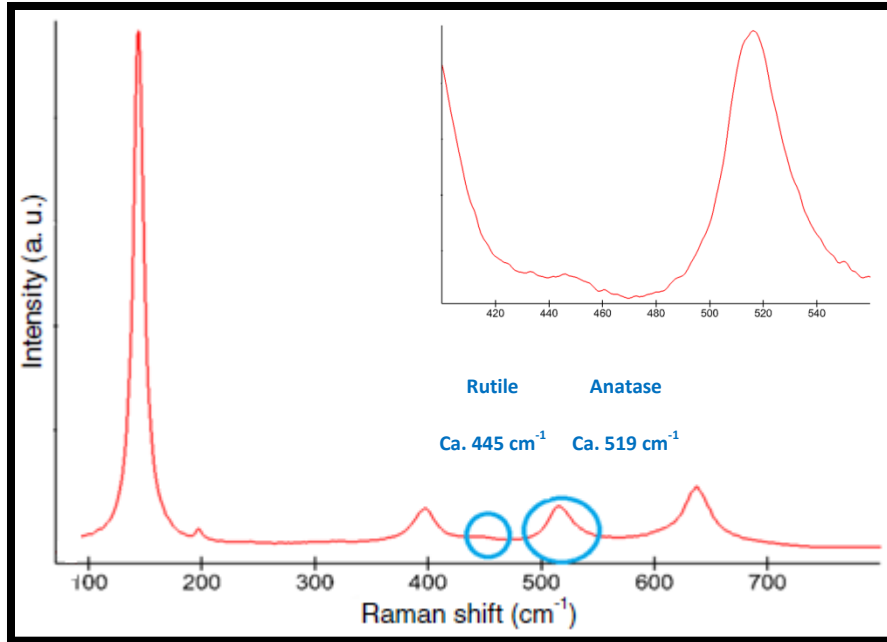
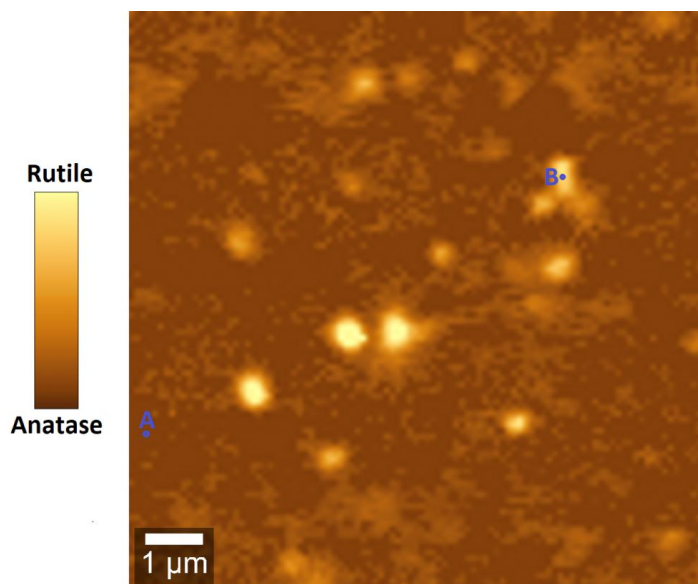


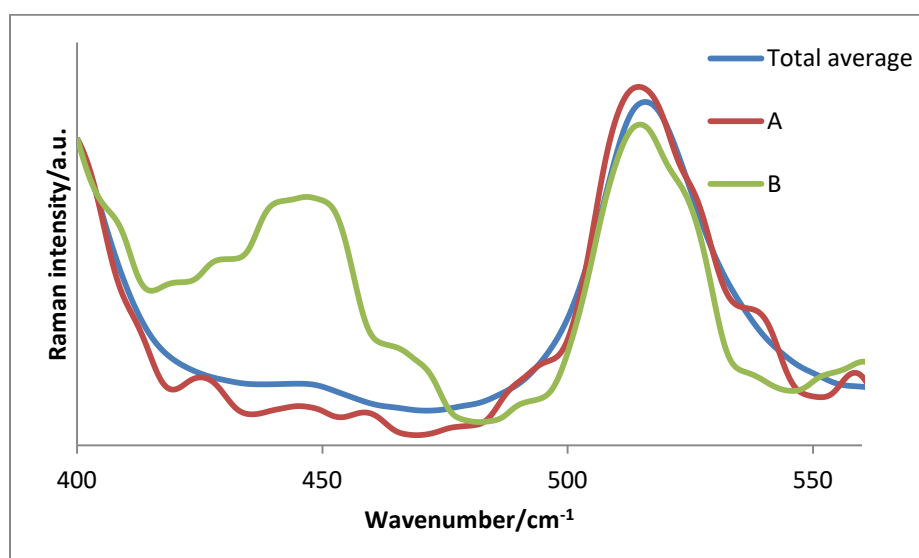
Figure (3-10). The peaks attributed to anatase and rutile in average Raman spectrum of the whole mapped Aerioxide P25 for performing Raman imaging.

In terms of anatase and brookite phase dispersion in P25, the results match that of previous works [11-12]. Datye *et al.* discovered that P25 is composed of bigger individual rutile nanoparticles dispersed in smaller anatase nanoparticles [11]. Moreover, Ohno *et al.* proved that rutile and anatase phases coexist as agglomerates in P25. Under a particular photocatalytic process, the agglomerates can be decomposed into anatase and rutile nanoparticles, which is claimed to be the key for high photocatalytic activity of the P25 powder [12].

As mentioned earlier, Raman imaging of P25 was reported only one time [13]. The image obtained from our work have a close similarity to what was achieved by Parussulo *et al.* (chapter 1; Figure (1-11)) [13]. But the resolution and quality of our image is higher.



(a)



(b)

Figure (3-11). (a) Raman image of Aeroxide P25 (c) The expanded Raman spectra taken from point A and point B plus total average spectrum of the whole imaged area.

3-3-Raman imaging of dye-adsorbed TiO₂ films

In the past, The Morin's Research group studied the adsorption of dyes on the surface of TiO₂ in details including the dye-sensitized TiO₂ efficiency at solar energy conversion [4,14]. Hence, Raman imaging of the dye-sensitized TiO₂ surface was of interest to us as it provides a map of the dye adsorption on the TiO₂ surface as well as the surface -OH groups available for binding in the absence of the dye.

Dyes employed in dye-sensitization of TiO₂ typically have one or several carboxyl group available for binding to the OH groups on the surface of TiO₂ that are known to be present on its surface [15-17]. For example, the N3 (Cis-bis(isothiocyanato)bis(2,2'-bipyridyl-4,4'-dicarboxylato)ruthenium(II)) dye, which is well known as one of the first highly performing dyes for solar energy conversion [7,18-19], possesses four carboxyl functional group as demonstrated in Figure (3-12). Similarly, Di-tetrabutylammoniumcis-bis(isothiocyanato)bis(2,2'-bipyridyl-4,4'-dicarboxylato) ruthenium(II), which is a crystalline black powder known as Z907, is a ruthenium based high performance dye as photo-sensitizer with the similar chemical structure to N3 (Figure (3-13)). It has been employed widely as sensitizer in dye-sensitized solar cells [20-23]. In comparison to N3, Z907 possesses hydrophobic character due to its C9 long chains and also two anchoring carboxyl group.

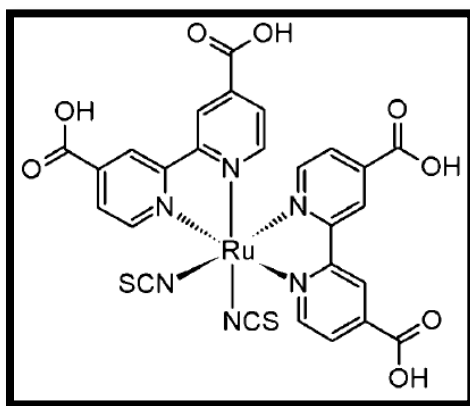


Figure (3-12). The structure of N3 dye. Reprinted by permission from Springer Nature: reference [24]. Copyright © 2013.

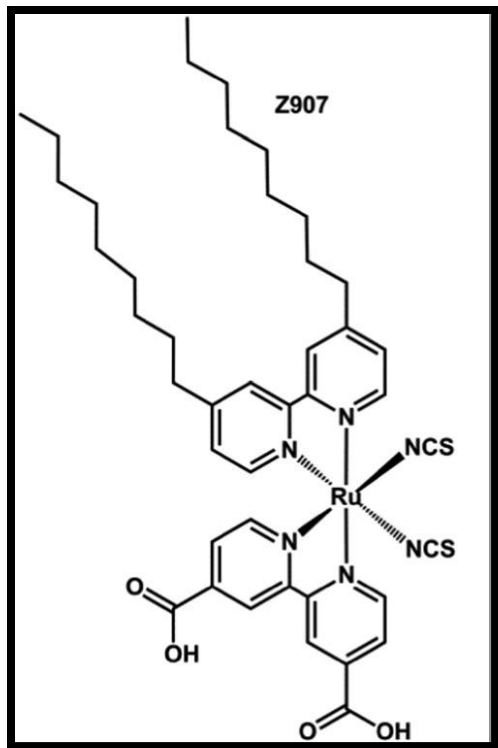


Figure (3-13). The chemical structure of Z907 dye. Republished with permission of ROYAL SOCIETY OF CHEMISTRY from reference [25], Copyright © 2013. Permission conveyed through Copyright Clearance Center, Inc.

3-3-1-Experimental

The N3 dye is purchased from Solaronix SA[®] and is used directly as received. N3 is dissolved in anhydrous Ethanol. The previously prepared pure or iron-doped TiO₂ thin films on glass are heated at ca. 100 °C in the oven to remove any water molecules from the surface in order to increase their dye adsorption. They are then dipped into the N3 dye solution while they are still hot. Then, they have been remained in the dye solution for 24 hours in a dark place. Finally, the films are rinsed abundantly with ethanol to remove physisorbed molecules as much as possible and then dried under an argon flux.

The Z907 dye is bought from Sigma-Aldrich[®] and it is dissolved in 1:1 volumetric mixture of acetonitrile and t-butanol solvents. The same procedure as N3 dye is used to adsorb Z907 on thin films of pure or iron-doped titanium dioxide.

In case of the performing Raman measurements on all samples covered with N3 or Z907 dye, a very low-power Raman laser should be employed, since the laser can easily burn the dye on the surface of the sample.

3-3-2-Results and discussion

3-3-2-1-N3 dye adsorbed on synthesized pure and iron-doped titanium dioxide: Raman spectroscopy has been carried out in various studies on both N3 dye and also N3 dye adsorbed on TiO_2 [26-28]. Figure (3-14) demonstrates the Raman spectra of pure titanium dioxide (anatase), pure N3 dye in solid state and N3 dye adsorbed on titanium dioxide [27]. The peaks at 1461 , 1528 and 1596 cm^{-1} are correlated to the stretching modes of bipyridyl groups of N3 [26].

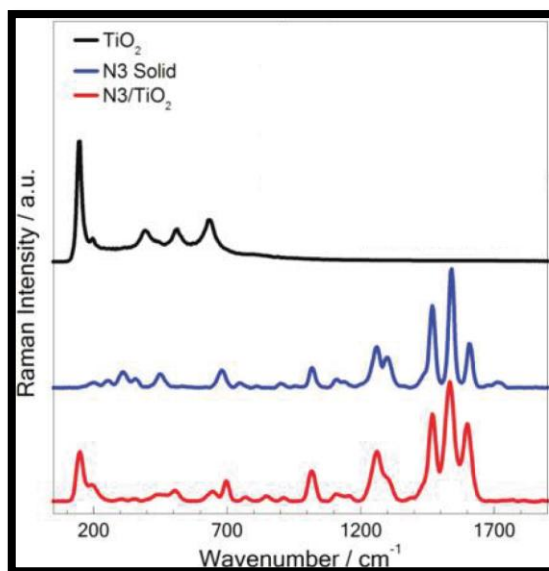


Figure (3-14). Raman spectra of pure titanium dioxide (anatase), pure N3 dye in solid state and N3 dye adsorbed on titanium dioxide. Reprinted with permission from reference [26],

Copyright © 2011, American Chemical Society.

The Raman spectrum of N3 dye adsorbed on titanium dioxide is a mixture of Raman spectra of both N3 and TiO_2 . Major Raman bands of anatase at 144 , 197 , 395 , 515 , and 638 cm^{-1} are found in Raman spectrum of pure TiO_2 as well [29].

Distribution of N3 dye on the surface of TiO_2 has a crucial impact on the sensitization efficiency of the dye. Raman mapping is able to provide valuable information in this regard. The average

Raman spectrum of the whole mapped area of our N3 dye adsorbed on the synthesized pure TiO₂ is very similar to the one discussed above from literature (Figure (3-15)). Two characteristic peaks at 145 cm⁻¹ and 1540 cm⁻¹ are chosen for titanium dioxide and N3 dye, respectively.

The Raman image of N3 adsorbed on TiO₂(2) (pure titanium dioxide) is shown in Figure (3-16). N3 covers most of the surface of the sample.

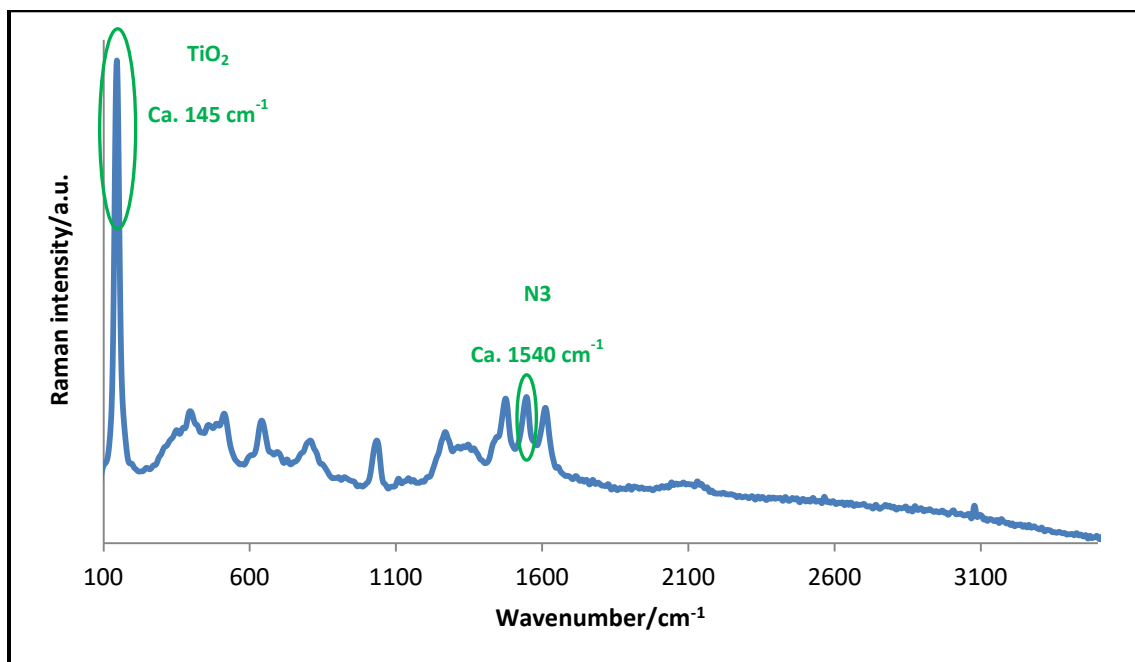


Figure (3-15). The peaks assigned for titanium dioxide and N3 dye in average Raman spectrum of N3 dye adsorbed on titanium dioxide taken from the whole mapped area.

Figure (3-17) displays the Raman image generated from another place on N3 adsorbed on TiO₂(2) (pure titanium dioxide). This image also illustrates a pattern similar to the one observed in the last figure. The experiment is implemented for the second time to make sure the data is reproducible.

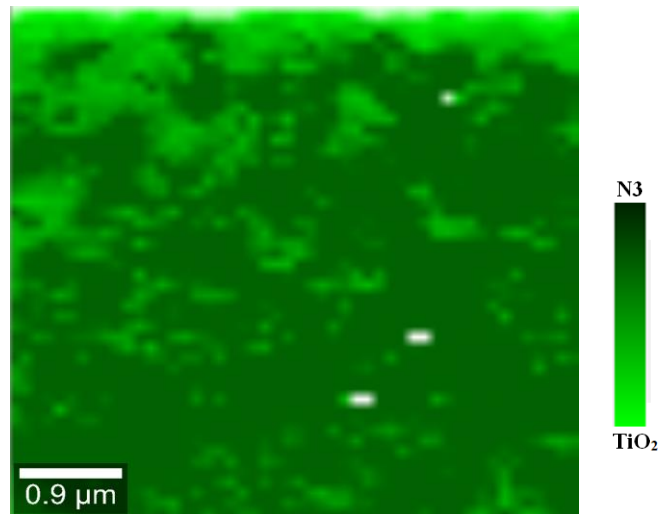


Figure (3-16). Raman image of N3 adsorbed on TiO₂(2) (pure titanium dioxide).

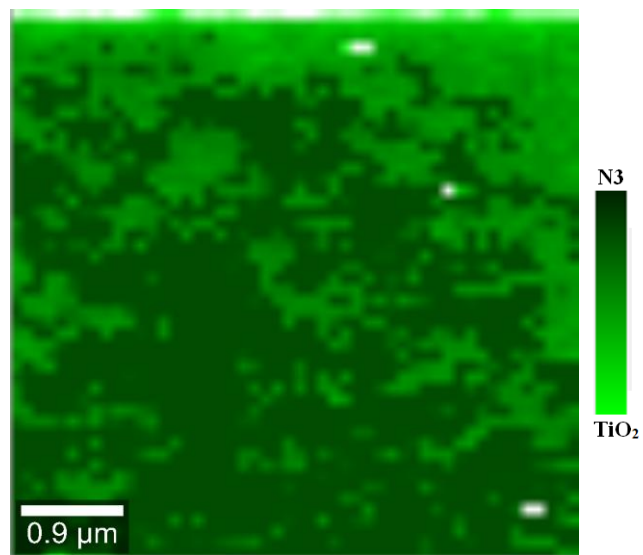


Figure (3-17). Raman image of another area of N3 adsorbed on TiO₂(2) (pure titanium dioxide).

The same type of Raman mapping is done on TiO₂(1) (pure titanium dioxide) and TiO₂(2). In terms of distribution of N3 on the surface of the sample, a pattern similar to TiO₂(2) is revealed (Figure (3-18)).

The effect of iron as dopant on the distribution pattern of N3 on the surface of titanium dioxide is studied by collecting the Raman mapping of iron-doped TiO_2 contains 0.9 mole% Fe as shown in Figure (3-19). N3 is adsorbed as efficiently as one pure titanium dioxide sample. There is no significant difference between the pure and iron-doped samples.

In summary, the Raman imaging of N3 dye adsorbed on synthesized pure and iron doped titanium dioxide is reported for the first time. The addition of iron as dopant does not have a significant influence on the adsorption pattern of N3 dye.

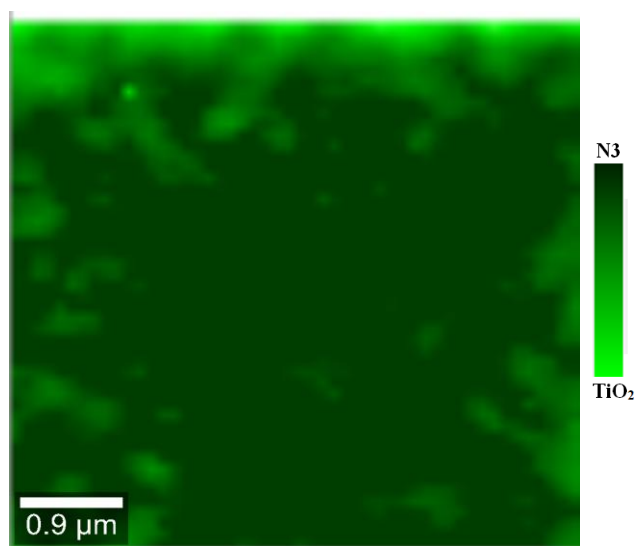


Figure (3-18). Raman image of N3 adsorbed on $\text{TiO}_2(1)$ (pure titanium dioxide).

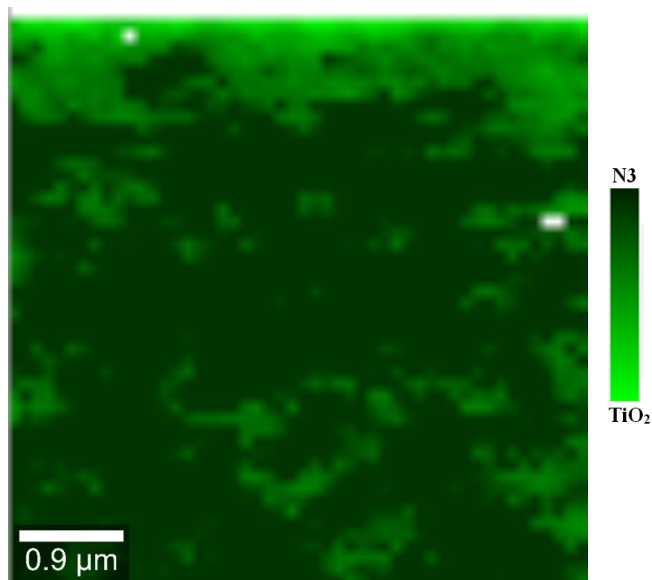


Figure (3-19). Raman image of N3 adsorbed on iron-doped titanium dioxide with 0.9 mole% Fe.

3-3-2-2-Z907 dye adsorbed on synthesized pure and iron-doped titanium dioxide:

The Raman spectra of both Z907 powder and Z907 adsorbed on TiO_2 shows the main vibrational structure of polypyridyl-ruthenium complexes is preserved (Figure (3-20)) [32]. The three intense bipyridine ring stretching modes at $1472\text{-}1613\text{ cm}^{-1}$ are analogous to the ones in the N3 Raman spectrum.

The same method as the one applied for imaging of N3 adsorbed on titanium dioxide is employed for Z907 adsorbed on TiO_2 . The peaks at 1540 cm^{-1} and 145 cm^{-1} are assigned in Raman imaging for Z907 and titanium dioxide, respectively (Figure (3-21)).

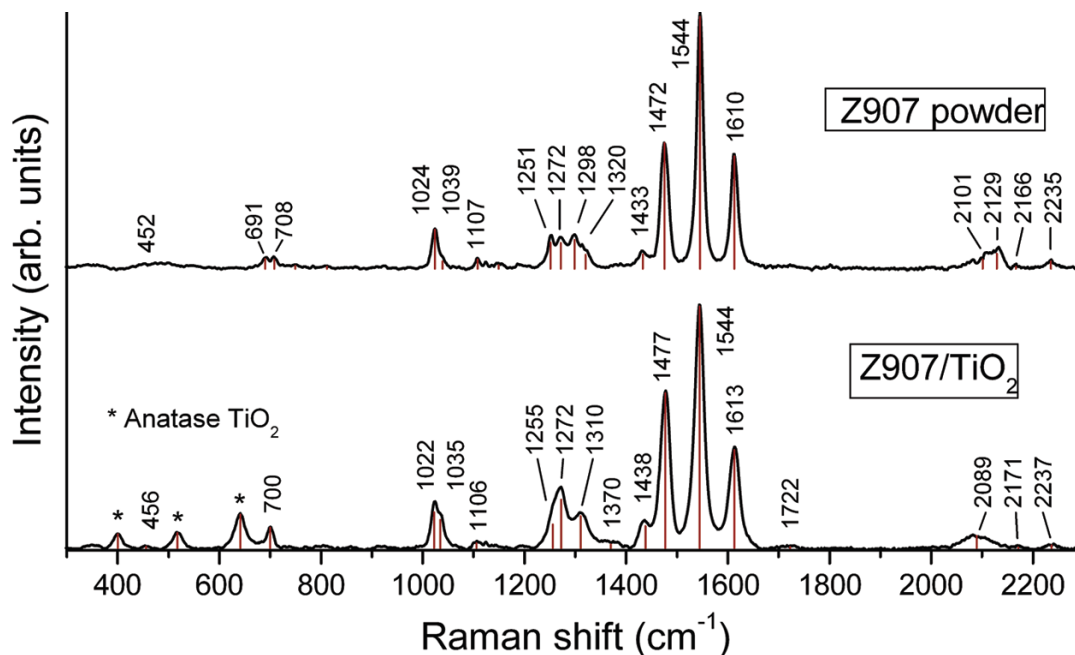


Figure (3-20). The Raman spectra of Z907 powder (top) and Z907 adsorbed on titanium dioxide. Reprinted with permission from reference [32], Copyright © 2009, American Chemical Society.

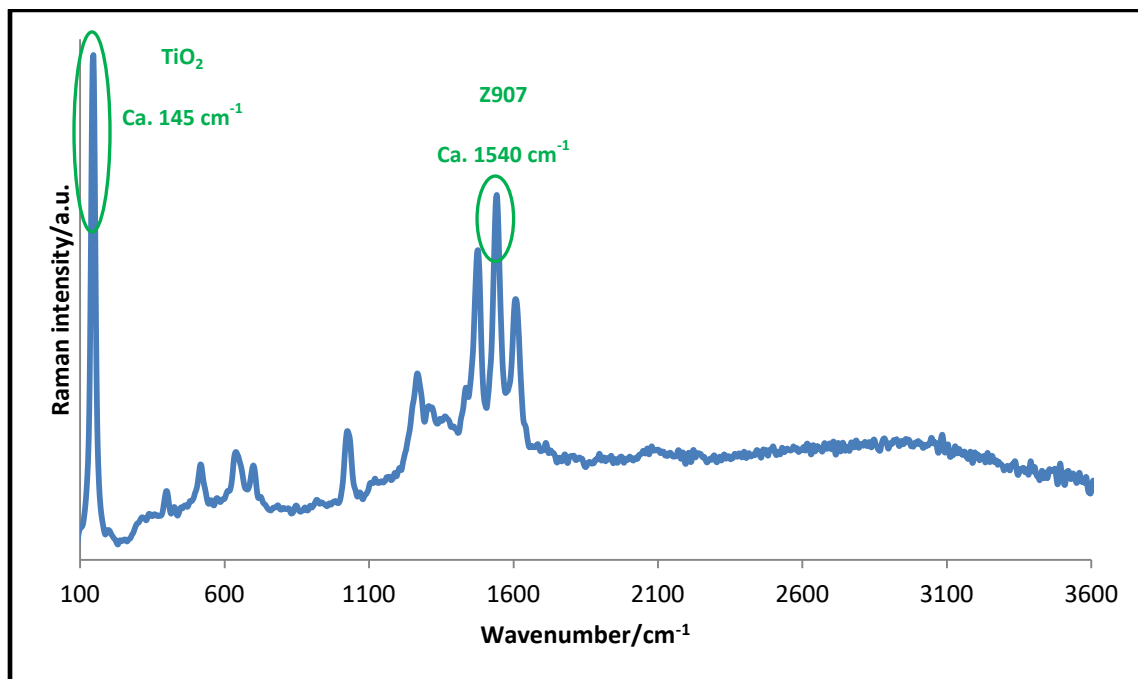


Figure (3-21). The peaks assigned for titanium dioxide and Z907 dye in average Raman spectrum of Z907 dye adsorbed on titanium dioxide taken from the whole mapped area.

The derived Raman images of Z907 adsorbed on TiO₂(1) and TiO₂(2) (pure titanium dioxides) point out an analogy between the distribution pattern of Z907 and N3 on the surface of pure titanium dioxide samples. But, Z907 covers a larger surface area of TiO₂ than N3 ((Figures (3-22) and (3-23)).

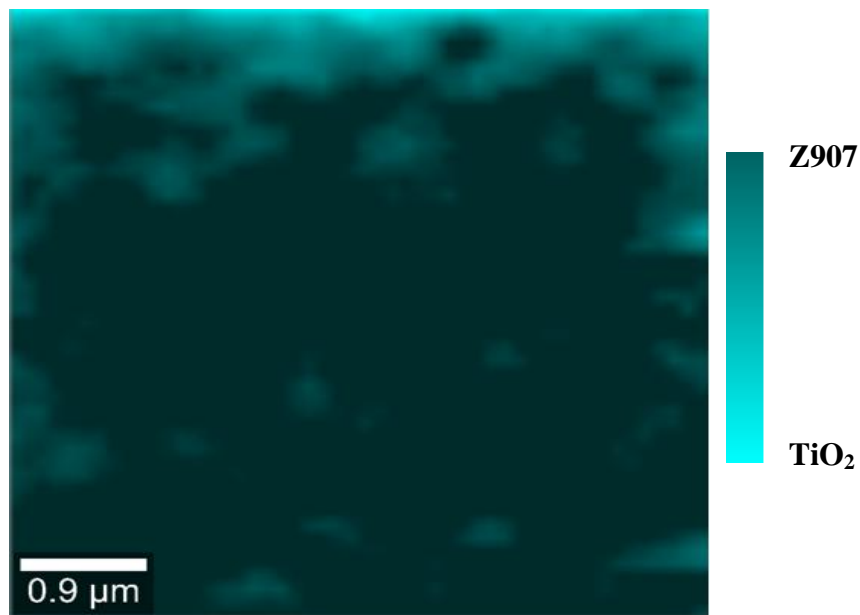


Figure (3-22). Raman image of Z907 adsorbed on TiO₂(1) (pure titanium dioxide).

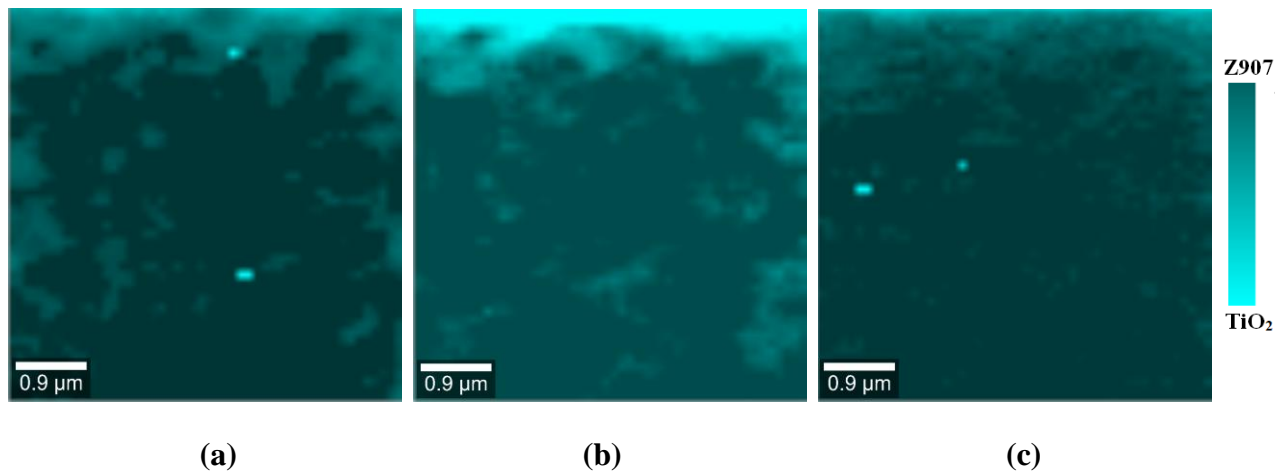


Figure (3-23). Raman images for (a) another spot for Z907 adsorbed on TiO₂(1) (pure titanium dioxide) (b) Z907 adsorbed on TiO₂(2) (pure titanium dioxide) (c) another spot for Z907 adsorbed on TiO₂(2) (pure titanium dioxide).

Finally, the Raman images of Z907 adsorbed on iron-doped TiO_2 with 0.7 mole% Fe from two different points are taken (Figure (3-24)). Addition of iron as dopant into the titanium dioxide matrix caused lower amount of Z907 adsorption on the surface of TiO_2 . However, compared to N3/TiO_2 samples, the distribution pattern of Z907 on iron doped TiO_2 is more continuous and a larger surface area is covered by the dye.

In summary, the Raman imaging of Z907 dye adsorbed on synthesized pure and iron doped titanium dioxide is reported for the first time. The addition of iron as dopant, can decrease the amount of Z907 dye adsorbed on the surface of TiO_2 .

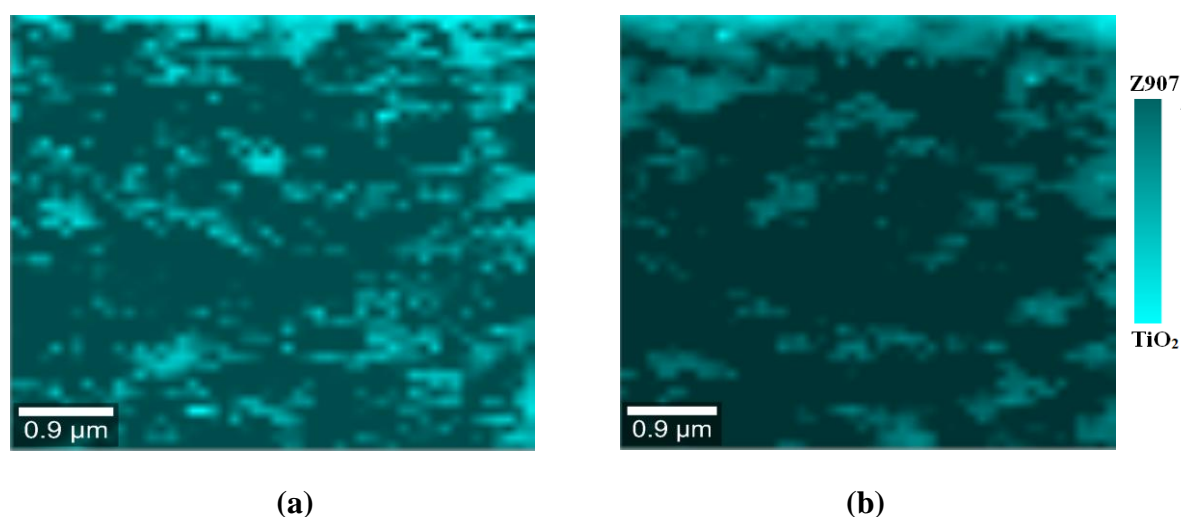


Figure (3-24). Raman images of (a) Z907 adsorbed on iron-doped titanium dioxide with 0.7 mole% Fe (b) another spot for Z907 adsorbed on it.

3-4-Conclusion

Raman mapping experiments have been carried out on pure and iron-doped titanium dioxide nanomaterials. Based on the XRD pattern, there was no evidence of having brookite phase in any of them except iron-doped TiO_2 (0.7 mol% Fe). But, Raman imaging proved the existence of brookite phase in these materials. In the case of pure titanium dioxide, the brookite phase was found as agglomerates distributed in between anatase phase. By addition of iron as dopant, the distribution of brookite phase in anatase becomes more homogeneous. Raman imaging of P25,

containing approximately 80% anatase and 20% rutile, shows rutile exists mostly as islands in between anatase phase.

Raman imaging on N3 dye adsorbed on titanium dioxide shows doping of titanium dioxide with iron does not have a significant influence on the distribution pattern of N3 on TiO₂. A similar study has been performed on Z907 dye adsorbed on TiO₂. In this case, doping of TiO₂ with iron decreases the amount of Z907 adsorbed on titanium dioxide.

3-5-References

- [1] Dieing T.; Hollrichter O.; Toporski J.; *Confocal Raman Microscopy*, Springer-Verlag, Berlin, Heidelberg, **2010**.
- [2] www.witec.de
- [3] Monai M.; Montini T.; Fornasiero P.; *Catalysts*, **2017**, 7, 304.
- [4] Sepehrifard A.; Chen S.; Stublla A.; Potvin P. G., Morin S.; *Electrochim. Acta*, **2013**, 87, 236.
- [5] Ma Y.; Wang X.; Jia Y.; Chen X.; Han H.; Li C.; *Chem. Rev.*, **2014**, 114, 9987.
- [6] Schneider J.; Matsuoka M.; Takeuchi M.; Zhang J.; Horiuchi Y.; Anpo M.; Bahnemann D. W.; *Chem. Rev.*, **2014**, 114, 9919.
- [7] Chen X.; Mao S. S.; *Chem. Rev.*, **2007**, 107, 2891.
- [8] Su. R.; Bechstein R.; Sjø L.; Vang R.T.; Sillassen M.; Esbjörnsson B.; Palmqvist A.; Besenbacher F.; *J. Phys. Chem. C* **2011**, 115, 24287.
- [9] Bakardjieva S.; Šubrt J.; Štengl V.; Dianez M. J.; Sayagues M. J.; *Appl. Catal. B-Environ.*, **2005**, 58, 193
- [10] Moret M. P.; Zallen R.; Vijay D. P.; Desu S. B.; *Thin Solid Films*, **2000**, 366, 8.
- [11] Datye A. K.; Riegel G.; Bolton J. R.; Huang M.; Prairie M. R. J.; *Solid State Chem.*, **1995**, 115, 236.
- [12] Ohno T.; Sarukawa K.; Tokieda K.; Matsumura M.; *J. Catal.*, **2001**, 203, 82.
- [13] André L. A. P.; Bonacin J. A.; Toma S. H.; Araki K.; Toma H. E.; *Langmuir*, **2009**, 25(19), 11269.
- [14] Sepehrifard A.; Kamino B. A.; Bender T. P.; Morin S.; *ACS Appl. Mater. Interfaces.*, **2012**, 4, 6211.
- [15] Nazeeruddin M. K.; Humphry-Baker R.; Liska P.; Grätzel M.; *J. Phys. Chem. B* **2003**, 107, 8981.
- [16] Galoppini E.; *Coordin. Chem. Rev.* **2004**, 248, 1283.

- [17] Mishra A.; Fischer M. K. R.; Bäuerle P.; *Angew. Chem. Int. Ed.* **2009**, 48, 2474.
- [18] Hagfeldt A.; Boschloo G.; Sun L.; Kloo L.; Pettersson H.; *Chem. Rev.*, **2010**, 110, 6595.
- [19] Bai Y.; Mora-Seró I.; De Angelis F.; Bisquert J.; Wang P.; *Chem. Rev.*, **2014**, 114, 10095.
- [20] Vougioukalakis G. C.; Stergiopoulos T.; Kontos A. G.; Pefkianakis E. K.; Papadopoulos K.; Falaras P.; *Dalton Trans.*, **2013**, 42, 6582.
- [21] Wang P.; Zakeeruddin S. M.; Moser J. E.; Zakeeruddin M. K.; Sekiguchi T.; Grätzel M.; *Nat. Mater.* **2003**, 2, 402.
- [22] Wang P.; Zakeeruddin S. M.; Comte P.; Charvet R.; Humphry-Baker R.; Grätzel M.; *J. Phys. Chem. B* **2003**, 107, 14336.
- [23] Rahman M. Y. A.; Umar A. A.; Roza L.; *Russ. J. Electrochem.* **2014**, 50 (11), 1072.
- [24] de Souza J..S.; de Andrade L.O.M.; Polo A.S. *Nanomaterials for Solar Energy Conversion: Dye-Sensitized Solar Cells Based on Ruthenium (II) Tris-Heteroleptic Compounds or Natural Dyes*. In: de Souza F., Leite E. (eds) *Nanoenergy.*, **2013**, Springer, Berlin, Heidelberg.
- [25] Liu Y.; Jennings J. R.; Wang X.; Wang Q.; *Phys. Chem. Chem. Phys.*, **2013**, 15, 6170.
- [26] Jang, S; Vittal R.; Lee J.; Jeong N.; Kim K.; *Chem. Commun.*, **2006**, 103, 103.
- [27] Parussulo A. L. A.; Huila M. F. G.; Araki K.; Toma H. E.; *Langmuir*, **2011**, 27, 9094.
- [28] Wang H.; Chen L.; Su W.; Chung J.; Hwang B.; *J. Phys. Chem. C* **2010**, 114, 3185.
- [29] Lu H.; Zhao J.; Li L.; Gong L.; Zheng J.; Zhang L.; Wang Z.; Zhang J.; Zhu Z.; *Energy Environ. Sci.* **2011**, 4, 3384.
- [30] Lee K. E.; Gomez M. A.; Elouatik S.; Demopoulos G. P.; *Langmuir*, **2010**, 26(12), 9575.
- [31] Lee K. E.; Gomez M. A.; Elouatik S.; Demopoulos G. P.; *ECS Trans.*, **2010**, 28 (10), 1.
- [32] Likodimos V.; Stergiopoulos T.; Falaras P.; Harikisun R.; Desilvestro J.; Tulloch G.; *J. Phys. Chem. C* **2009**, 113, 9412.

Chapter 4: Photodegradation Properties of Iron-doped Titanium Dioxide Nanomaterials

4-1-Introduction

As outlined in the introduction, TiO₂ nanomaterials are particularly well suited as catalysts for the photodegradation of organic pollutants in water using sunlight as a source of power. In this chapter, a detailed study of the photocatalytic activity of our pure and iron-doped titanium dioxide nanomaterials is presented. The photodegradation of methylene blue has been studied as a model reaction to quantify the photocatalytic activity of all our materials under simulated sunlight for reaction times of up to 3 hours. This approach mirrors that of other similar studies reported in the scientific literature and allows for direct comparison with the performance of other materials. Details about our methodology including materials, instrumentation and photodegradation experimental setup is provided below. In the results and discussion section, the photodegradation is presented in detail together with several key control experiments. Thereafter, the effect of pH on this reaction and its correlation to the point of zero charge (PZC) of the studied materials are explained.

4-2-Experimental

4-2-1-Materials: Methylene blue (Reagent grade, 92%) is purchased from Fisher Scientific (Ottawa, ON). Ultra-pure water is used to prepare all solutions as well as for rinsing the glassware. All pure and iron-doped titanium dioxides (0.5, 0.7, 2.1, 3 and 4 mol% iron) were prepared before in our lab at York university and used directly as they were synthesized.

4-2-2-Instrumentation: PET Solar Light Simulator (Photo Emission Tech Inc. (Camarillo, CA)) is employed for illumination of samples. UV-Vis Spectrophotometer (Agilent Technologies (Mississauga, ON)) is used to determine the concentration of methylene blue. Ultra-sonicator (Laval Lab Inc. (Laval, QB)) is applied for sonication and dispersion of TiO₂ powder in the

solution of methylene blue. For effective separation of catalyst powder from the reaction mixture, samples are centrifuged.

4-2-3-Photodegradation experimental setup: The photodegradation efficiency of titanium dioxides with various iron concentrations as dopant are tested by using a 4 mg/l methylene blue solution as a model pollutant in water under the irradiation of a simulated solar light. The photodegradation experiment for each titanium dioxide sample is repeated three times under the same condition. 2 mg/l of TiO₂ sample is sonicated in methylene blue solution in order to disperse the catalyst powder properly before exposing them to the light. Thereafter, the obtained suspension is stirred for 30 minutes in the dark to reach the adsorption equilibrium. Stirring is continued during the light illumination. The measured intensity of incident light (AM 1.5) is about 36 mW/cm². The overall irradiation time is 3 hours. Every 30 minutes, a small aliquot of the reaction mixture is collected to trace the reaction progress. The collected aliquots are centrifuged at 13000 rpm for 20 minutes. Then, the remaining methylene blue concentration is determined by UV-Vis spectrophotometer. All measurements are performed at 663 nm as maximum absorption peak for methylene blue.

4-3-Results and Discussion

The correlation between methylene blue concentration and the absorption obtained by UV-Vis instrument is determined by measurement of the absorption of methylene blue standard solutions with known concentrations followed by drawing the calibration curve as demonstrated in Figure (4-1).

The efficiency of pure and iron-doped titanium dioxides (0.5, 0.7, 2.1, 3 and 4 mol% iron) is evaluated by degradation of methylene blue under irradiation of simulated sunlight. The achieved results are depicted in Figure (4-2).

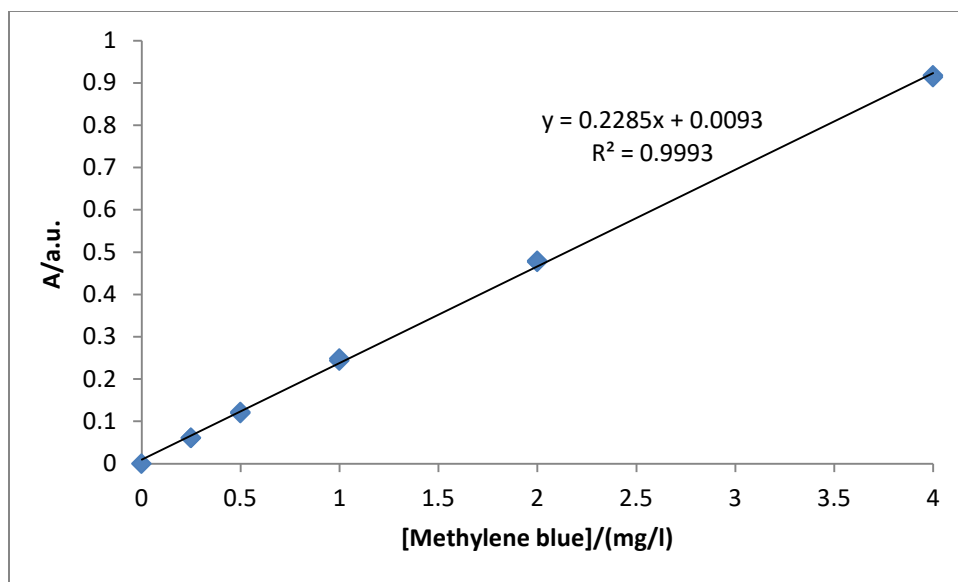


Figure (4-1). The standard calibration curve of methylene blue concentration and UV-Vis absorption.

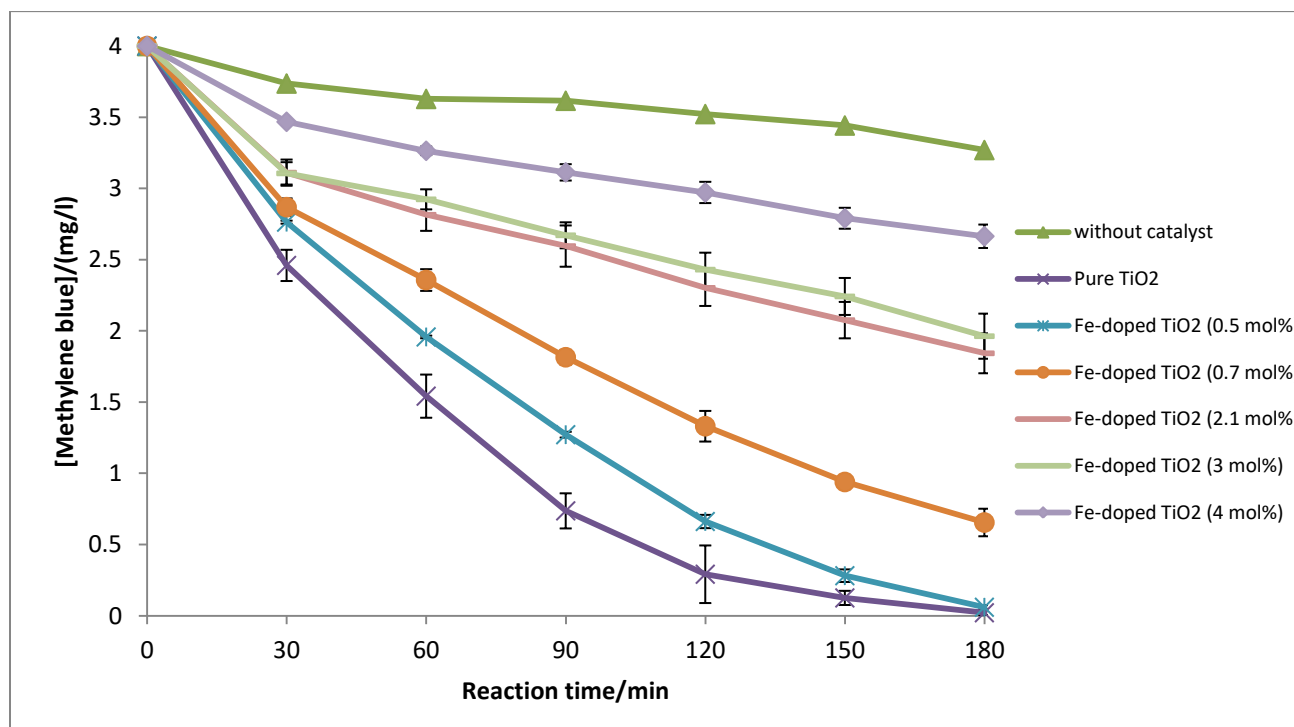


Figure (4-2). Photodecomposition efficiency of pure and iron-doped titanium dioxides for removal of methylene blue dye in water at pH 4.5.

It can be seen that, of all samples studied, pure titanium dioxide has the highest photocatalytic activity, and as the amount of iron in TiO₂ catalyst is increased, the photodegradation activity decreased. Although the addition of iron to titanium dioxide reduces the band gap and expands the absorption edge of TiO₂ from UV to visible area of solar spectrum, the discovered trend in terms of photocatalytic efficiency seems to work in the opposite direction. Photocatalysis is a complex multi-parameter process where band gap enhancement and optical absorption improvement are not the only factors impacting the catalytic behaviour of the prepared catalyst. For example, Zhang *et al.* have shown that particle size plays a crucial role in photocatalytic activity of TiO₂ by impacting the dynamic of electron-hole recombination [1]. They proved that applying iron as dopant only enhances the photonic efficiency of TiO₂ particles smaller than 11 nm by decreasing recombination on the surface of TiO₂. Moreover, particle size determines the surface area of the catalyst, which is a vital parameter for effective light absorption and substrate adsorption-desorption. Ganesh *et al.* also reported that changing the concentration of methylene blue as a substrate can alter the relative photocatalytic efficiency of iron-doped TiO₂ with different iron contents [2]. Overall, the photodegradation is slower for higher concentrations of methylene blue. This arises from intermediate products competing with methylene blue for hydroxyl radicals generated near the surface of the catalyst. In other words, when the initial methylene blue concentration is higher, the concentration of intermediate products are also higher which decreases the methylene blue photodecomposition rate [3]. In our study, the initial concentration of the methylene blue is the same for all tested nanomaterials. This optimised initial concentration is where we expect to obtain the best photocatalytic trend between our materials while ensuring that it is low enough so that Beer-Lambert law applies. This concentration was determined based on literature study and appropriate tests were conducted to establish the optimum methylene blue concentration.

As discussed earlier in section 1-9 of chapter one, the pH of the reaction mixture is a fundamental factor controlling the rate in this photocatalytic process. In order to check the impact of the pH on the photodegradation behavior of our iron-doped TiO₂ nanomaterials, photodegradation tests were performed at the pH values of 3.5 and 2.5 for selected samples including pure TiO₂ and iron-doped TiO₂ (0.5 mol%) nanomaterials. The results at the pH value of 2.5 showed us that the photocatalytic activity of pure TiO₂ and iron-doped TiO₂ containing 0.5 mol% iron are becoming very similar in comparison to pH=4.5. Thereafter, the behavior of these

two abovementioned samples have been studied at the pH values of 2.3, 2.4, 2.6 and 2.7. At pH=2.4, it has been discovered that iron-doped TiO₂ (0.5 mol.%) acts much better than pure TiO₂ in terms of methylene blue photodegradation.

Hence, the photodegradation tests were repeated for all samples at pH 2.4 and another trend is obtained (Figure (4-3)). In general, the photocatalytic process is slower at this pH compared to higher pH values. The reason behind it is that at lower pH values, it is harder to produce hydroxyl radicals which are crucial to conduct photocatalytic reaction [4].

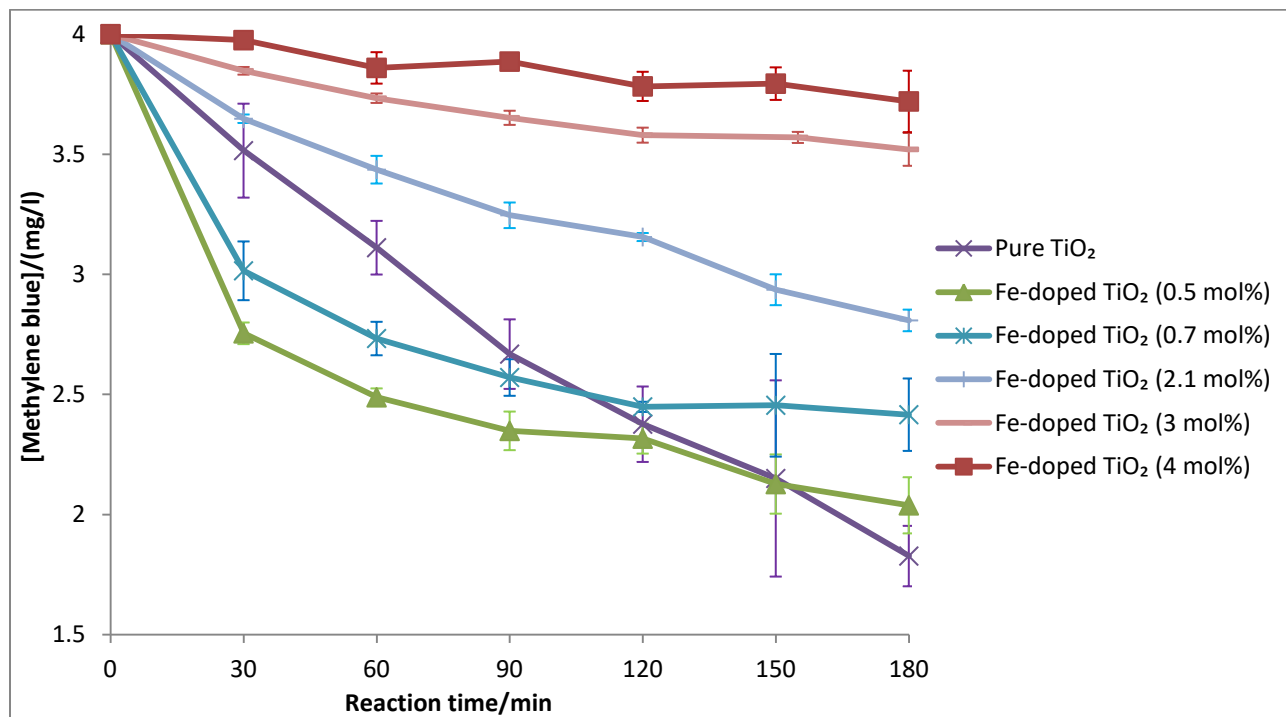
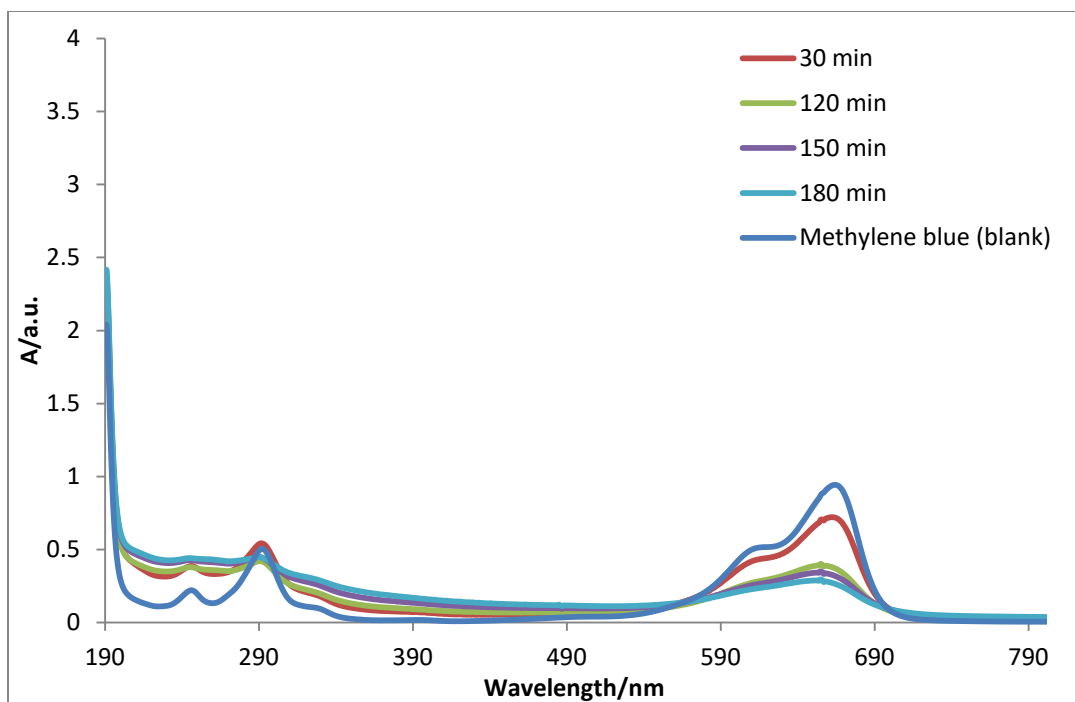


Figure (4-3). Photodecomposition efficiency of pure and iron-doped titanium dioxides for removal of methylene blue dye in water at pH 2.4.

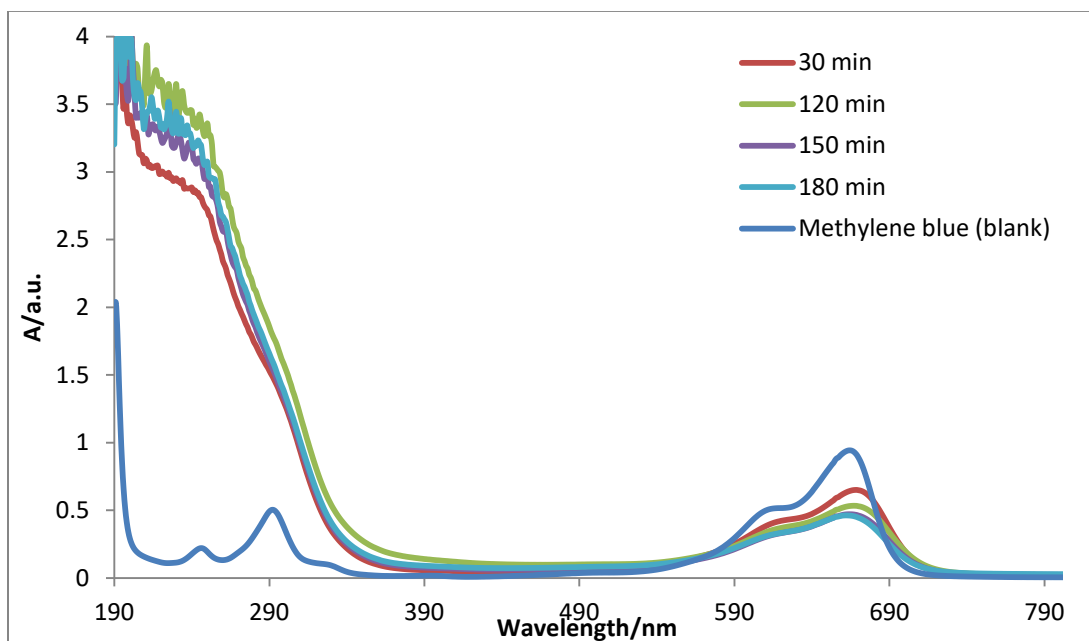
Fe-doped TiO₂ samples with the lowest percentage of iron (0.5 and 0.7 mol% Fe) show significantly high photodegradation activity at the beginning of the reaction compared to all other materials studied in this thesis including pure TiO₂. Then, their activity diminish during the course of the reaction. But the reactivity of pure TiO₂ remains approximately constant during the reaction. In order to understand this process, the UV-Vis spectra of methylene blue solutions that

were used for both pure TiO₂ and iron-doped TiO₂ with 0.5 mol% of iron have been traced as a function of reaction time. As one can observe in Figure (4-4), the two materials, namely pure TiO₂ and iron-doped TiO₂ with 0.5 mol% of iron, give rise to different UV-Vis spectra patterns indicating different products being present in solution during photodegradation. This phenomenon can be attributed to each photocatalytic process following different photodegradation mechanisms.

Different mechanistic pathways have been suggested for the photodegradation of methylene blue and various intermediate compounds have been reported [5-9]. The majority of these intermediates are aromatic compounds with their maximum absorption intensity located below 400 nm. Table (4-1) shows some selected intermediates with the wavelength of their maximum absorption intensity peaks taken from references 10 to 14.



(a)



(b)

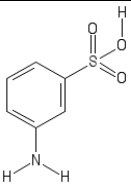
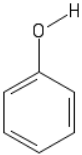
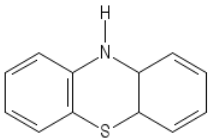
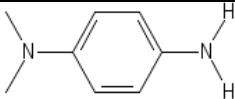
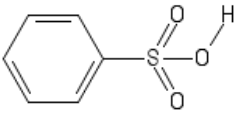
Figure (4-4). UV-Vis spectra of methylene blue used in photodegradation reaction at pH 2.4 with (a) pure titanium dioxide (b) Fe-doped titanium dioxide (0.5 mol% Fe).

When comparing the two different spectral patterns in Figure (4-4), a strong wide absorption band is detected below 400 nm which can be attributed to high concentration of aromatic intermediate compounds in the reaction mixture, when iron-doped titanium dioxide (0.5 mol% Fe) is used as the photocatalyst. But, this wide strong band below 400 nm is absent for pure TiO₂. That means the full degradation of methylene blue intermediates happens completely for pure titanium dioxide and all intermediates are converted to final inorganic products such as water, carbon dioxide, ammonium and sulfate anions [5]. However, at higher pH level (pH=4.5), iron-doped TiO₂ (0.5 mol%) displays a similar behavior as pure titanium dioxide and is able to complete the reaction to full degradation of methylene blue intermediates following a similar mechanism (Figure (4-5)). These observations could be explained by a change of surface chemistry/reactivity as a result of the pH change.

The UV-Vis spectra acquired for higher iron content during the photodegradation reaction is analysed to confirm difference and similarities in the photodegradation mechanisms as a function of pH.

In order to obtain more information about the strong wide absorption band below 400 nm for Fe-doped titanium dioxide (0.5 mol% Fe) at pH=2.4, the isolated solution at each time stage of the reaction is diluted 3 times with deionised water. The resulting spectra series are depicted in the Figure (4-6).

Table (4-1). Intermediate compounds formed during photodegradation of methylene blue and their maximum absorption intensity wavelength.

Compound name	Chemical structure	maximum absorption intensity wavelength (nm)
O-aminobenzenesulfonic acid [6]		≈243 [10]
Phenol [7,9]		≈270 [11]
Phenothiazine [5]		≈254 [12]
N,N-dimethyl-1,4-benzenediamine [7]		253 [13]
benzenesulfonic acid [7,9]		235 [14]

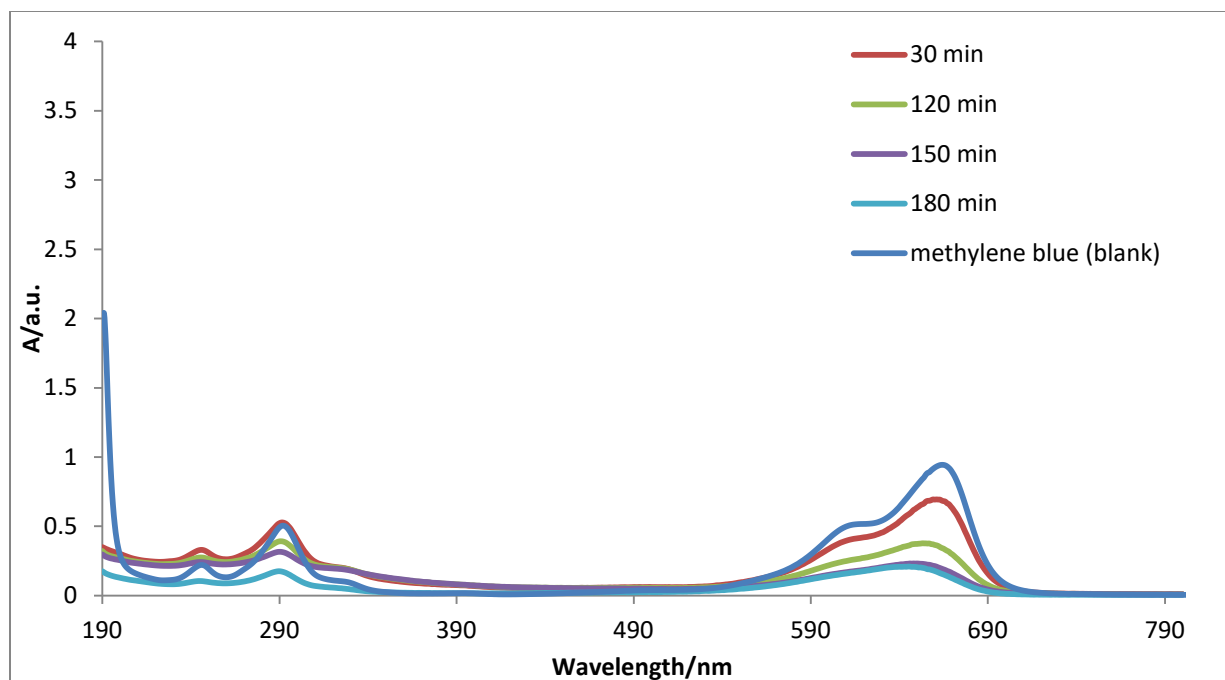


Figure (4-5). UV-Vis spectra of methylene blue used in photodegradation reaction at pH 4.5 with Fe-doped titanium dioxide (0.5 mol% Fe).

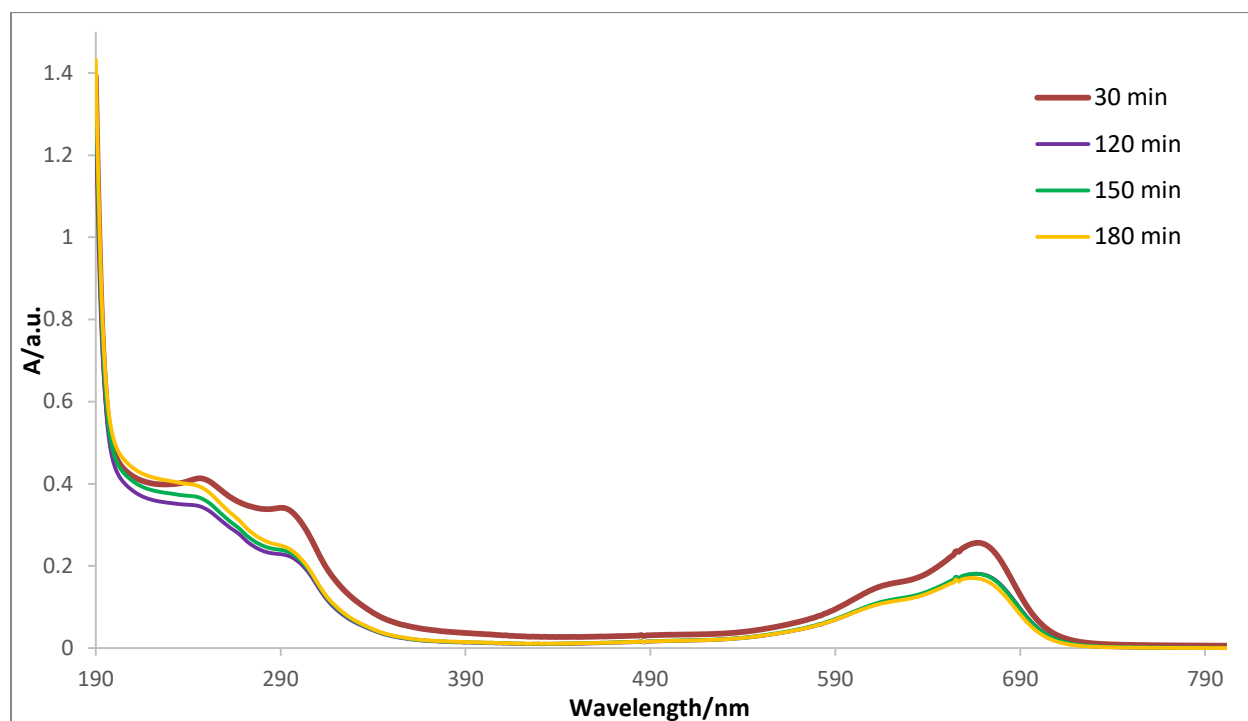


Figure (4-6). UV-Vis spectra of methylene blue used in photodegradation reaction at pH 2.4 with Fe-doped titanium dioxide (0.5 mol% Fe) after 3 times dilution.

Two significant peaks at ca. 293 nm and 248 nm are found. The peak at ca. 248 nm has a close value to three intermediates (243, 253, 254 nm) that are reported for photodegradation of methylene blue, based on the information provided previously in Table (4-1). The other peak with a lower intensity at ca. 293 is close to the absorption of phenol (ca. 270 nm) as one of the other intermediates. However, it might be related to other intermediates that were not detected and/or characterized before. Thus, it can be concluded that the broad absorption band below 400 nm for Fe-doped titanium dioxide (0.5 mol% Fe) at pH=2.4 before dilution belongs to reaction intermediates formed during photocatalysis.

One of the methods to study the surface of the materials at different pH values is to determine their surface zeta potentials as a function of pH. The pH value at which the zeta potential is equal to zero is identified as the "point of zero charge" or PZC. Based on IUPAC recommendation, "PZC is defined as the conditions at which the surface charge density is equal to zero" [15]. Zero net surface charge density does not mean there are absolutely no charges on the surface, it implies the same number of positive and negative charges on the surface of the material [15].

The point of zero charge is measured for all pure and iron doped titanium dioxide samples. The results are summarized in the following diagram. There is a linear relationship between the PZC values and the amount of iron incorporated in the TiO₂ structure, by increasing the load of iron in titanium dioxide, the PZC value is decreasing. Hence, the addition of iron as a dopant to titanium dioxide has an impact on the surface properties in terms of surface charges. The PZC is crucial factor in heterogenous catalysis, since it can have a remarkable influence on the adsorption and desorption of not only the target molecule but also that of the intermediates form during the reaction. However, it is not the only parameter that comes into play in a photocatalytic experiment.

While the PZC plays an important role in the case of pure titanium dioxide and iron-doped one with low concentration of iron (0.5 and 0.7 mol% of iron). Our experiments also show that the PZC does not affect the behavior of titanium dioxides with higher content of iron, i.e. Fe-doped TiO₂ with 2.1 mol% iron content, a drastic change in terms of the photodegradation trend is identified only for pure as well as low-iron-content titanium dioxides by changing the pH value from 4.5 to 2.4.

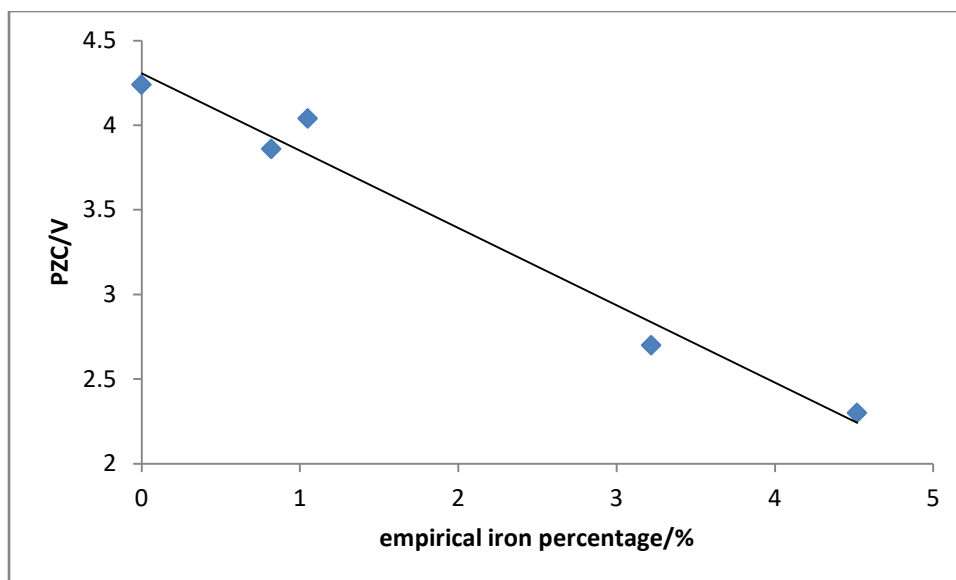


Figure (4-7). The linear relationship between PZC and empirical iron percentage in titanium dioxide samples.

One of the plausible reasons for such a significant difference between pure and iron-doped TiO_2 at pH 2.4 could be the fast decomposition of three-ring structure of methylene blue on iron-doped titanium dioxide (0.5 mol% Fe) into other aromatic intermediates which would suppress the intensity of methylene blue peak at 663 nm and elevate the intensity of intermediate peaks below 400 nm, significantly (Figure (4-8)). Because the PZC value is lower for iron-doped TiO_2 compared to pure TiO_2 , fewer positive charges can be accumulated on the surface of iron-doped titanium dioxide than pure titanium dioxide at an acidic pH of 2.4. Moreover, the pKa value for methylene blue is 3.8 [16], which causes this dye to possess positive charges at any pH lower than 3.8. Because the same electrostatic charges repel each other, there is less tendency for positive-charged methylene blue to be adsorbed on the surface of more positive-charged pure TiO_2 compared to less positive-charged iron-doped TiO_2 (0.5 mol% Fe). Consequently, methylene blue can be adsorbed better on the surface of iron-doped TiO_2 (0.5 mol% Fe) leading to more efficient photocatalytic reaction in the first step which is the decomposition of three-ring structure of methylene blue. However, after completion of first step, two possible scenario can be predicted. Firstly, the high amount of produced intermediates causes a significant pH change, e.g. as a result of various aromatic sulfonic acids formed during the course of reaction.

Some examples of these compounds can be seen in table (4-1) and Figure (4-8). As a result, neither methylene blue itself nor the intermediates are capable to decompose properly because of changing of the surface charge of the photocatalyst as well as the decrease in the concentration of hydroxyl radical produced. Secondly, high concentration of intermediates block the active surface sites and due to Le Chatelier's principle, the equilibrium between the adsorbed intermediates and the ones in the solution would favor the formation of adsorbed intermediates on the surface of the photocatalyst inhibiting the photodegradation reaction.

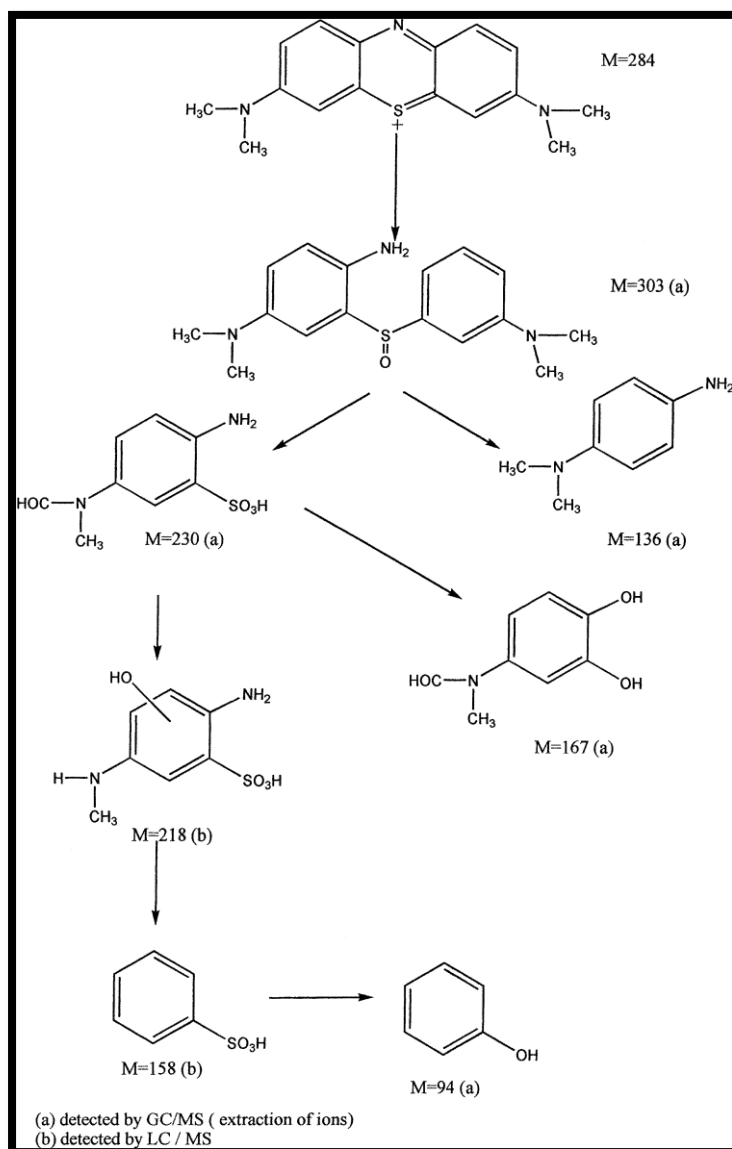


Figure (4-8). One of the proposed mechanisms for the photocatalytic degradation of methylene blue. Reprinted from reference [7], , Copyright © 2001, With permission from Elsevier.

The pH change of the methylene blue solution before and after being used in the photodegradation reaction at pH 2.4 with pure titanium dioxide and iron-doped titanium dioxide (0.5 mol% Fe) has been measured during the course of reaction as a function of time. The results are summarized in the following diagram:

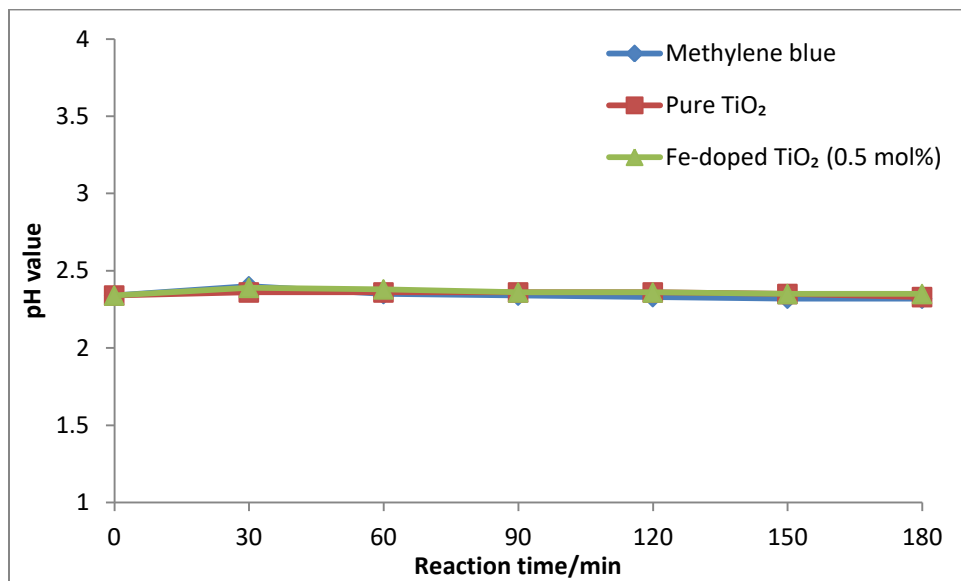


Figure (4-9). Tracing of pH during the course of the reaction for methylene blue solution alone at pH 2.4 and methylene blue solution used in photodegradation reaction at pH 2.4 with pure titanium dioxide and iron-doped titanium dioxide (0.5 mol% Fe).

According to the results obtained, changes of pH during the course of photodegradation reaction is negligible either for methylene blue itself or methylene blue used with pure TiO₂ or iron-doped TiO₂ (0.5 mol% Fe). Consequently, our first hypothesis regarding the sudden pH changes during the reaction progress is not correct and only the second hypothesis could be considered as a plausible mechanism for this reaction.

If PZC was the only factor that could impact the effectiveness of the photocatalytic reaction, we should have observed better outcomes by increasing the amount of iron concentration in titanium dioxide. It is known that having a high content of iron in titanium dioxide leads to higher recombination of electrons and holes formed as a result of photon absorption [17]. Because of this, for the titanium dioxides with high amount of iron, the number of electrons and holes that

can produce active species on the surface of the catalyst is not as high as the one with lower iron content. Consequently, iron-doped TiO₂ with 0.5 and 0.7 mol% of iron are the most optimum material in our case. But we were interested to investigate if the broad peak observed below 400 nm for iron-doped TiO₂ with 0.5 mol% of iron at acidic pH of 2.4 is formed only when the concentration of iron is low. So photodegradation spectral pattern were acquired using for different iron-doped titanium dioxide during the course of methylene blue photodegradation reaction at pH=2.4 (see Figure (4-10)).

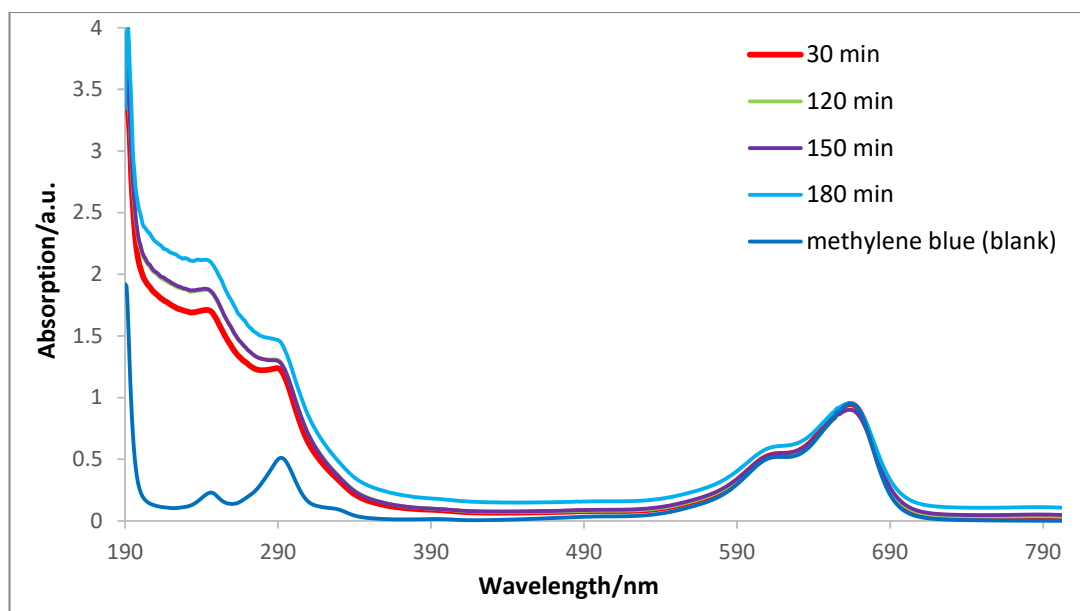


Figure (4-10). UV-Vis spectra of methylene blue used in photodegradation reaction at pH 2.4 with Fe-doped titanium dioxide (4 mol% Fe).

The broad band below 400 nm is also detected for the titanium dioxide with high content of iron. However, for the same reaction times, the signal intensity is lower compared to the one related to iron-doped titanium dioxide with 0.5 mol% iron. It can be concluded that existence of iron can change the mechanism of methylene blue photodegradation. However, the load of iron in titanium dioxide controls the efficiency of this reaction.

4-3-1-Kinetic studies on photodegradation reaction of methylene blue: The Langmuir-Hinshelwood (L-H) model can be applied to all tested samples at pH=4.5 except for pure TiO₂ as

well as iron-doped TiO₂ with 0.5 mol% iron. As shown in Figure (4-11), the kinetic data fit fairly well to a linear Langmuir-Hinshelwood (L-H) model.

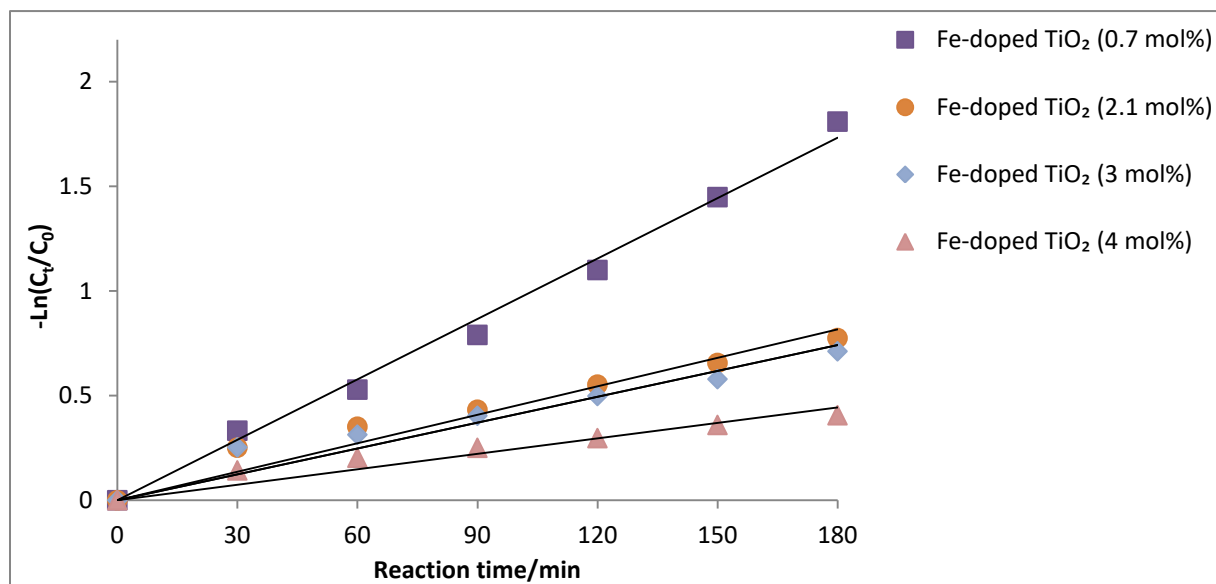


Figure (4-11). Langmuir-Hinshelwood linear transform model for photodegradation reaction of methylene blue at pH=4.5.

The calculated k_{obs} values according to theoretical and empirical amount of iron in titanium dioxide are shown in table (4-2) and Figure (4-12). By increasing the amount of iron as dopant in titanium dioxide matrix, the k_{obs} value has been decreased. This implies that although photodegradation reaction is a sophisticated multiparameter reaction, iron changes the activity of titanium dioxide as a catalyst.

Table (4-2). The calculated k_{obs} values according to theoretical and empirical amount of iron in titanium dioxide for methylene blue photodegradation at pH=4.5.

Theoretical percentage of iron in TiO ₂ (mol%)	Empirical percentage of iron in TiO ₂ (mol%)	k_{obs} (min ⁻¹)
0.7	1.0 (±0.2)	9.6 (±0.6) × 10 ⁻³
2.1	2.6 (±0.2)	4.5 (±2.0) × 10 ⁻³
3	3.2 (±0.6)	4.1 (±2.2) × 10 ⁻³
4	4.5 (±0.3)	2.5 (±1.2) × 10 ⁻³

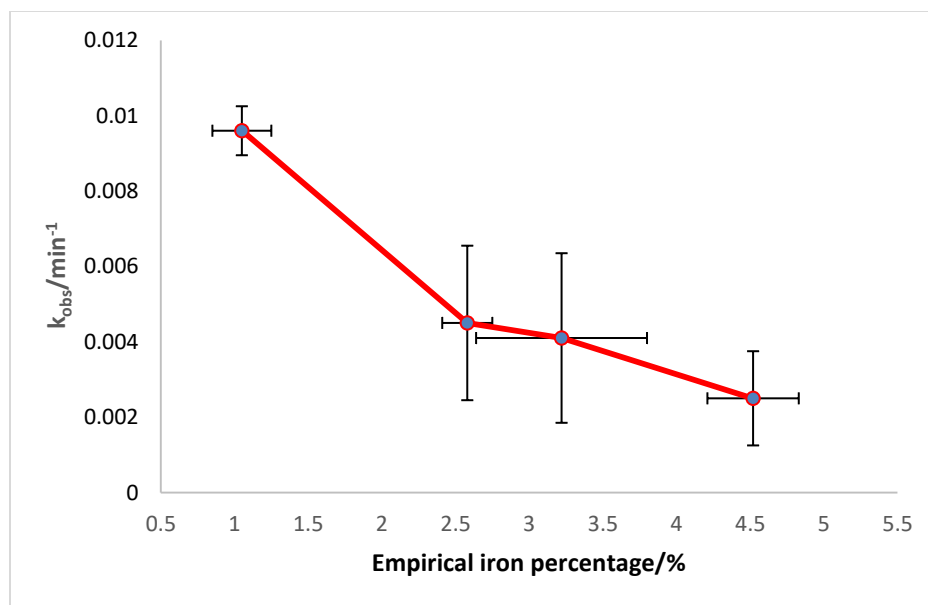


Figure (4-12). Relationship between empirical amount of iron as dopant in TiO₂ and calculated k_{obs} values for photodegradation reaction of methylene blue at pH=4.5.

The k_{obs} values can also be correlated to the band gap values as demonstrated in Figure (4-13). As it is discussed earlier in chapter 2, increasing the content of iron in titanium dioxide decreases the band gap value. However, decreasing the band gap value should technically help to increase the kinetics of photocatalytic reaction, but, as a result of increasing the recombination of

electrons and holes at the same time, the observed trend is reversed. In other words, increasing the band gap leads to the increase in k_{obs} .

The largest k_{obs} value at pH=4.5 ($k_{\text{obs}} = 9.6 \times 10^{-3} \text{ min}^{-1}$) is larger than the two previous reported k_{obs} values (0.00823 min^{-1} [2] and 0.0035 min^{-1} [19] in table (1-1)) for methylene blue photodegradation employing iron-doped titanium dioxide showing that our material has a more efficient photocatalytic activity. But, it is lower than the other reported k_{obs} value (0.0162 min^{-1} [20]), which could be related to a significantly different material morphology. The iron-doped titanium dioxide material used in ref. 20 was in the form of nanotubes and must possess much larger surface area as well as different electronic properties.

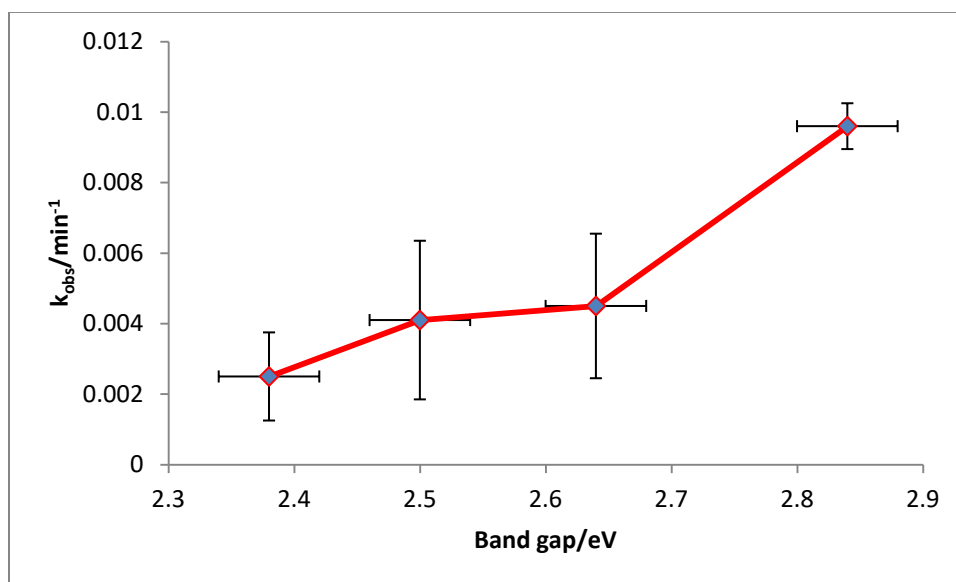


Figure (4-13). Relationship between the band gap values and calculated k_{obs} values for photodegradation reaction of methylene blue at pH=4.5.

In a similar way, a linear transformation based on the Langmuir-Hinshelwood model for photodegradation of methylene blue at pH=2.4 can be obtained only for three iron-doped titanium dioxides with the highest percentage of iron and also for pure titanium dioxide (Figure

(4-14)). The calculated k_{obs} values are also summarized in the following table. Overall, the k_{obs} values at pH=2.4 are lower in comparison to k_{obs} values at pH=4.5.

Regardless of pH change from 4.5 to 2.4 for methylene blue photodegradation reaction, with increasing the empirical amount of iron as dopant in TiO_2 , the calculated k_{obs} values are decreased and with increasing the band gap values, the calculated k_{obs} values are increased (Figure (4-15) and Figure (4-16)).

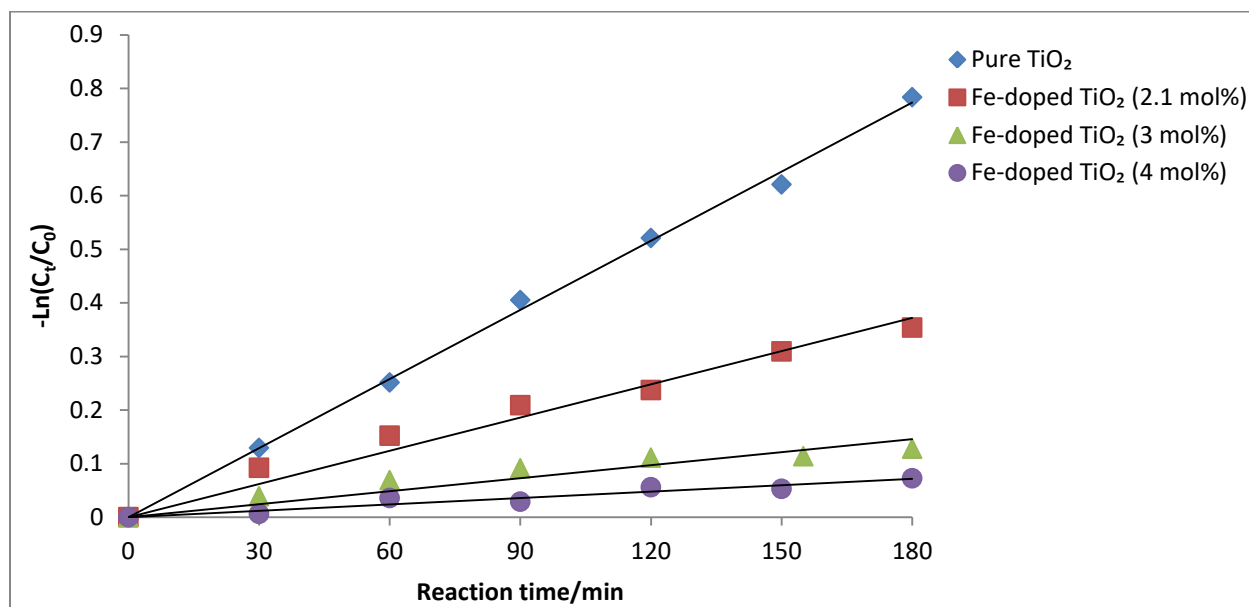


Figure (4-14). Langmuir-Hinshelwood linear transform model for photodegradation reaction of methylene blue at pH=2.4.

Table (4-3). The calculated k_{obs} values according to theoretical and empirical amount of iron in titanium dioxide for methylene blue photodegradation at pH=2.4.

Theoretical percentage of iron in TiO ₂ (mol%)	Empirical percentage of iron in TiO ₂ (mol%)	k_{obs} (min ⁻¹)
0	0	$4.3 (\pm 0.2) \times 10^{-3}$
2.1	$2.6 (\pm 0.2)$	$2.1 (\pm 0.5) \times 10^{-3}$
3	$3.2 (\pm 0.6)$	$8.0 (\pm 2.0) \times 10^{-4}$
4	$4.5 (\pm 0.3)$	$4.0 (\pm 2.0) \times 10^{-4}$

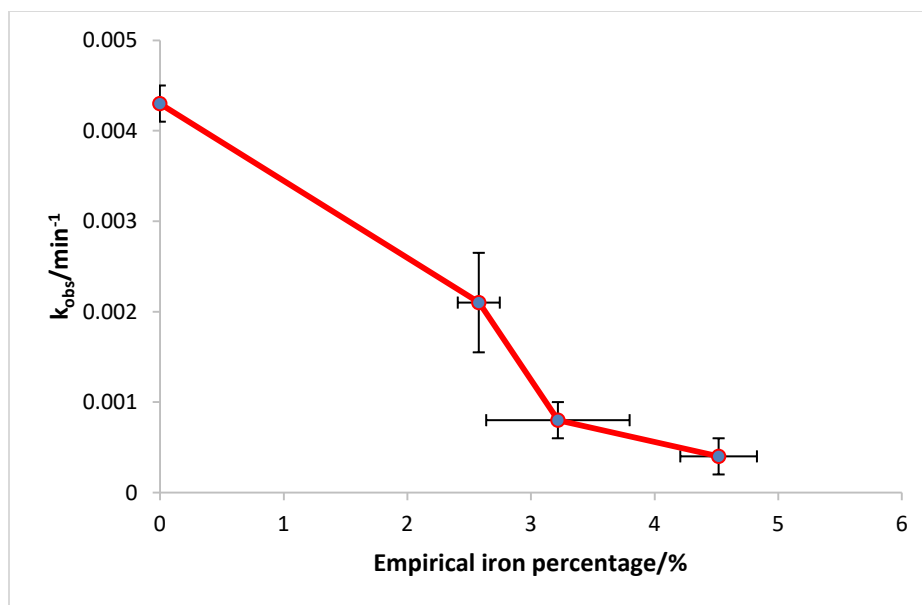


Figure (4-15). Relationship between empirical amount of iron as dopant in TiO₂ and calculated k_{obs} values for photodegradation reaction of methylene blue at pH=2.4.

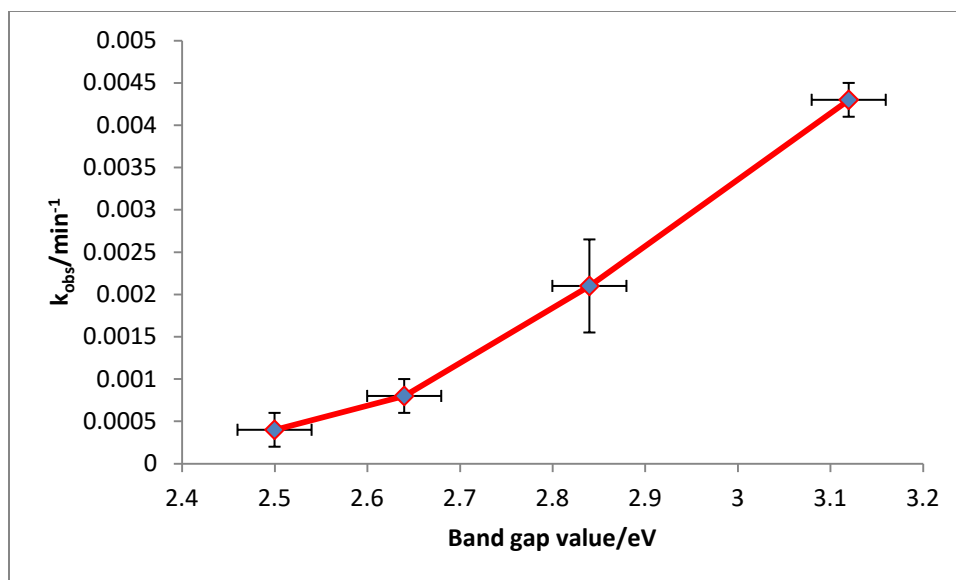


Figure (4-16). Relationship between the band gap values and calculated k_{obs} values for photodegradation reaction of methylene blue at pH=2.4.

4-4-Conclusion

The photodecomposition of methylene blue dye in water has been used to investigate the photocatalytic performance of all prepared iron-doped TiO_2 and pure TiO_2 nanomaterials for reaction times up to 3 hours under simulated solar light. Pure TiO_2 showed the highest photodegradation efficiency at pH=4.5, while at pH=2.4, iron doped TiO_2 nanomaterials containing 0.5 and 0.7 mol% iron showed the highest photodecomposition performance at the beginning of the reaction (ca. first 30 minutes) in comparison to all other tested samples.

The reason for this change in photocatalytic behavior as a result of pH alteration can be attributed to a decrease in positive charges on the surface of the photocatalyst. This can be explained in terms of point of zero charge (PZC). There is a reverse linear correlation between the PZC value and the load of iron as a dopant in titanium dioxide. Due to lower PZC value of iron-doped TiO_2 in comparison to pure TiO_2 , lower number of positive charges in acidic pH value of 2.4 can be accumulated on the surface of iron-doped TiO_2 than pure TiO_2 as a result of adsorption of proton on TiO_2 surface. Moreover, methylene blue has positive charges at any pH value below 3.8. Because the same electrostatic charges tend to repel each other, positively-

charged methylene blue molecules have a lower tendency to be adsorbed on the surface of more positively-charged pure TiO₂ compared to less positively-charged iron-doped TiO₂ (0.5 and 0.7 mol% iron). Hence, methylene blue can be adsorbed more efficiently on the surface of Fe-doped titanium dioxide resulting in higher photocatalytic performance at the onset of the photodegradation reaction, which is the decomposition of the three-ring structure of methylene blue. However, this trend cannot be maintained throughout the course of the reaction due to the production of relatively high concentrations of intermediates leading to the blockage of active sites of the catalysts.

Furthermore, for all prepared materials, which are following the Langmuir-Hinshelwood model, the load of iron in TiO₂ is a controlling parameter in terms of kinetics of methylene blue photodegradation, regardless of the pH value of reaction mixture. Increasing the amount of iron in titanium dioxide decreases the k_{obs} values. Moreover, the decrease in band gap values leads to the suppression of k_{obs} values, which is an unexpected trend. This later phenomenon can be attributed to increasing the recombination of photogenerated electrons and holes by increasing the concentration of iron in TiO₂. In other samples, which are not following this model, the role of iron is still of great importance. But, the kinetics of the reaction is not as simple as Langmuir-Hinshelwood model. Consequently, Langmuir-Hinshelwood is not able to explain the kinetics of all photodegradation reaction happening on the surface of a heterogeneous catalyst.

4-5-References

- [1] Zhang Z.; Wang C.; Zakaria R.; Ying J. Y.; *J. Phys. Chem. B*, **1998**, 102, 10871.
- [2] Ganesh I.; Kumar P. P.; Gupta A. K.; Sekhar P. S. C.; Radha K.; Padmanabham G.; Sundararajan G.; *Processing and Application of Ceramics*, **2012**, 6, 21.
- [3] Xu C.; Rangaiah G. P.; Zhao X. S.; *Ind. Eng. Chem. Res.*, **2014**, 53, 14641.
- [4] Mahvi A. H.; Ghanbarian M.; Nasserri S.; Khairi A., *Desalination*, **2009**, 239, 309.
- [5] Yu Z.; Chuang S. S. C.; *Appl. Catal. B Environ.*, **2008**, 83, 277.
- [6] Huang H.; Leung D. Y. C.; Kwong P. C. W.; Xiong J.; Zhang L.; *Catal. Today*, **2013**, 201, 189.
- [7] Houas A.; Lachheb H.; Ksibi M.; Elaloui E.; Guillard C.; Herrmann J.; *Appl. Catal. B Environ.*, **2001**, 31, 145.
- [8] Xia S.; Zhang L.; Pan G.; Qian P.; Ni Z.; *Phys. Chem. Chem. Phys.*, **2015**, 17, 5345.
- [9] Yang C.; Dong W.; Cui G.; Zhao Y.; Shi X.; Xia X.; Tang B.; Wang W.; *RSC Adv.*, **2017**, 7, 23699.
- [10] <https://webbook.nist.gov/cgi/cbook.cgi?ID=C95169&Mask=400>
- [11] <https://webbook.nist.gov/cgi/cbook.cgi?ID=C108952&Mask=480>
- [12] <https://webbook.nist.gov/cgi/cbook.cgi?ID=C92842&Units=SI&Mask=400>
- [13] Weast R. C.; Astle M. J.; *CRC Handbook of Data on Organic Compounds*, CRC Press Inc., **1994**, Vol. 1, Page 770.
- [14] Weast R. C.; Astle M. J.; *CRC Handbook of Data on Organic Compounds*, CRC Press Inc., **1994**, Vol. 1, Page 1168.
- [15] Kosmulski M.; *Surface Charging and Point of Zero Charge*, CRC Press, Taylor and Francis Group, **2009**.
- [16] https://www.chemicalbook.com/ProductMSDSDetailCB2748858_EN.htm
- [17] Andriamiadamanana C.; Laberty-Robert C.; Sougrati M. T.; Casale S.; Davoisne C.; Patra S.; Sauvage F.; *Inorg. Chem.*, **2014**, 53, 10129.
- [18] Xu C.; Rangaiah G. P.; Zhao X. S.; *Ind. Eng. Chem. Res.*, **2014**, 53, 14641.

[19] Manu S.; Khadar M. A.; *J. Mater. Chem. C*, **2015**, 3, 1846.

[20] Sun L.; Li J.; Wang C. L.; Li S. F.; Chen H. B.; Lin C. J.; *Sol. Energy Mater Sol. Cells*, **2009**, 93, 1875.

Chapter 5: Conclusions and Future Outlook

In this thesis, a series of iron-doped titanium dioxides with various percentages of iron have been prepared. Then, multiple characterization tools, such as X-ray diffraction (XRD), scanning electron microscope (SEM), Energy-dispersive X-ray (EDX), Diffusive Reflectance UV-Vis spectroscopy (UV-Vis DRS), Cyclic voltammetry (CV) and Raman imaging have been employed to evaluate the influence of iron addition on the structure and properties of titanium dioxide. Finally, the photodegradation reaction of methylene blue as model pollutant has been utilized to monitor the photocatalytic properties of all prepared photocatalysts. The impact of pH and its correlation to surface charge properties of iron-doped TiO₂ photocatalysts is carefully investigated.

5-1-Conclusions

The essential findings of this research project are summarized below.

A series of iron-doped titanium dioxide nanomaterials with various percentages of iron were prepared by using sol-gel method. Pure titanium dioxide has been synthesized in a same way for comparison purposes.

X-ray diffraction (XRD) patterns have shown that all prepared pure and iron-doped TiO₂ nanoparticles are composed mainly of the anatase phase. Only three iron-doped TiO₂ samples have a small amount of brookite phase. Rutile phase, iron oxides or iron hydroxides are not detected in any of the samples. Increasing the amount of iron concentration in the TiO₂ matrix leads to broadening of XRD peaks which is an indication of decreasing crystallinity in the system. This could be because of the presence of iron as an impurity in titanium dioxide.

Diffusive Reflectance UV-Vis spectroscopy (UV-Vis DRS) showed that doping of titanium dioxide with iron expands the absorption edge of titanium dioxide from UV to the visible region by decreasing the TiO₂ semiconductor band gap. A comparison between the solid UV-Vis pattern of iron-doped titanium dioxide and the solid mixture of titanium dioxide and iron (III)

oxide containing the similar amount of iron showed that iron is incorporated into the structure of titanium dioxide as a result of doping rather than being simply a mixture of iron (III) oxide with TiO_2 .

All samples including pure and iron-doped titanium dioxides are nanostructures in the form of agglomerates as depicted by scanning electron microscopy (SEM). The size distribution of agglomerates is wide but below 180 nm in diameter.

Energy-dispersive X-ray (EDX) shows the existence of iron in all iron-doped titanium dioxide nanomaterials proving that iron doping has been conducted, successfully. The amount of iron determined by EDX is fairly close to the amount of the iron added to the sample during the synthesis, which is indicative of the accuracy of the synthesis route employed.

Raman imaging of iron-doped titanium dioxide samples and, in a broader view, Raman imaging of metal-doped TiO_2 semiconductors, is reported for the first time. Although, there is no evidence of existence of brookite phase based on the XRD patterns (except iron-doped TiO_2 containing 0.7 mol% iron) in the studied samples, Raman imaging is a more sensitive technique and showed us not only the existence of brookite in our pure and iron-doped TiO_2 samples, but also the effect of iron on distribution pattern of anatase and brookite polymorphs. The load of iron in titanium structure leads to a better dispersion of brookite phase into anatase.

The Raman imaging of N3 dye adsorbed on synthesized pure and iron doped titanium dioxides are reported for the first time. The addition of iron as dopant does not have a significant influence on the adsorption pattern of N3 dye.

The Raman imaging of Z907 dye adsorbed on the synthesized pure and iron doped titanium dioxide are reported for the first time. The addition of iron as dopant, can decrease the amount of Z907 dye adsorbed on the surface of TiO_2 .

The photodegradation of methylene blue dye, a model pollutant in water, has been utilized to study the performance of all prepared iron-doped TiO_2 and pure TiO_2 photocatalysts under simulated sunlight for reaction times of up to 3 hours. At pH=4.5, pure titanium dioxide showed the highest photodecomposition efficiency, while at pH=2.4, iron-doped titanium dioxide nanomaterials with 0.5 mol% and 0.7 mol% iron expressed a higher photodegradation power

compared to all other samples at the beginning of the reaction (ca. first 30 minutes). The reason behind this behavior change as a result of pH change can be traced to charges on the surface of the catalyst, which can be correlated to PZC. There is an inverse linear relationship between the PZC and the amount of iron incorporated into titanium dioxide matrix. Because the PZC value is lower for iron-doped TiO₂ compared to pure TiO₂, fewer positive charges can be accumulated on the surface of iron-doped titanium dioxide than pure titanium dioxide at acidic pH of 2.4 by adsorption of protons on the surface of TiO₂. Furthermore, methylene blue possesses positive charges at any pH lower than 3.8. Because the same electrostatic charges repel each other, there is less tendency for positively-charged methylene blue molecules to be adsorbed on the surface of more positive-charged pure TiO₂ compared to less positive-charged iron-doped TiO₂ (0.5 and 0.7 mol% Fe). Consequently, methylene blue at this pH can be adsorbed better on the surface of iron-doped TiO₂ (0.5 and 0.7 mol% Fe) leading to more efficient photocatalytic reaction in the first step, which is the decomposition of three-ring structure of methylene blue. Such a difference leads to higher performance of these iron-doped catalysts at the onset of photocatalytic reaction. However, they are not able to maintain this trend until the end of the reaction because of the production of relatively high concentrations of intermediates causing the blockage of the catalysts' active sites.

In terms of novelty, the systematic study of the effect of pH on a range of iron-doped titanium dioxide nanomaterials with different loads of iron has been investigated for the first time. In previous studies, only one iron-doped TiO₂ sample was elected to be studied in various pH conditions [1-3]. Moreover, the relationship between the PZC and the amount of iron as dopant in titanium dioxide is reported for the first time as well as the correlation between the concentration of iron in TiO₂ and the rate constant value of the photodegradation process using the Langmuir-Hinshelwood model.

5-2-Future outlook

As future works, the effect of pH change on the photodegradation of doped-TiO₂ can be studied with multiple dopants. For example, the first row of transition metals in periodic table can be one of the interesting systematic studies in this regard. The correlation between the type and amount

of the dopant on the PZC value of titanium dioxide can reveal more knowledge about the influence of doping on the surface properties of TiO₂ nanomaterials.

Changing the molecule used as model pollutant can be employed as another novel approach in this field considering the pK_a value of the molecule as well as the events happening after the decomposition of the molecule.

The Raman imaging of doped titanium dioxide can also be studied using other doping materials at various concentrations. This is one of the fields with lack of reported studies with an enormous potential to be developed. In a similar way, adsorption of various dyes on titanium surface can also be considered as another novel approach to obtain more information regarding the correlation between the surface properties of titanium dioxide and chemical structure of the dye. The outcome of such a research is useful for a better understanding behind the mechanism and function of photodegradation reactions as well as dye-sensitized solar cells (DSSCs).

5-3-References

- [1] Deng F.; Luo X.; Li K.; Tu X.; Luo S.; Yang L.; Zhou N.; Shu H.; *J. Mol. Catal. A: Chem.*, **2013**, 366, 222.
- [2] Tabasideha S.; Malekib A.; Shahmoradib B.; Ghahremani E.; *Sep. Purif. Technol.*, **2017**, 189, 186.
- [3] I. W. Mwangi; Ngila J. C.; Ndungu P.; *Environ. Sci. Pollut. Res.*, **2013**, 20, 6028.